

STATISTICAL HADRONIZATION PHENOMENOLOGY IN HEAVY ION
COLLISIONS AT SPS AND RHIC ENERGIES

by

Giorgio Torrieri

Copyright © Giorgio Torrieri 2004

A Dissertation Submitted to the Faculty of the
DEPARTMENT OF PHYSICS
In Partial Fulfillment of the Requirements
For the Degree of
DOCTOR OF PHILOSOPHY
In the Graduate College
THE UNIVERSITY OF ARIZONA

2004

The University of Arizona ®
Graduate College

As members of the Final Examination Committee, we certify that we have read the dissertation prepared by Giorgio Torrieri

entitled STATISTICAL HADRONIZATION PHENOMENOLOGY IN
HEAVY ION COLLISIONS AT SPS AND RHIC ENERGIES

and recommend that it be accepted as fulfilling the dissertation requirement for the
Degree of Doctor of Philosophy

Keith Dienes

Keith Dienes

date

4/14/04

Johann Rafelski

Johann Rafelski

date

4/14/04

Michael Shupe

Michael Shupe

date

4/14/04

Robert Thews

Robert Thews

date

4/14/04

Ubirajara Van Kolck

Ubirajara Van Kolck

date

4/14/04

Final approval and acceptance of this dissertation is contingent upon the candidate's submission of the final copies of the dissertation to the Graduate College.

I hereby certify that I have read this dissertation prepared under my direction and recommend that it be accepted as fulfilling the dissertation requirement.

Dissertation Director:

Johann Rafelski

date 4/14/04

STATEMENT BY AUTHOR

This dissertation has been submitted in partial fulfillment of requirements for an advanced degree at The University of Arizona and is deposited in the University Library to be made available to borrowers under rules of the library.

Brief quotations from this dissertation are allowable without special permission, provided that accurate acknowledgment of source is made. Requests for permission for extended quotation from or reproduction of this manuscript in whole or in part may be granted by the copyright holder.

SIGNED: _____

ACKNOWLEDGEMENTS

I would like to thank my advisor, committee, a lot more people in and outside the department and, above all, my family.

See Appendix E for details.

DEDICATION

To mum.

TABLE OF CONTENTS

LIST OF FIGURES	9
LIST OF TABLES	14
ABSTRACT	15
1 The strong interaction and quark-gluon plasma	17
1.1 Elementary and collective phenomena	17
1.2 The strong interaction	18
1.2.1 Quarks	18
1.2.2 Color and gluons	19
1.2.3 Quantization and the running coupling constant	22
1.3 The structure of the QCD vacuum at zero temperature	24
1.3.1 Confinement	25
1.3.2 Chiral symmetry breaking	27
1.4 The QCD phase transition	29
1.4.1 A rough calculation (which will prove useful later)	31
1.4.2 Results from lattice QCD	33
1.5 How to study the quark-gluon plasma experimentally	37
1.5.1 Comparison benchmarks	39
1.5.2 Jet quenching	42
1.5.3 Direct photon and dilepton production	46
1.5.4 Charmonium suppression	48
1.5.5 Strangeness enhancement	50
1.5.6 Collectivity	55
1.5.7 QGP evolution	57
1.6 The scope of this thesis	61
2 Statistical hadronization: an overview	63
2.1 Introduction	63
2.2 Thermodynamics and hydrodynamics from Kinetic theory	64
2.3 Statistical hadronization and the Cooper-Frye formula	66
2.3.1 Total particle yields	68
2.4 Treatment of resonance decays	71
2.4.1 Spectra	73
2.5 What kind of statistical hadronization?	79
2.5.1 Long freeze-out	81

2.5.2	Explosive freeze-out	83
2.6	How to falsify freeze-out models	88
3	Particle spectra at SPS: a spherical ansatz	91
3.1	Sudden freeze-out spectra	91
3.2	Spherically symmetric freeze-out	93
3.3	Thermal freeze-out analysis of SPS data	95
3.4	Overview of the results	97
3.5	Statistical significance of the results presented	102
3.6	Omega spectra	103
3.7	Discussion of SPS spectra	105
4	Particle spectra at RHIC: A boost-invariant ansatz	113
4.1	Boost-invariant statistical hadronization	113
4.1.1	General remarks	113
4.1.2	Freeze-out geometry	115
4.1.3	Flow profile	120
4.2	Sensitivity to model choice	123
4.3	Fit to RHIC data ($\sqrt{s_{NN}} = 130\text{GeV}$)	127
5	Direct detection of short-lived resonances	132
5.0.1	Introduction and motivation	132
5.1	Can short-lived resonances be explained by a statistical model?	135
5.2	Modeling resonances in heavy ion collisions	137
5.2.1	Direct production at hadronization	137
5.3	Rescattering	139
5.4	Production of pentaquarks	147
5.5	Momentum dependence of the resonance-particle ratios as a freeze-out probe	155
5.6	Discussion	158
6	Azimuthal anisotropy	163
6.1	Introduction	163
6.2	v_n in the Cooper-Frye approach	166
6.3	Results and discussion	170

7 Summary and outlook	173
7.1 What chapters 3-6 have shown	173
7.1.1 Does non-equilibrium sudden hadronization work?	174
7.1.2 Have we ruled out staged hadronization?	175
7.1.3 Have we constrained freeze-out dynamics?	177
7.2 Outlook on the heavy ion experimental program	178
7.3 Outlook on statistical hadronization	180
APPENDIX A Coordinates and units	184
APPENDIX B Fitting	186
APPENDIX C Relativistic phase space	189
APPENDIX D Publications	191
APPENDIX E Further acknowledgments	192
REFERENCES	194

LIST OF FIGURES

1.1 Potential calculated with full three flavor QCD , rescaled by a constant r_1 at which confinement effects become significant. 1.2 The bag model phase diagram 1.3 Left: The Polyakov loop expectation value as a function of distance at several temperatures. σ refers to the best fit zero temperature flux tube tension. Right: The order of the deconfinement phase transition as a function of the number of flavors and quark masses (physical QCD is somewhere in between the extrema of the diagram). 1.4 Left: Energy density over T^4 (should be flat for a relativistic ideal gas), calculated on the lattice as a function of temperature, scaled with the critical temperature (where the sharp step occurs). Right: The phase diagram on the lattice. The diagonal dotted line shows the limit beyond which the curvature of p/T^4 can not be fitted. The diamond refers to the estimated critical point. 1.5 Polyakov loop susceptibility (left) and $\bar{\psi}\psi$ susceptibility vs $1/g^2$ ($\sim T$) for various quark masses (expressed in terms of the inverse of the lattice size). 1.6 Left: The definition of impact parameter in a colliding system. Right: How energy is distributed after the collision. “Stopping” refers to the dissipation of the system’s initial longitudinal momentum. 1.7 Left: SPS 19.4 GeV/A charged particles pseudorapidity distribution measured by the NA49 collaboration Right: RHIC 130 GeV/A charged particle pseudorapidity distribution measured by PHOBOS, and compared to a boost-invariant statistical model (see chapter 4). 1.8 How an opaque system leads to jet correlations 1.9 Left: jet azimuthal correlation (number of jet pairs emitted at an angular separation $\Delta\phi$) normalized by the number of triggered jets, as measured by the STAR collaboration in p-p, d-Au and Au-Au collisions and 200 GeV. Right: The nuclear modification factor (as defined in section 1.5.1) for d-Au and Au-Au collisions, measured by STAR. The curves refer to calculations done within a model where partonic thermalized degrees of freedom are assumed. Minimum bias means that no centrality selection was performed. 1.10 The di-electron invariant mass (m_{ee}) distribution observed at CERES, per unit of pseudorapidity (η) and scaled with the total pseudorapidity density of observed charged particles $dN_ch/d\eta$. The dotted, dashed and dot-dashed lines represent the expected distribution from electromagnetic decays of known resonances. An excess is observed at $m_{ee} \sim 0.7$ 	26 32 34 35 36 40 43 44 45 47
---	--

1.11	Nuclear modification factor (See section 1.5.1) of charmonium particles (detected through the $J/\Psi \rightarrow \mu^+ \mu^-$ decay) It is plotted against the energy density calculated within the Bjorken model ($\propto R_0^2 dN/dy$, where R_0 , the overlapping nuclear area, depends on centrality). Minimum bias means that no centrality selection was performed.	48
1.12	Density of strange quarks with respect to time calculated in a QGP (left, normalized to baryon density with $m_s = 150$ MeV) and a hadron gas (middle) kinetic production models. As can be seen, equilibration time is significantly shorter for the QGP phase. In addition, as the panel on the right shows, equilibrium strangeness quark content will be stronger in the QGP phase at all chemical potentials.	51
1.13	Left: Production of multi-strange hadrons through combination of strange quarks from a QGP. Right: Detection of strange particles from a heavy ion collision due to decay topology.	52
1.14	The nuclear modification factor (see section 1.5.1) for the production of hyperons as measured by the NA57 experiment, normalized by the number of participants. Particle yields for p-p and Pb-Pb collisions are compared to p-Be, plotted against the number of participants, calculated within the Wounded nucleon model (see section 1.5.1) . . .	52
1.15	Nuclear modification factor for Λ (right) and Λ, Ξ, Ω (left) production calculated within a canonical statistical hadronization model. The result is plotted against the number of participants N_{part} (left) and center of mass collision energy per nucleon (right).	53
1.16	Mass dependence of the apparent temperature (inverse slope in a logarithmic graph) as calculated by uRQMD and HSD models (see section 1.5.1 for references).	56
1.17	Transverse mass distributions for particle and anti-particles as measured by the WA97 experiment	57
1.18	Left: π production per wounded-nucleus a function of energy for A-A vs p-p collisions, plotted against Fermi's energy measure $F = (\sqrt{s_{NN}} - 2m_N)^{3/4} / \sqrt{s_{NN}}^{1/4}$, where $\sqrt{s_{NN}}$ is the average of the center of mass energy per nucleon-nucleon collision. Right: K/π ratio in nucleus-nucleus collisions collisions as a function of $\sqrt{s_{NN}}$	58
2.1	Left: Typical resonance decay patterns. Right: Resonance contribution to observed particle yield as a function of freeze-out temperature	72
2.2	Equilibration fits for SPS (left) and RHIC (right) energies . The $\chi^2/\text{DoF} = 38/16$ at the SPS and $5.7/7$ at RHIC.	81
2.3	How expansion plus vacuum pressure leads to viscous fingering . . .	84
2.4	Entropy, Energy and number density as $\gamma_q > 1$ increases	87
3.1	(color on-line) Thermal freeze-out temperature T for different centrality bins compared to chemical freeze-out analysis shown by horizontal solid lines. Original statistical error is used in the dotted results, five times statistical error for kaon data is used in solid vertical lines.	97

3.2 (color on-line) Thermal freeze-out flow velocity v (top) and break up (hadronization) velocity $\frac{\partial t_f}{\partial r}$ for different centrality bins. Upper limit $\frac{\partial t_f}{\partial r} = 1$ (dashed line) and chemical freeze-out analysis limits for v (solid lines) are also shown.	99
3.3 Hadronization volume (arbitrary units) for different centrality bins.	101
3.4 Thermal analysis chemical quark fugacity λ_q (top) and strange quark fugacity λ_s (bottom) for different centrality bins compared to the chemical freeze-out analysis results.	102
3.5 Thermal analysis chemical quark abundance parameter γ_q (top) and γ_s/γ_q (bottom) for different centrality bins compared to the chemical freeze-out analysis. Thick line: upper limit due to pion condensation.	103
3.6 (color online) Thermal analysis m_T spectra: Λ	104
3.7 (color online) Thermal analysis m_T spectra: $\bar{\Lambda}$	105
3.8 (color online) Thermal analysis m_T spectra: Ξ	106
3.9 (color online) Thermal analysis m_T spectra: $\bar{\Xi}$	107
3.10 (color online) Thermal analysis m_T spectra: K_s	108
3.11 (color online) χ^2/Dof per particle data point. As can be seen, K_s (error given by the experiment) gives the dominant discrepancy	109
3.12 The total error divided by degrees of freedom for different centrality bins, shown as function of (fixed) freeze-out temperature T , bottom for the experimental value of the (statistical) K^0 error, top for the 5 times enlarged kaon data statistical errors.	110
3.13 The total error divided by degrees of freedom for different centrality bins, shown as function of (fixed) flow velocity v on top and for (fixed) freeze-out surface $\partial t_f/\partial r_f = 1/\frac{\partial r_f}{\partial t_f}$ dynamics on the bottom.	111
3.14 (color online) Thermal analysis m_T spectra: $\Omega + \bar{\Omega}$	112
4.1 (Color on-line) While boost-invariance fixes the longitudinal freeze-out structure (left), several scenarios exist for the transverse dependence of freeze-out (right). For spherical freeze-out, only plot on the right applies	119
4.2 (Color on-line) π, K, Λ and Ξ m_T distributions obtained with different freeze-out models and flow profiles. For this and subsequent figures, a uniform density profile was assumed	121
4.3 (color on-line) Results of fits to Monte-Carlo generated data samples I and II ($\frac{dt_f}{dr} = 0$): χ^2 profiles for temperature (left) and fitted $\partial t_f/\partial r$ (right). The models used in the fits are described in sections 1.1 and 1.2 Full fit includes fitted chemical potentials and $\gamma_{q,s}$, resonances and fitted $\partial t_f/\partial r$. Last profile shows effect of fitting sample II using Eq. (4.17)	123

4.4 (color on-line) $dN_{tot}/d(y, \eta)$ arising from freeze-out of a Bjorken fluid, before (open circles) and after (solid circles) resonance decays. The normalization is arbitrary, chosen to coincide with PHOBOS data (triangles)	124
4.5 (color on-line) Results of fits to Monte-Carlo generated data samples III ($\frac{dt_f}{dr} = 1$): χ^2 profiles for temperature (left) and fitted $\partial t_f/\partial r$ (right). The models used in the fits are described in sections 1.1 and 1.2 Full fit includes fitted chemical potentials and $\gamma_{q,s}$, resonances and fitted $\partial t_f/\partial r$	125
4.6 (color on-line) Fit to RHIC data profiles for temperature (left) and fitted $\partial t_f/\partial r$ (right). The models used in the fits are described in sections 1.1 and 1.2 Full fit includes fitted chemical potentials and $\gamma_{q,s}$, resonances and fitted $\partial t_f/\partial r$	127
4.7 (color online) Left: Ξ and Ω m_T distributions, within a global fit including resonances and chemical potentials (Fig. 4.6, solid black) as well as no resonances or chemistry (Fig. 4.6,dashed red). The model with chemical potentials was used to predict the Σ^* m_T distribution using the Monte-Carlo. Right: PHENIX $\pi^- p_T$ distribution, within the global fit from Fig. 4.6. As can be seen, both resonances and γ_q help, but are not sufficient to explain the pion distribution fully.	129
4.8 (color online)(left) K^* , K^- and ϕ normalized spectra within the global fit using non-equilibrium sudden freeze-out (Fig. 4.6, black). (right) momentum dependence of K^* suppression through rescattering of decay products, calculated in the microscopic hadronic model uRQMD	130
5.1 Stages of the space-time evolution of a heavy ion collision. At a certain moment in proper time (known as chemical freeze-out), hadrons emerge. The system then evolves as an interacting hadron gas, until thermal freeze-out, the point at which all elastic interactions cease.	133
5.2 How re-scattering can inhibit resonance reconstruction. If the resonance decay products reach the detector without further interactions, their invariant mass distribution should yield a clear peak at the resonance mass. However, if these decay products undergo re-scattering before reaching the detector, the signal may be indistinguishable from the background caused by unrelated particle pairs.	135
5.3 (Color on-line) Fits to particle ratios containing several short-lived resonances, using an equilibrium (left) and a non-equilibrium (right) formalism. The fit in (right), was obtained using the SHARE program (See Appendix D).	136

5.4	Temperature dependence of ratios of Σ^* , K^{*0} and $\Lambda(1520)$ to the total number of observed K Λ s and Ξ s. Branching ratios are included. Dashed lines show the result for a measurement at central rapidity $\Delta y = \pm 0.5$. The experimental measurements included in the diagram are discussed in the first part of this paper. It should be noted that the K^*/K ratio is actually $\overline{K^*}/K^-$ for the NA49 measurement, and an average $(K^* + \overline{K^*})/(K^+ + K^-)$ for STAR.	140
5.5	Produced (dashed line) and observable (solid lines) ratios $\Lambda(1520)/(\text{total } \Lambda)$, $\Sigma^*/(\text{total } \Lambda)$, K^{*0}/K and $\Xi/(\text{total } \Lambda)$. The solid lines correspond to evolution after chemical freeze-out of 1,2,3,4,5,7,10,15,20 fm/c, respectively. The values at time zero (chemical freezeout) were taken from Fig. 5.4. See Fig. 5.4 caption for the meaning of K , K^*	143
5.6	How temperature and fireball lifetime decouple when two resonances of different masses and widths are compared. A point on any of the above diagrams is potentially sufficient to fix both of these quantities. The experimental measurements are discussed in the first section. See Fig. 5.4 caption for the meaning of K , K^*	146
5.7	K^*/K vs $\Lambda(1520)/\Lambda$ assuming half of the $\Lambda(1520)$ s are suppressed in-medium. See Fig. 5.4 caption for the meaning of K , K^*	147
5.8	(Color online) χ^2/dof for statistical hadronization fits at SPS and RHIC: results are shown for 40, 80, 158A GeV Pb on stationary Pb target collisions and at RHIC for 65+65 and 100+100A GeV Au–Au head on interactions.	151
5.9	(Color online) Yield of $\Theta^+(1540)$ in relativistic heavy ion collisions, based on statistical hadronization fit to hadronization parameters at SPS and RHIC 40, 80, 158A GeV Pb on stationary Pb target collisions and at RHIC for 65+65 and 100+100A GeV Au–Au head on interactions. Relative yields with K_s , Λ , and $\Lambda(1520)$ are shown from bottom to top.	152
5.10	(Color online) Dependence of the K^*/K , Σ^*/Λ and η'/eta on the Freeze-out model	160
5.11	(Color online) $(K^* + \overline{K^*})/(\text{all } K_S)$, $\Sigma^*(1385)/(\text{all } \Lambda)$ and $\eta'/(\text{all } \eta)$ ratios, including feed down from resonances.	161
5.12	(Color online) p_T dependence of $(K^* + \overline{K^*})/(\text{all } K_S)$, $\Sigma^*(1385)/(\text{all } \Lambda)$ and $\eta'/(\text{all } \eta)$ ratios, including feed down from resonances.	162
6.1	A general freeze-out surface in configuration space	166
6.2	Left: Varying flow anisotropy. Right: Varying freeze-out dynamics .	172
6.3	Left: Varying geometrical anisotropy. Right: Varying flow spread .	172
6.4	Left: Varying flow profile. Right: Higher v_n s from an elliptic fireball .	172
B.1	Confidence levels as a function of degrees of freedom.	188

LIST OF TABLES

1.1 Heavy ion Experimental program.	38
1.2 Selected heavy ion Experiments. “Telescope” refers to a detector narrow in both angle and rapidity. “mid-rapidity” to a detector covering rapidity region where the center of mass momentum vanishes. “Wide acceptance” means an area outside the mid-rapidity is covered.	38
2.1 The chemical freeze-out statistical parameters found for nonequilibrium (left) and semi equilibrium (right) fits to SPS results. We show $\sqrt{s_{NN}}$, the temperature T , light quark fugacity λ_q , strange quark fugacity λ_s , the quark occupancy parameters γ_q and γ_s/γ_q . Bottom line presents the statistical significance of the fit. The star (*) indicates for λ_s that it is a value resulting from strangeness conservation constraint. For γ_q that there is an upper limit to which the value converged, $\gamma_q^2 < e^{m_\pi/T}$ (on left), or that the value of $\gamma_q = 1$ is set (on right).	88
2.2 freeze-out statistical parameters found for non-equilibrium (left) and $\gamma_q = 1, \gamma_s$ fitted (right) fits to RHIC results. We show $\sqrt{s_{NN}}$, the temperature T , baryochemical potential μ_b , strange quark chemical potential μ_s , strangeness chemical potential μ_s , the quark occupancy parameters γ_q and γ_s/γ_q , and in the bottom line the statistical significance of the fit. The star (*) indicates that there is an upper limit on the value of $\gamma_q^2 < e^{m_\pi/T}$ (on left), and/or that the value is set (on right).	89
4.1 (Color on-line) Freeze-out hypersurfaces at contours of constant radii.	119
5.1 Resonances contributing to Λ and K production, with their degeneracies, rest-frame momentum (p^*) and possibility for experimental reconstruction.	138
5.2 Scattering model parameters	145

ABSTRACT

This dissertation examines the phenomenology of statistical hadronization at ultrarelativistic energies. We start with an overview of current experimental and theoretical issues in Relativistic heavy ion physics. We then introduce statistical hadronization, and show how it gives a description of particle abundances and spectra through relativistic covariance and entropy maximization.

We argue that several statistical hadronization models are possible; In particular, a distinction can be made between equilibrated staged freeze-out in which post-formation hadron interactions play an important role in determining final-state observables, and non-equilibrium sudden freeze-out where spectra and abundances get determined at the same time and further interactions are negligible.

We attempt to falsify sudden freeze-out by examining whether particle abundances and spectra can be described using the same formation temperature. This is done both in the chemical equilibrium framework, and using a chemical non-equilibrium ansatz. Our fits to experimental data suggest that the sudden freeze-out model explains both the particle abundances and spectra.

We then try to extract the particle formation temperature, and quantify post-freeze-out hadronic interactions using experimentally observable resonances. We discuss observed resonances and suggest further measurements that have the potential to distinguish between the possible freeze-out scenarios experimentally.

Finally, we infer from experimental data how particle formation proceeds in spacetime, in particular whether freeze-out dynamics agrees with the sudden freeze-out expectation. We examine particle spectra, and show that they are not sensitive enough to pick the right freeze-out dynamics. We suggest resonances and azimuthal anisotropy as experimental probes for this task.

CHAPTER 1

The strong interaction and quark-gluon plasma

1.1 Elementary and collective phenomena

Physics research within the last fifty years can be divided into two classes of problems: figuring out the fundamental rules which govern physical processes at the microscopic level, and examining how these fundamental rules give rise to the phenomena we observe macroscopically. Particle physics is concerned with finding the fundamental rules. Condensed matter physics studies how these rules generate complex structure.

This division is somewhat simplistic. Quantum mechanics, together with relativity, imply that every interacting system will always have an infinite number of degrees of freedom. Even the vacuum state will always contain particle-antiparticle pairs popping in and out of it at all times. This means that the vacuum, just like any material studied in condensed matter physics, may exhibit collective phenomena. If the interaction is strong enough, the collective phenomena will dominate “elementary” physics, and the observed degrees of freedom might be, in their nature and behavior, different from the fundamental ones. In other words, to understand the physics of one particle, we need to understand the collective medium through which this particle will propagate.

As an arena to understand general collective systems, condensed matter physics has some limitations. While the structures and properties of condensed matter systems are enormous in their variety, the “elementary rules” they are based on are limited and understood: electromagnetism and quantum mechanics. It is not at all certain that by introducing a different set of fundamental rules we will not arrive at a qualitatively novel macroscopic system. The fact that an analogue of strong interaction confinement has never been found in a condensed matter system reinforces the need to investigate how the “macroscopic phenomena” change when a qualitatively different set of “microscopic rules” is introduced.

The purpose of heavy ion physics is to do just that: to create and study a “condensed matter system” using a different fundamental interaction than electromagnetism.

1.2 The strong interaction

1.2.1 Quarks

According to the current theory of the strong interaction, all hadrons are composed of fermionic constituents called quarks. The non-interacting quark Lagrangian therefore comprises several massive fermion fields, denoted by a quantum number, called flavor (f), conserved in strong interactions

$$L = \sum_f \overline{\psi}_f (i\gamma^\mu \partial_\mu - m_f) \psi_f. \quad (1.1)$$

Quarks are arranged in three flavor doublets, of which the top member has electromagnetic charge $+2/3$ and the bottom member has charge $-1/3$ (in units where the proton has charge $+1$).

The quarks in the first doublet, called up and down (u and d from now on), have a mass that is negligible with respect to the mass of the observed hadrons, and are therefore often called “light quarks”. These quarks are the only ones stable against flavor-changing weak decays.

The quarks forming the second doublet, called strange and charm (s and c) are more massive. The strange quark is of particular interest to the subject of this dissertation, since, as we will see, its mass (50 to 150 MeV) is comparable to both the mass of the lightest hadron and the energy scale of the QCD phase transition. The charm quark is much more massive (~ 1 GeV), though it may be produced in the initial processes of a heavy ion collision. The third doublet, top and bottom, is too massive to be produced in present heavy ion collision experiments (though the ~ 4 GeV b quarks could be studied in future heavy ion collisions).

1.2.2 Color and gluons

The strong interaction, responsible for holding hadrons and nuclei together, is fundamentally very similar to QED in that interactions maintain the Lagrangian invariant under a local phase transformation of the quark wave function

$$\psi \rightarrow U\psi \quad (1.2)$$

$$UU^+ = 1.$$

However, we postulate that quarks transform as vectors in a 3-dimensional space called color space, while anti-quarks are co-vectors

$$\psi = \begin{pmatrix} \psi_r \\ \psi_b \\ \psi_g \end{pmatrix}, \quad \bar{\psi} = (\bar{\psi}_r, \bar{\psi}_b, \bar{\psi}_g). \quad (1.3)$$

Hence, the most general form of Eq. (1.2) allows U to be a special unitary matrix. ($UU^+ = 1$, $|U| = 1$). Such matrices form a group, called $SU(3)$ ¹. It can be shown that for any U eight real numbers α_j can be chosen such that

$$U = e^{i \sum_{j=1}^8 \alpha_j t_j} \quad (1.4)$$

where the generators of the $SU(3)$ group t_j can be represented by the Gell-Mann matrices

$$\begin{aligned} t_1 &= \frac{1}{2} \begin{pmatrix} 0 & 1 & 0 \\ 1 & 0 & 0 \\ 0 & 0 & 0 \end{pmatrix} & t_2 &= \frac{1}{2} \begin{pmatrix} 0 & -i & 0 \\ i & 0 & 0 \\ 0 & 0 & 0 \end{pmatrix} & t_3 &= \frac{1}{2} \begin{pmatrix} 1 & 0 & 0 \\ 0 & -1 & 0 \\ 0 & 0 & 0 \end{pmatrix} \\ t_4 &= \frac{1}{2} \begin{pmatrix} 0 & 0 & 1 \\ 0 & 0 & 0 \\ 1 & 0 & 0 \end{pmatrix} & t_5 &= \frac{1}{2} \begin{pmatrix} 0 & 0 & -i \\ 0 & 0 & 0 \\ i & 0 & 0 \end{pmatrix} & t_6 &= \frac{1}{2} \begin{pmatrix} 0 & 0 & 0 \\ 0 & 0 & 1 \\ 0 & 1 & 0 \end{pmatrix} \\ t_7 &= \frac{1}{2} \begin{pmatrix} 0 & 0 & 0 \\ 0 & 0 & -i \\ 0 & i & 0 \end{pmatrix} & t_8 &= \frac{1}{2\sqrt{3}} \begin{pmatrix} 1 & 0 & 0 \\ 0 & 1 & 0 \\ 0 & 0 & -2 \end{pmatrix}. \end{aligned} \quad (1.5)$$

Just as in the case of electromagnetism, imposing the phase symmetry locally requires the introduction of a covariant derivative to subtract the effect of a varying U on neighboring points. This covariant derivative, however, now contains eight terms corresponding to each Gell-Mann matrix

$$\partial_\mu \rightarrow D_\mu = \partial_\mu - ig \sum_{j=1}^8 A_{\mu j} t_j. \quad (1.6)$$

Physically, substituting D_μ into Eq (1.1) means that quarks can interact through eight bosons called gluons. However, unlike QED, each gluon also carries a color

¹The results described in this section can be generalized to $SU(N)$ invariance, corresponding to physically N colors and $N^2 - 1$ generators. Historically, the first example of this theory to be examined was the Yang-Mills Lagrangian, corresponding to $SU(2)$.

charge, which, in the Gell-Mann representation Eq. (1.5) corresponds to

$$\frac{r\bar{b} + b\bar{r}}{\sqrt{2}}, \frac{r\bar{b} - b\bar{r}}{i\sqrt{2}}, \frac{r\bar{r} - b\bar{b}}{\sqrt{2}}, \frac{r\bar{g} + g\bar{r}}{\sqrt{2}}, \frac{r\bar{g} - g\bar{r}}{i\sqrt{2}}, \frac{b\bar{g} + g\bar{b}}{\sqrt{2}}, \frac{b\bar{g} - g\bar{b}}{i\sqrt{2}}, \frac{r\bar{r} + b\bar{b} - 2g\bar{g}}{2\sqrt{3}} \quad (1.7)$$

for $t_{1..8}$ respectively.

Gauge invariance also allows for a dimension four gluon field contribution to the Lagrangian, equivalent to a curvature tensor in gauge space

$$L \rightarrow L + \sum_{j=1}^8 \text{Tr}([D_\mu, D_\nu][D^\mu, D^\nu]) = L + \frac{1}{4} \sum_{j=1}^8 F_{\mu\nu j} F_j^{\mu\nu}. \quad (1.8)$$

A qualitative difference with respect to QED emerges due to the fact that the matrices $t_{1..8}$ do not commute. Their commutators, represented by the $SU(3)$ structure constants f_{j,j_1,j_2}

$$[t_{j_1}, t_{j_2}] = i \sum_{j=1}^8 f_{j,j_1,j_2} t_j \quad (1.9)$$

will therefore appear in the QCD field strength since

$$[D_\mu D_\nu] = \dots + \sum_{j_1,j_2=1}^8 [t_{j_1} t_{j_2}] A_{j_1}^\mu A_{j_2}^\nu = \dots + i \sum_{j_1,j_2=1}^8 f_{j,j_1,j_2} t_j A_{j_1}^\mu A_{j_2}^\nu \quad (1.10)$$

Hence, gluons can also interact, and their interaction manifests itself in a physical gauge-invariant way through a term in the gluon field strength.

In summary the Lagrangian of interacting QCD is

$$L = \frac{1}{4} \sum_{j=1}^8 F_{\mu\nu}^j F^{\mu\nu j} + \sum_f \sum_{c,\bar{c}=1}^3 \overline{\psi_{\bar{c},f}} \left[i\gamma_\mu \left(\partial^\mu - ig \sum_{j=1}^8 A_j^\mu t_{j\bar{c}} \right) - m_f \right] \psi_{c,f} \quad (1.11)$$

with

$$F_j^{\mu\nu} = \partial^\mu A_j^\nu - \partial^\nu A_j^\mu - g \sum_{j_1,j_2=1}^8 f_{j,j_1,j_2} A_{j_1}^\mu A_{j_2}^\nu. \quad (1.12)$$

Here, the index c runs over the color quantum number, while j runs over the gluon type. The gluon matrices $t_{1..8}$ contract the anti-quark co-vector with the quark vector.

While the symmetry principles used in deriving the QCD Lagrangian follow the QED case closely, the self-interaction term has profound consequences not seen in QED. This becomes evident when the theory is quantized.

1.2.3 Quantization and the running coupling constant

Expanding Eq. (1.11) in terms of $A_{\mu j}$ leads to the following Feynman rules³

$$\begin{array}{c} a \\ \diagdown \\ \text{---} \text{---} \text{---} \\ \text{---} \text{---} \text{---} \\ b \end{array} = ig\gamma_\mu t_{j_1} \quad (1.13)$$

$$\begin{array}{c} p^{\alpha, j_1} \\ \text{---} \text{---} \text{---} \\ \text{---} \text{---} \text{---} \\ q^{\beta, j_2} \end{array} = gf_{j_1 j_2 j_3}(g_{\beta\gamma}(q-r)_\alpha + g_{\gamma\alpha}(r-p)_\beta + g_{\alpha\beta}(r-p)_\gamma) \quad (1.14)$$

$$\begin{array}{c} r^\gamma, j_3 \\ \text{---} \text{---} \text{---} \\ \text{---} \text{---} \text{---} \\ \mu, j_1 \\ \rho, j_3 \end{array} \begin{array}{c} \nu, j_2 \\ \text{---} \text{---} \text{---} \\ \text{---} \text{---} \text{---} \\ \sigma, j_4 \end{array} = -ig^2 \left[\begin{array}{l} \sum_{j'} \{ f_{j_1 j_2 j'} f_{j_3 j_4 j'} (g^{\mu\rho} g^{\nu\sigma} - g^{\mu\sigma} g^{\nu\rho}) \\ + f_{j_1 j_3 j'} f_{j_2 j_4 j'} (g^{\mu\nu} g^{\rho\sigma} - g^{\mu\sigma} g^{\nu\rho}) \\ + f_{j_1 j_4 j'} f_{j_2 j_3 j'} (g^{\mu\nu} g^{\rho\sigma} - g^{\mu\rho} g^{\nu\sigma}) \} \end{array} \right] \quad (1.15)$$

Where the indices correspond to color for quarks ($a, b = 1..3$), type for gluons ($j_{1..4} = 1..8$) and Greek letters for gluon Lorentz indices.

While the first term is similar to the QED case, the next two, which come out of the $f_{abc}A_b^\mu A_c^\nu$ contribution to $F^{\mu\nu}$ are new. Their profound effect can be seen when one attempts to calculate quantum corrections to the coupling constant g (μ is the momentum transfer at which the coupling constant is measured)

$$g^2(q^2) = \frac{g^2(\mu^2)}{1 - [\Pi(q^2) - \Pi(\mu^2)]} \quad (1.16)$$

$$\Pi(q^2) = \left[\text{---} \text{---} \text{---} + \text{---} \text{---} \text{---} + \text{---} \text{---} \text{---} + \dots \right] \quad (1.17)$$

³We will ignore the additional “ghost” particle needed in some gauges. See (Peskin and Schroeder 1995) for more details.

The explicit calculation of this $\Pi(q^2)$ is a somewhat involved endeavor beyond the scope of this thesis (Peskin and Schroeder 1995). However, one can see that since boson loops have the opposite sign from fermion loops, the contribution of the last two diagrams will in general have an effect on the running of the coupling constant opposite to that of the first term. Intuitively, while the first term screens the charge, the gluon loops increase the field strength while maintaining the attractive potential, resulting in a larger effective charge than the bare one (anti-screening). Combining all the diagrams, one can see that in a general Yang-Mills theory with N colors and n light flavors, the coupling constant will be, to a leading order correction (Peskin and Schroeder 1995)¹

$$g^2(k^2) = \frac{g^2(\mu^2)}{1 + \frac{g^2(\mu^2)}{(4\pi)^2} \left(\frac{11}{3}N - \frac{2}{3}n \right) \ln(k^2/\mu^2)}. \quad (1.18)$$

Provided a scale μ^2 can be found where $g^2 \ll 4\pi$ this is a self-consistent result.

In the QED case ($N = 0, n = 1$ for the light electron) $\alpha(k^2)$ increases at increased momentum transfer, and it is found that in low energy experiments $\frac{g^2(k^2 \rightarrow 0)}{4\pi} = \alpha = \frac{1}{137} \ll 1$. Hence,

$$g_{QED}^2(k^2) = \frac{4\pi\alpha}{1 - \frac{2}{3}4\pi\alpha \ln(k^2/m_e^2)} \quad (1.19)$$

with the theory remaining perturbative until a very high energy scale ($\sim e^{700}m_e$) at which QED is not expected to hold anyways.

In the QCD case, however ($N = 3, n = 3$ for three light quarks) the situation is reversed. g^2 decreases with increasing momentum transfer, and eventually becomes perturbative at a large scale Λ (the experimentally measured

¹higher order corrections are generally not thought to change the direction of the running.

$$\frac{g^2(100\text{GeV})}{4\pi} = 0.12 \quad)$$

$$g_{QCD}^2(k^2) = \frac{g^2(\Lambda^2)}{1 + 9\frac{g^2(\Lambda^2)}{(4\pi)^2} \ln(k^2/\Lambda^2)}. \quad (1.20)$$

The highly energetic quarks produced at this energy scale become bundles of approximately collinear fast particles known as jets, with each jet having the momentum of the original quark.

However, at smaller k^2 g^2 increases to the point where perturbation theory ceases to be a useful tool. Thus, while high-energy scattering cross-sections can be computed through perturbative QCD, low-energy effects such as vacuum structure and infrared corrections to particle propagators are governed by non-perturbative physics.

1.3 The structure of the QCD vacuum at zero temperature

The non-perturbative nature of the strong interaction in the low-energy limit should not come as a surprise: the fundamental degrees of freedom of QCD (quarks, gluons) are very different from the fundamental degrees of freedom observed in the strong interactions at low energies (the 100+ hadrons in the particle data book). For instance, every hadron observed so far is not charged under color, and does not interact manifestly through gluon exchange. It must be the case, therefore, that somehow only color singlets survive as physical states. Moreover, QCD predicts gluons to be massless, and high energy scattering processes have determined light quarks to be extremely light (\sim a few MeV). Yet the observed hadrons are much heavier than that (\sim GeV). Both of these phenomena are not as yet rigorously understood. However, there are phenomenological ways to see how they arise.

1.3.1 Confinement

A simple picture of what happens when two color charges (for instance, a quark-antiquark pair $q\bar{q}$) become separated is provided by relativistic quantum mechanics (Gribov 1999): As the separation of the $q\bar{q}$ pair increases, so does the effective charge. At a certain point it becomes energetically convenient to create a new $q\bar{q}$ pair so that a separated $q\bar{q}$ becomes two tightly bound $q\bar{q}$.

An analogous situation exists in atomic physics: Dirac energy levels of an electron orbiting a $Z > 137$ point charge become complex (Rafelski et al. 1978) as it becomes energetically possible to create a real e^+e^- pair out of the vacuum ($A_Z \rightarrow A_Z + e^+ + e^-$). The positron escapes to infinity, and the energy contained in the $(A_Z + e^-)_{\text{bound}} + e^+$ state is less than that of the field of the isolated A_Z ion. The anti-screening of QCD means that the field strength necessary for this vacuum instability will be reached when any two color charges become sufficiently separated (Gribov 1999).

This picture is reinforced by evidence from lattice gauge theory (Wilson 1974), a calculational technique valid when asymptotic freedom applies. In this approach, the continuous spacetime is replaced by a discrete lattice of points, as it is assumed that smaller-scale degrees of freedom become perturbative. It is then possible to represent the pure-gauge action using links from one lattice point to the next

$$U(x_1, x_2)_a \sim e^{ig \int_{x_1}^{x_2} dx_\mu A_a^\mu t_a} \quad (1.21)$$

and calculate physical observables in euclidean spacetime ($t \rightarrow it$) by evaluating a trace over the lattice points (which approaches the functional integral in the

continuum limit) using Monte-Carlo techniques. For instance, the potential energy between two static color sources

$$\langle V(r) \rangle \sim \sum_{a=1}^8 g A_a^0(r) = \sum_{a=1}^8 \langle j_{\mu a} A_a^{\mu} \rangle$$

corresponds to the expectation value of a loop in Euclidean spacetime spanning the particle's separation r (Wilson 1974; Bali 2001).

$$\langle V(r) \rangle = \lim_{t \rightarrow \infty} \frac{1}{t} \log (\langle W(r) \rangle) \quad (1.22)$$

$$\langle W(r, t) \rangle = \frac{\int dA \exp \left[\oint_{0,0}^{r,t} (j_{\mu} A^{\mu} - L) d^4x \right]}{\int dA \exp \left[- \oint_{0,0}^{r,t} L d^4x \right]} \quad (1.23)$$

In the strong coupling limit and neglecting quark loops ¹ it can be proven (Creutz

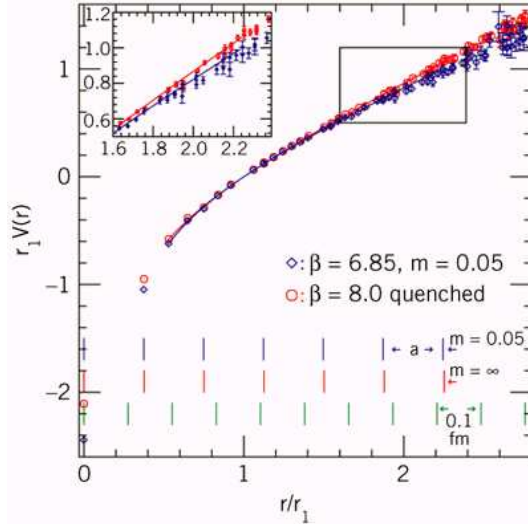


Figure 1.1: Potential calculated with full three flavor QCD , rescaled by a constant r_1 at which confinement effects become significant.

1978) that

$$V(r) \propto r. \quad (1.24)$$

¹This is known as the quenched approximation. Without it, the potential will saturate at the value necessary to create a quark-antiquark pair, as per the Gribov mechanism.

A numerical calculation with a more realistic picture, with three quark flavors, does not change this conclusion; as Fig. 1.1 (Bernard et al. 2000) shows, the effective QCD potential between heavy quark charges can be fitted by a function increasing linearly with r . Heavy quark spectroscopy($c\bar{c}$ J/Ψ states and $b\bar{b}$ Υ states) has experimentally confirmed that the QCD potential can indeed be effectively modeled by a coulomb and a linear term (Richardson 1979; Brambilla et al. 2000).

The Gribov argument and lattice evidence point to a coherent qualitative picture of what happens as the strong interaction coupling constant increases beyond the perturbative limit. Instead of decreasing at large distances, as the electromagnetic potential does, the strong interaction potential continues to increase monotonically until the vacuum decays into more quarks and gluons in such a way as to make every state ultimately observed a color singlet.

This phenomenon, called confinement, has not been fully understood. Nothing similar has, as yet, been observed within many-body systems interacting via electromagnetism. Thus, the study of how confinement arises is a good example of the problems outlined in section 1.1.

1.3.2 Chiral symmetry breaking

A considerable number of hadron masses ($\rho, \text{nucleons}, \Delta, \Lambda, \Sigma, \Sigma^*, \Xi, \Xi^*, \Omega$) can be fitted reasonably well by assuming hadrons to be made up of “constituent” quarks, whose number is given by the hadron’s flavor content. If the constituent quark mass is set to ~ 300 MeV for u, d and ~ 500 MeV for s , observed masses for these hadrons can be described in terms of the constituent quark masses plus spin couplings and electromagnetic effects.

To see how such constituent quark states might arise, consider decomposing the light quark part of the Lagrangian into left-handed and right-handed components

$$\psi = \begin{pmatrix} u \\ d \\ s \end{pmatrix} \quad (1.25)$$

$$\psi_L = \frac{1}{2}(1 - \gamma_5)\psi \quad (1.26)$$

$$\psi_R = \frac{1}{2}(1 + \gamma_5)\psi \quad (1.27)$$

The quark part of the Lagrangian then becomes

$$L_q = \overline{\psi_L}i\gamma^\mu D_\mu\psi_L + \overline{\psi_R}i\gamma^\mu D_\mu\psi_R - \sum_{i=u,d,s} m_{\psi_i}(\overline{\psi_L}\psi_R + \overline{\psi_R}\psi_L). \quad (1.28)$$

We see that the only mixing term is provided by the quark mass. Therefore, in “bare” QCD, the left and right light quark currents should be separated with only a small correction ($\sim 10\text{MeV}$ for u, d , $\sim 100\text{MeV}$ for s).

However, if the QCD vacuum exhibits quark condensation

$$\langle vac | \overline{\psi}\psi | vac \rangle = \langle vac | \overline{\psi_L}\psi_R + \overline{\psi_R}\psi_L | vac \rangle \neq 0$$

the low energy effective Lagrangian will exhibit an additional quark mass, since, as implemented in effective models such as Nambu-Jona-Lasinio (Nambu and Jona-Lasinio 1961; Nebauer and Aichelin 2002), interactions between quarks will generate an effective mass term.

We can see that this is the case in QCD since the Lagrangian in Eq. (1.28) is, in the $m_{u,d,s} \rightarrow 0$ limit, invariant under two separate symmetries

$$\psi_L \rightarrow e^{i(\sum_{i=1,2,3} \alpha_{Li}\sigma_i + \beta_L I)}\psi_L, \quad \psi_R \rightarrow e^{i(\sum_{i=1,2,3} \alpha_{Ri}\sigma_i + \beta_R I)}\psi_R \quad (1.29)$$

where I is the identity matrix, σ_i are the Pauli matrices and $\alpha_{Li,Ri}, \beta_{L,R}$ are real numbers. Using the transformations of Eq. (1.29), corresponding to the

$$\begin{aligned} U(3)_L \times U(3)_R &= SU(3)_L \times SU(3)_R \times U(1)_L \times U(1)_R \\ &= SU(3)_V \times SU(3)_A \times U(1)_V \times U(1)_A \end{aligned}$$

symmetry group, it should be possible to transform any hadron into a hadron of inverse parity (e.g., a negative-parity vector meson, with a current given by $\bar{\psi}\gamma_\mu\psi$, into a positive parity pseudo-vector $\bar{\psi}\gamma_\mu\gamma_5\psi$). Hence, the mass difference between such states (e.g. ρ and $f_1(980)$, or the Λ and the $\Lambda(1405)$) should be of the order of the quark mass. In fact, these differences are $\sim 300\text{MeV}$, the same order of magnitude as the constituent quark mass.

Hence, it appears that $U(3)_L \times U(3)_R$ is spontaneously broken to a lower subgroup. Identifying the lower subgroup as $SU(3)_V \times U(1)_V$ (Isospin \times Baryon number)¹ we are left with eight Goldstone modes, the π, K, η mesons (which are all considerably lighter than the constituent quark prediction, although the large strange quark bare mass makes the K and η much heavier than the π).

The nature of the chiral symmetry breaking, and its relationship with confinement, are under intense study. However, numerical results described in the next section suggest the two phenomena are related.

1.4 The QCD phase transition

The previous two sections make it clear that in empty space light colored particles become confined in massive (at least 140 MeV) color-neutral composite particles.

¹ $U(1)_A$, is broken through quantum corrections ('t Hooft 1976), which is why no light isospin=0 pseudo-scalar meson exists, the η' having a mass of $\sim 1\text{GeV}$.

The question which immediately follows is: What happens if temperature or quark-density increases to such an extent that inter-hadron separation becomes comparable to the separation of quarks within a hadron? Intuitively, hadrons should then break down, and at the very high temperature or density limit the system should approach the asymptotically free limit of a relativistic ideal gas. However, does this occur as a phase transition (ie, a discontinuity in some order parameter) or is it rather a continuous cross-over, much like the formation of the electromagnetic plasma? At what temperature do the quark and gluon degrees of freedom start manifesting themselves? What does a strongly interacting QGP look like away from the infinite temperature limit?

Studying these questions, at both theoretical and experimental levels, is important for a variety of reasons, some of which are discussed in section 1.1. The Universe underwent this phase transition shortly ($t \sim 10^{-6}$ seconds) after the big bang, and evolved as a quark-gluon plasma before that time. Hence, the QCD phase transition might have had consequences for the evolution and structure of the Universe. Moreover, there are astronomical objects today, such as neutron stars, where a QGP might be expected to exist naturally. Finally, to reiterate the point made at the start of this chapter, the QCD phase transition (if it is indeed a phase transition) is the only vacuum phase transition which is at energies experimentally accessible for the foreseeable future (It is very unlikely, for instance, that we will be able to create any-time soon a thermalized system hot enough for electroweak symmetry restoration). The study of the QCD phase transition, therefore, is invaluable for our understanding of quantum field theory in general, especially in the regime where standard perturbation theory methods fail.

1.4.1 A rough calculation (which will prove useful later)

We shall proceed to calculate the QCD phase transition parameters from the MIT bag model (Johnson 1975), an ansatz which can fit reasonably well the spectra of the observed non-Goldstone hadrons. The zero-temperature QCD vacuum is assumed to have a “bag constant” term due to deconfinement/chiral symmetry breaking, i.e. a vacuum energy with positive energy density (ϵ) but negative pressure (P). The energy-momentum tensor is then

$$T^{\mu\nu} = T_{matter}^{\mu\nu} + Bg^{\mu\nu} \quad (1.30)$$

with

$$\epsilon = \epsilon_{matter} + B \quad (1.31)$$

$$P = P_{matter} - B \quad (1.32)$$

Hadrons arise as “bags” filled with free or weakly interacting quarks, trapped in volumes where the pressure exerted by the quarks in the bag balances the negative pressure exerted by the bag.

Through solving the Dirac equation, one can find the quark wave-functions inside the bag and the hadron masses in terms of the bag constant. Fits to the ρ meson, nucleon and Δ yield a bag constant of $B^{1/4} = 150\text{MeV}$ (Chodos et al. 1974). It can be seen that in this model a first order phase transition may occur when a gas of hadrons has the same pressure as a quark-gluon plasma (Rafelski et al. 1996). We calculate the pressures of the particles using the grand canonical ensemble for a non-interacting ideal gas (see the next chapter for details)

$$P = \frac{\partial F}{\partial V} = T \sum_{particles} \int_0^\infty \frac{g_i 4\pi p^2 dp}{(2\pi)^3} (\pm 1) \ln \left(1 + (\pm 1) e^{\frac{\mu - \sqrt{m^2 + p^2}}{T}} \right) \quad (1.33)$$

where \pm applies, respectively, to fermions and bosons and g_i is the degeneracy. For the QGP phase we used 2 massless and one massive quark (fermions) with a degeneracy of 6 (spin×color) and eight gluons (bosons) with a degeneracy of 2 (polarizations). For the hadron gas, in addition to the vacuum pressure given by the bag constant, we used all particles in the particle data book with a mass lighter than 2 GeV (Hagiwara et al. 2002). Light flavor chemical equilibrium was assumed ($\mu_q = -\mu_{\bar{q}}$) and the strangeness chemical potential was put to 0 (no strange quarks).

Fig. 1.2 shows the phase diagram calculated in this ansatz. As can be seen,

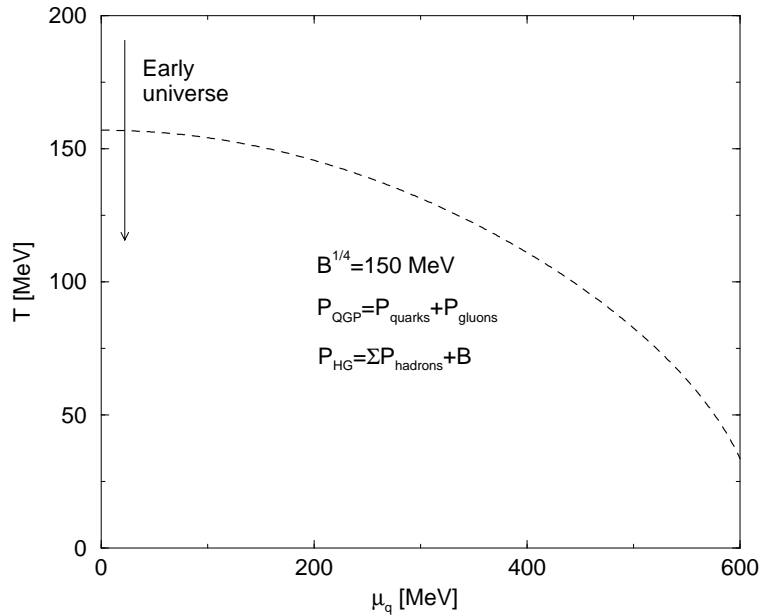


Figure 1.2: The bag model phase diagram .

our estimate predicts a critical temperature roughly equivalent to the mass of the lightest hadron. While many assumptions used in this estimate can be considered naive at first glance, calculations on the lattice give very similar results.

1.4.2 Results from lattice QCD

A phase diagram calculation can also be performed from first principles QCD through lattice techniques, introduced in section 1.3.1. The fact that lattice field theory can be used to describe finite temperature systems is evident from the fact that the QFT partition function

$$Z_{QFT} = \int D\psi DA e^{i \int L(\psi, A) d^3x dt} \quad (1.34)$$

is related to the thermodynamic partition function

$$Z_{TH} = \int D\psi DA e^{- \int L(\psi, A) d^3x / T} \quad (1.35)$$

by the substitution $t \rightarrow i\frac{1}{T}$. This substitution, together with the fact that $e^A = e^{A+2\pi i}$, means that a quantum field theory with a periodic boundary conditions in the time direction (anti-periodic for fermions) (Matsubara 1955; Kapusta 1979)

$$\psi \left(x, t + \frac{2\pi}{T} \right) = -\psi(x, t) \quad (1.36)$$

$$A \left(x, t + \frac{2\pi}{T} \right) = A(x, t) \quad (1.37)$$

will effectively model a finite-temperature quantum field in equilibrium with a heat bath.

In such a formulation the Wilson loop definition given in Eq. (1.23) has to be modified, since no $t \rightarrow \infty$ limit is possible. Instead, the relevant variable becomes the expectation value of the Polyakov Loop (Polyakov 1978; McLellan and Svetitsky 1981), where the quark propagator closes on itself in the periodic

time: ²

$$\langle W_{T \neq 0}(T, r) \rangle = \frac{\int dA \exp \left[\oint_{0,0}^{r, \frac{2\pi}{T}} (j_\mu A^\mu - L) dt d^3x \right]}{\int dA \exp \left[- \oint_{0,0}^{r, \frac{2\pi}{T}} L dt d^3x \right]}. \quad (1.38)$$

It's far from obvious, however, if this calculation will be relevant to the physical world. Eq. (1.35) refers to a system in perfect equilibrium, something which did not apply either to the expanding early Universe or to the conditions in which quark-gluon plasma is created. Nevertheless, a lattice calculation can serve as an indication of what we can expect the quark-gluon plasma phase transition to be like.

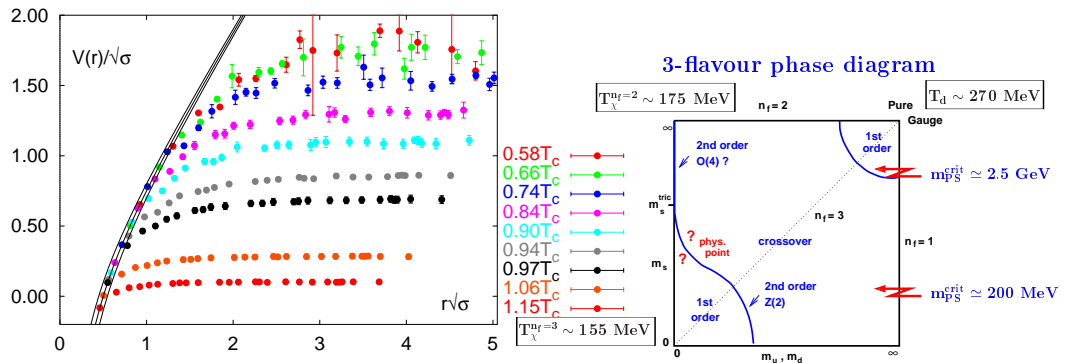


Figure 1.3: Left: The Polyakov loop expectation value as a function of distance at several temperatures. σ refers to the best fit zero temperature flux tube tension. Right: The order of the deconfinement phase transition as a function of the number of flavors and quark masses (physical QCD is somewhere in between the extrema of the diagram).

Fig. 1.3 (Karsch and Laermann 2003) shows that the lattice does indeed exhibit something which looks like a phase transition. As the temperature increases, the distance dependence of the Polyakov loop decreases, to vanish at a critical

²Further evidence that the Polyakov loop is the order parameter for deconfinement is the fact that it is not gauge-invariant for color non-singlets (McLellan and Svetitsky 1981). Hence, unless its expectation value becomes independent of quark separation (which it does above a certain temperature as shown in Fig. 1.3), only color singlets survive as physical states above the lattice scale.

value as expected in a deconfining phase. We still, however, do not know what order characterizes this phase transition, or even if a phase transition is present at all. As the right panel of Fig. 1.3 shows, the order of the phase transition is strongly dependent on theory input, such as the number of flavors and the values of the masses of the light and strange quark. Since performing calculations using realistic inputs for the light and strange quark masses (the realistic values for these quantities are somewhere in the middle of those in the panel) is beyond the range of today's computing power, the order of the phase transition is still unknown. Fig. 1.4

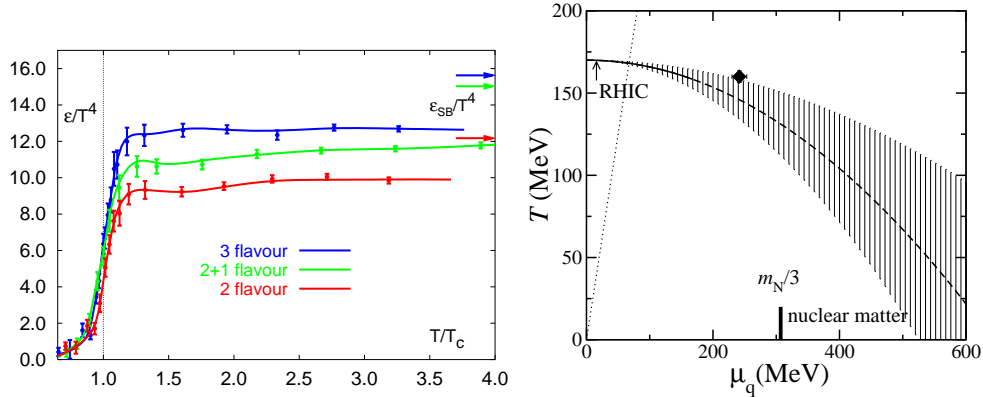


Figure 1.4: Left: Energy density over T^4 (should be flat for a relativistic ideal gas), calculated on the lattice as a function of temperature, scaled with the critical temperature (where the sharp step occurs). Right: The phase diagram on the lattice. The diagonal dotted line shows the limit beyond which the curvature of p/T^4 can not be fitted. The diamond refers to the estimated critical point.

(right) (Ejiri et al. 2003) shows that the phase diagram mirrors very closely that we obtained in the bag model picture of Fig. 1.2. To compound this, Fig. 1.4 (left) shows that, above the rather sharp critical temperature jump, the thermodynamics of the strongly interacting system seems to be close to that of a relativistic ideal gas with perturbative corrections (Letessier and Rafelski 2003).

In fact, as calculated in (Karsch et al. 2003), the hadron gas phase seems

to be modeled closely by the resonance gas ansatz used in this thesis, while perturbation theory to a few orders can describe the QGP just above critical temperature reasonably well (Letessier and Rafelski 2003). Fig. 1.5 (Karsch 1998) can perhaps

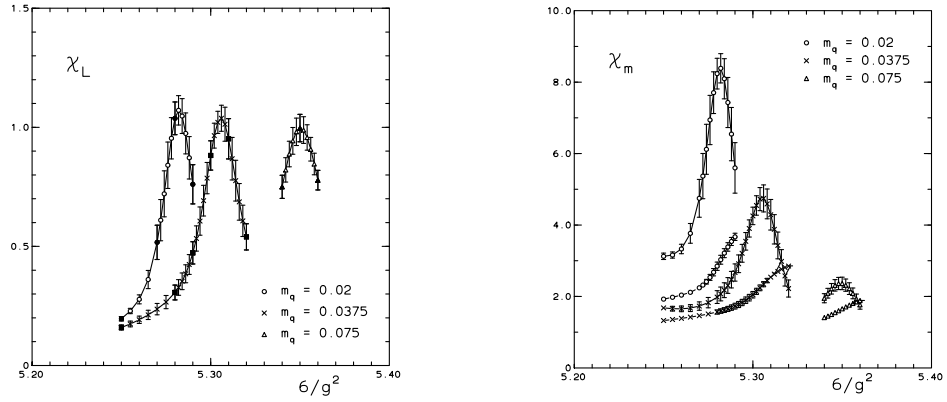


Figure 1.5: Polyakov loop susceptibility (left) and $\bar{\psi}\psi$ susceptibility vs $1/g^2$ ($\sim T$) for various quark masses (expressed in terms of the inverse of the lattice size).

provide an indication of why this is the case. As can be seen, the discontinuity in the Polyakov loop susceptibility χ_L and the $\bar{\psi}\psi$ susceptibility χ_m seem occur at the same temperature for a range of quark masses. Hence, the onset of deconfinement also means that the quarks lose their dynamically acquired “constituent” mass and become nearly massless. This, together with the color screening in a deconfined medium, means that the QGP can be described by the ideal ultra-relativistic gas ansatz at temperatures much lower than originally expected.

1.5 How to study the quark-gluon plasma experimentally

We now proceed to give an overview of the main experimental issues raised in the study of QGP. The only way we can think of to make QGP in a laboratory is to collide two energetic heavy ions (ideally large enough to make an equilibrated system described by the grand canonical ensemble). Hopefully, the collisions will transform some of the energy of the heavy ion into heat, resulting in a hot hadronic system in the center of mass frame. If enough energy is produced, the system will then undergo a phase transition, evolve as quark-gluon plasma, change back into hadrons, and we will be able to tell that a phase transition has taken place and to study the properties of deconfined matter through a careful analysis of the decay products.

It is easy to see that in practice telling whether quark-gluon plasma has been produced is not a simple matter. Indeed, the two claims of quark-gluon plasma production ((Heinz and Jacob 2000) and (Gyulassy 2004)) are both based on an assessment of different kinds of signatures. (And, it should be said, the kinds of signatures claimed by (Heinz and Jacob 2000) differ significantly from those used in (Gyulassy 2004)). Table 1.1 summarizes the experimental heavy ion collision programs energies and nuclei. Some accelerators are geared toward fixed-target experiments and others are colliders. The advantage of the collider is that much more energy is available to make a thermalized system. The disadvantage, aside from the cost, is that it is a lot more difficult to have an acceptance covering a large solid angle (rather than some region, for example mid-rapidity). Table 1.2 provides a list of some heavy ion experiments. In the next subsections, we will proceed to give a summary of the issues involved in each experiment.

Table 1.1: Heavy ion Experimental program.

Accelerator	Type	System under study	Energy (GeV/A) (Center of Mass)	Place
SIS	Fixed target	Various	2-4	GSI, Darmstadt
AGS	Fixed target	Au-Au, S-Au	2-11	BNL, NY
SPS	Fixed target	C-C, S-S, Pb-Pb	40, 80, 158 (8.73, 12.3, 17.3)	CERN, Geneva
RHIC	Collider	Au-Au	19.5, 130, 200	BNL, NY
LHC (2007)	Collider	From p-p to Pb-Pb	7000	BNL, NY
GSI (200...)	Collider	High μ_B /density	In development	GSI, Darmstadt

Table 1.2: Selected heavy ion Experiments. “Telescope” refers to a detector narrow in both angle and rapidity. “mid-rapidity” to a detector covering rapidity region where the center of mass momentum vanishes. “Wide acceptance” means an area outside the mid-rapidity is covered.

Name	Location	Predominant phase space	What it measures
KaoS, FOPI	SIS	Wide acceptance	Hadrons, Strangeness
E864,E878,E886	AGS	Wide acceptance	Hadrons, Strangeness
NA57	SPS	Telescope	Strangeness
NA49	SPS	Wide acceptance	All hadronic signatures
NA50, NA60	SPS	Telescope	leptons, J/Ψ
WA98	SPS	Telescope	γ s, hadrons
CERES/NA45	SPS	Mid-rapidity	γ s, leptons
STAR	RHIC	Mid-rapidity	Hadrons, jets, strangeness
PHENIX	RHIC	Mid-rapidity and telescope	Hadrons, jets, leptons, γ s
PHOBOS	RHIC	Wide, mid-rapidity parts	Hadrons, jets
BRAHMS	RHIC	Telescope, wide rapidity	Hadrons, jets, strangeness
ALICE	LHC	Mid-rapidity	Everything
CMS	LHC	Mid-rapidity	J/Ψ , Υ , γ s, jets, leptons
ATLAS	LHC	Mid-rapidity	Υ , jets

1.5.1 Comparison benchmarks

The first issue to think about is a comparison benchmark. To test for qualitatively new physics, the system under consideration has to be compared to a system in which the physics can be understood in terms of phenomena encountered previously. In our case, this means a system with low energy, or very few hadrons, in which we know that quark-gluon plasma can not be produced, and the dynamics can be understood either by perturbative QCD or as a superposition of hadron-hadron collisions. The latter can be analyzed in terms of elementary collisions measured in control experiments, either through bulk analytical calculations (e.g. the wounded nucleon model (Ftacnik et al. 1987)) or microscopic kinetic models (e.g. Quantum molecular dynamics, or uRQMD (Bass et al. 1998) or hadronic string dynamics, or HSD (Ehehalt and Cassing 1996)).

The most obvious choice for a benchmark experiment is proton-proton collisions. Any effects peculiar to Nucleus-Nucleus ($A - A$ or $A - B$) collisions can be parametrized through the nuclear modification factor (normally referred to as R_{AB} , sometimes as “enhancement” or “suppression”, depending on what the measured or expected physics looks like): the ratio of a quantity observed in the nuclear collision to the same quantity observed in a $p - p$ collision normalized by the product of the two nuclei mass numbers $A \times B$, or by the number of participants.

Proton-proton collisions might not always be a good benchmark, since there can be large volume or many-body effects which are not associated with the phase transition but still have to be accounted for. Hence, proton-nucleus, deuteron-nucleus or collisions between light nuclei are also studied. In these, there is a large volume of excited matter and many collisions, but (presumably) no phase transition.

More generally, it is possible to analyze observables in terms of collision centrality

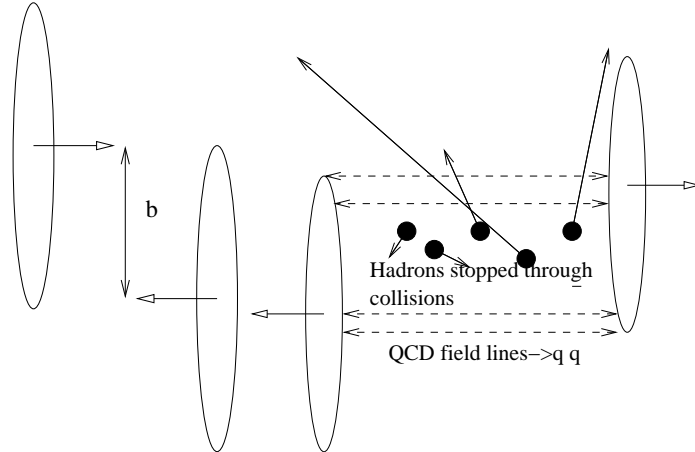


Figure 1.6: Left: The definition of impact parameter in a colliding system. Right: How energy is distributed after the collision. “Stopping” refers to the dissipation of the system’s initial longitudinal momentum.

(number of participants) or collision energy. This way, one can investigate if there is a critical energy (roughly correlated with temperature) or number of participants (roughly correlated with reaction volume and evolution time) at which qualitatively new behavior (e.g., a phase transition) occurs. A measure of the collision centrality is provided by the number of participating nuclei, related to the impact parameter, b , Fig. (1.6 Left). b can be found either directly, by having a detector placed downstream from the collision point to measure how many nucleons escaped the primary collision, or indirectly, by simply measuring the total multiplicity (which is related to the volume of the thermal system).

It should be noted, however, that increasing the collision energy leads to some non-trivial consequences which should be taken into account. First of all, higher collision energy increases the role of perturbative QCD within the system. In the non-perturbative limit, the particles will undergo repeated soft interactions

after the primary collision. These interactions will stop the particles in the collision region and transform their initial colliding energy into thermal energy. Hence, the size of the colliding system, and ultimately the total number of particles produced, will scale as the number of participants

$$N_{prod} \propto N_{participants} \quad (1.39)$$

As the collision energy increases, perturbative interactions will play a bigger role. This means that collisions, rather than participants, will play a larger role in stopping the system, and the scaling becomes (parametrized by α, β)

$$N_{prod} = \alpha N_{participants} + \beta N_{collisions} \quad (1.40)$$

$$N_{collisions} \sim N_{participants}^{4/3}. \quad (1.41)$$

Due to the large center of mass momentum and asymptotic freedom, stopping in primary collisions will decrease with increasing energy. Two highly energetic heavy ions will pass each-other nearly transparently. Their energy will be released into the medium due to confinement, as the color fields generated by the initial collision interactions become stronger and ultimately melt into incoherent $q\bar{q}$ pairs (see Fig. 1.6 (right)). The two highly Lorentz-contracted nuclei can be thought of as capacitors of the color field). For this reason, heavy ion systems colliding at high energy also tend to have a lower baryon density and chemical potential.

These considerations also control the likely initial conditions for hydrodynamic evolution. A system with high baryon stopping will evolve from the pancake-shaped collision region, localized in rapidity space around the center of mass frame. This system has been originally analyzed as a starting point for hydrodynamic evolution by Landau (Landau 1953). In the infinite time limit, it should give rise to an

elliptical fireball with comparable transverse and longitudinal flow profiles, which at mid-rapidity can be well approximated by a spherically symmetric freeze-out.

By contrast, the thermalized system formed when the two very energetic nuclei pass through each other will have a high degree of boost-invariance. As argued in (Bjorken 1983), two highly Lorentz-contracted “pancakes” passing nearly transparently through each-other will look the same in a boosted reference frame. Hence, the dynamics of this collision should exhibit a rapidity plateau. As shown in (Bjorken 1983) this initial condition is hydro-dynamically stable.

Fig. 1.7 shows that the two limits can be used as an ansatz for, respectively, SPS and RHIC energies. At the SPS (Appelshauser et al. 1999), the pseudorapidity distribution is approximately Gaussian, corresponding to a sharp longitudinal structure. Hence, we have used a spherical flow profile to model SPS mid-rapidity data in chapter 3. As the right panel of Fig. 1.7 shows, the situation is perhaps different at RHIC. We have used the Monte-Carlo described in detail in chapter 4 to verify that the flat pseudorapidity distribution observed by PHOBOS (Olszewski et al. 2002) can be reproduced by a boost-invariant source. Such a source is described in detail, and used to model RHIC data, in chapter 4³.

1.5.2 Jet quenching

Jets, or energetic streams of hadrons resulting from a perturbative QCD interaction, are a promising test of whether the dense system formed in a heavy ion collision exhibits hadronic or partonic degrees of freedom. A parton propagating through

³Recent data from BRAHMS (Bearden 2004) may have thrown the validity of this picture in doubt, as the rapidity distribution of identified π is approximately a Gaussian, similar to (Appelshauser et al. 1999) and predicted by the Landau model.

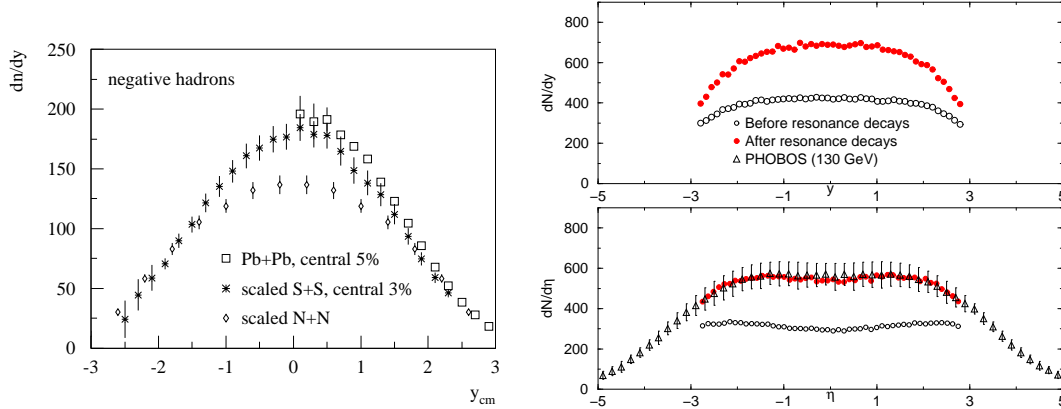


Figure 1.7: Left: SPS 19.4 GeV/A charged particles pseudorapidity distribution measured by the NA49 collaboration Right: RHIC 130 GeV/A charged particle pseudorapidity distribution measured by PHOBOS, and compared to a boost-invariant statistical model (see chapter 4).

a quark-gluon plasma can lose a lot of energy quickly due to repeated interactions with soft gluons. This energy loss is especially pronounced due to the quantum interference of interactions between many coherent gluons (this is known as the Landau-Pomeranchuk-Migdal effect) (Wang et al. 1995). The quark-gluon plasma is therefore expected to be much more opaque to jets than ordinary nuclear matter. One way to quantify such opacity is to measure jet azimuthal correlation, and compare it to elementary (proton-proton or proton-nucleus) collisions. As Fig. 1.8 shows, in an opaque system one of a pair of jets should become quenched, and hence unobservable. For this reason, jets should lose the expected azimuthal correlation. In case of non-central collisions, this effect will also acquire an angular dependence (Gyulassy et al. 2001).

As Fig. 1.9 (left) shows, this effect has received a remarkable experimental confirmation (Adams et al. 2003a). The observed loss of azimuthal correlation is qualitatively unique to Au-Au collisions, the jets in both p-p and d-Au collisions

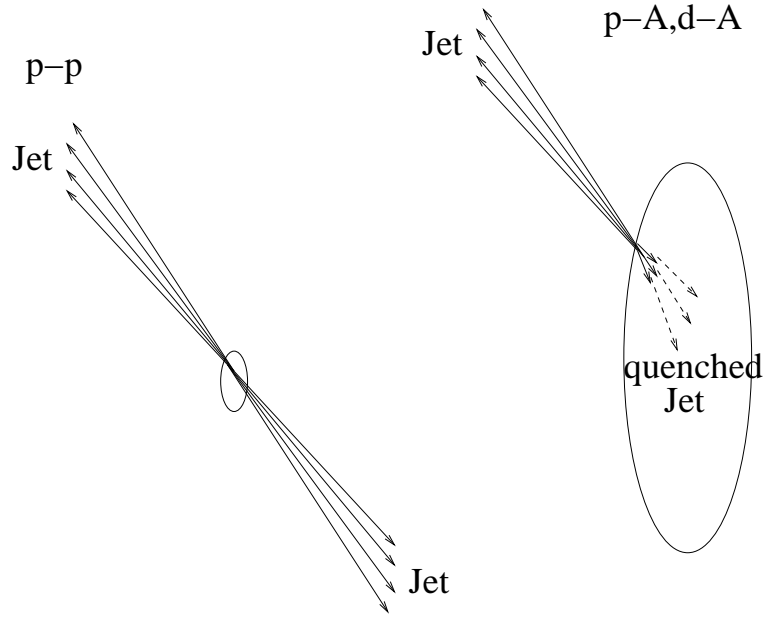


Figure 1.8: How an opaque system leads to jet correlations .

being perfectly correlated. As Fig. 1.9 (right) shows, the loss of azimuthal correlation is accompanied by the loss of hard (jet-energy) particles, with respect to an extrapolation of hard particles produced in p-p collisions. This is also unique to Au-Au, hard particles in d-Au being enhanced.

While some features of the data have recently been modeled within a hadronic scenario with strong in-medium modifications (Capella et al. 2004), the full high p_T dataset from p-p, Au-Au and d-Au collisions has only been convincingly described in a model which assumes that the matter at the center of Au-Au collisions exhibits colored degrees of freedom and is 100 times the density of normal nuclear matter. Furthermore, the non-decrease of the jet suppression with p_T could only be modeled by taking the Landau-Pomeranchuk-Migdal effect into account (Gyulassy et al. 2003).

While the evidence described above makes jet quenching widely regarded

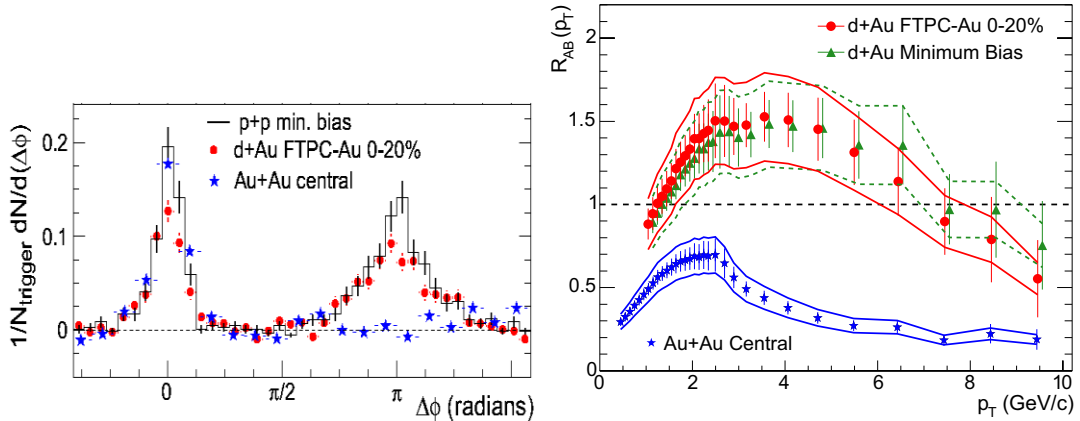


Figure 1.9: Left: jet azimuthal correlation (number of jet pairs emitted at an angular separation $\Delta\phi$) normalized by the number of triggered jets, as measured by the STAR collaboration in p-p, d-Au and Au-Au collisions and 200 GeV. Right: The nuclear modification factor (as defined in section 1.5.1) for d-Au and Au-Au collisions, measured by STAR. The curves refer to calculations done within a model where partonic thermalized degrees of freedom are assumed. Minimum bias means that no centrality selection was performed.

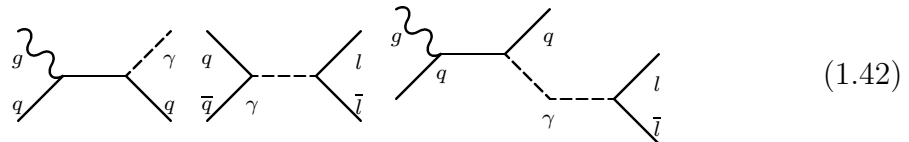
as the definitive proof of QGP formation (Gyulassy 2004), jet quenching as a QGP diagnostic has limitations. The information it provides about QGP equilibration, kinetics and equation of state is rather limited. Jets will not evolve with the bulk of the matter, and their hadronization, due to asymptotic freedom, will not impact the observed energy-momentum distribution significantly. While jets can sample some extensive quantities, such as the density of matter they traverse, soft physics is needed to understand if the system having those extensive quantities is equilibrated in a particular phase, or if it is in a different phase from the usual hadronic matter (Wang et al. 1995). Soft physics is also needed as a complement to perturbative QCD to account for the missing jet energy. Modeling quantitatively how the jet energy is distributed among the soft degrees of freedom, and what the effect of the deposited energy is, is an interesting theoretical problem potentially rich in insights into fundamental physics. However, an understanding of the soft degrees of freedom

is essential to solve it.

Hence, while jet quenching might convince us that QGP is there, it is not a very good tool for measuring its properties and how it changes into normal matter. For this, probes more dependent on soft physics are required.

1.5.3 Direct photon and dilepton production

Historically, the standard way to measure the temperature of a hot medium has been to measure the thermal spectrum of its emitted light. This can be expected to be true for a QGP as well, given the abundance of scattering reactions with quarks and gluons (Kapusta et al. 1991). Of course, the processes under consideration here are energetic enough to allow the emitted photons to produce lepton-antilepton pairs (Kajantie et al. 1986). Photons (γ) and leptons antilepton pairs ($l\bar{l}$) will be emitted in reactions such as



The particularly attractive feature of this signature is that photons and dileptons always emerge from the system without undergoing further not-well understood interactions (energy loss, hadronization etc.) However, the enormous background due to the many short-lived mesons that decay into photons ($\rho, \omega, \eta, \dots$) makes extricating the signal from the background experimentally very difficult. The most interesting result which has come out of this approach so far is CERES's report of observing a dilepton excess (Lenkeit et al. 1999) (see Fig. 1.10). This result was presented by CERN as part of the evidence for its announcement of having found deconfined matter (Heinz and Jacob 2000). However, it is unclear whether

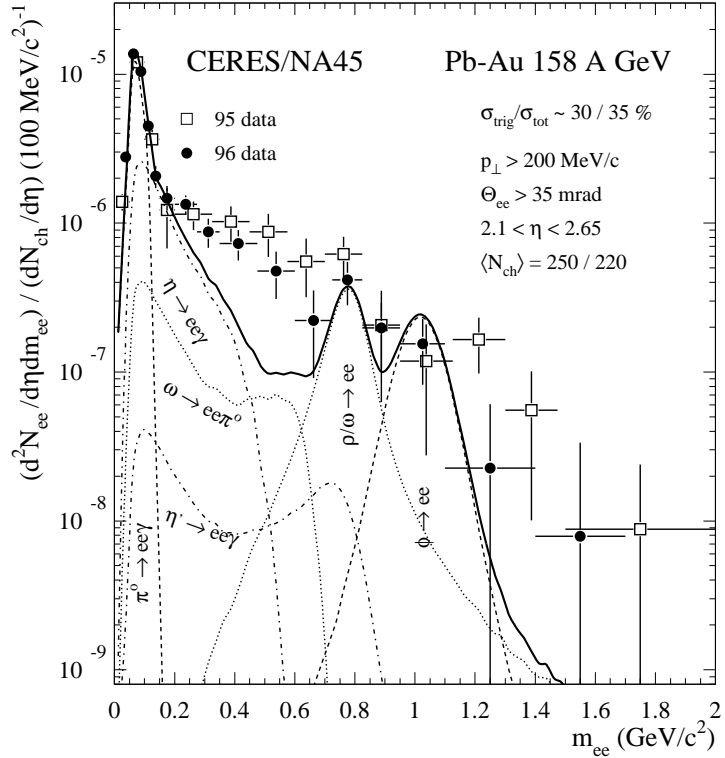


Figure 1.10: The di-electron invariant mass (m_{ee}) distribution observed at CERES, per unit of pseudorapidity (η) and scaled with the total pseudorapidity density of observed charged particles $dN_{ch}/d\eta$. The dotted, dashed and dot-dashed lines represent the expected distribution from electromagnetic decays of known resonances. An excess is observed at $m_{ee} \sim 0.7$.

it signals a dilepton excess due to QGP or, rather, a shift in the ρ peak due to partial chiral symmetry restoration. Measurement of photons/dileptons is part of the planned ALICE program, where it can be a very useful probe if correlated with jet-quenching (Gale et al. 2004). The energetic reactions in Eq. (1.42) could produce a detectable photon/dilepton pair together with either a detectable, partially quenched, or totally quenched jet. The correlation will then be a powerful tomography tool.

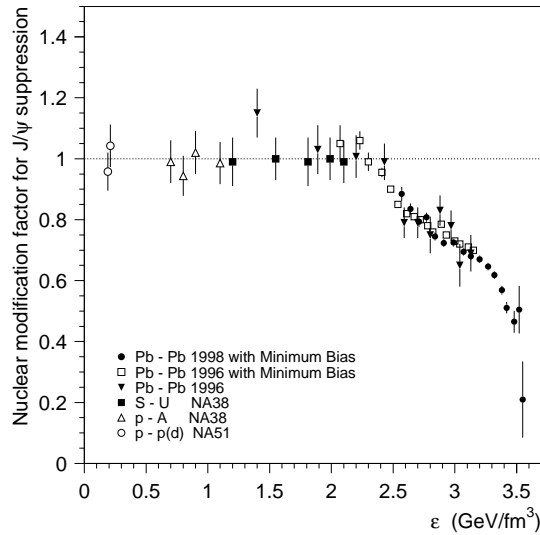


Figure 1.11: Nuclear modification factor (See section 1.5.1) of charmonium particles (detected through the $J/\Psi \rightarrow \mu^+ \mu^-$ decay) It is plotted against the energy density calculated within the Bjorken model ($\propto R_0^2 dN/dy$, where R_0 , the overlapping nuclear area, depends on centrality). Minimum bias means that no centrality selection was performed.

1.5.4 Charmonium suppression

One of the original ways to look for deconfinement is through Charmonium suppression (Matsui and Satz 1986). Charmonium (bound $c\bar{c}$ states, such as $J/\Psi, \Psi', \dots$) can be produced in the initial reactions of an intermediate energy heavy ion collision. Normally, these particles are very narrow (tightly bound) states. However, in a deconfined medium, charmonium pairs will melt due to the color screening provided by the free quarks and gluons. Moreover, different bound states will melt at different temperatures/densities, thus providing an effective QGP thermometer.

The NA50 experiment has indeed detected such a suppression (Abreu et al. 2000) (see Fig. 1.11) which is absent in proton-proton collisions and can not be explained through standard nuclear absorption models. This absorption was one of

the pieces of evidence CERN put forth in its announcement of quark-gluon plasma discovery (Heinz and Jacob 2000).

However, the NA50 experiment cannot detect total charm, but only $J/\Psi \rightarrow \mu\mu$ reactions. Hence, it is possible to adjust nuclear absorption models through in-medium mass modification rather than deconfinement. J/Ψ production is particularly sensitive to such mass shifts since a small modification of its mass will make the $J/\Psi \rightarrow D\bar{D}$ decay possible. In fact, a nuclear absorption model with J/Ψ mass modification does manage to explain the observed J/Ψ suppression (Chaudhuri 2002). The story is not completely over. Other than the fact that the J/Ψ in-medium modification, though reasonable, has never been observed, the nuclear absorption model still can not account for the suppression of the Ψ' .

The NA60 experiment, which will also measure open charm, might shed some light on what exactly causes J/Ψ absorption at SPS energies. Charm data is forthcoming from RHIC and, when it turns on, the LHC (both of which also measure open charm).

As energy increases, we will reach a point where several charm pairs will be produced in each collision. This might change things considerably, since a QGP phase will dissolve the existing $c\bar{c}$ pairs, but will also allow J/Ψ s to form from initially uncorrelated c and \bar{c} at hadronization (Thews et al. 2001). This means that the number of J/Ψ will become

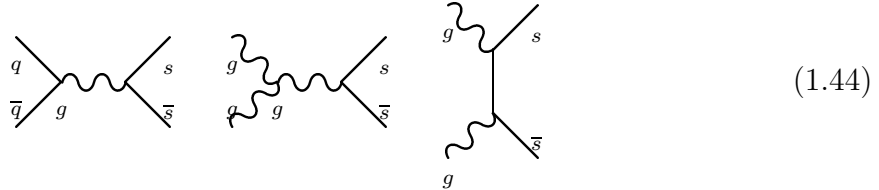
$$N_{J/\Psi} = AN_{c\bar{c}} + BN_{c\bar{c}}^2 \quad (1.43)$$

($B = 0$ if only one $c\bar{c}$ pair is expected per collision). If enough $c\bar{c}$ s are produced, we might observe an enhancement of charmonium produced in heavy ion collisions instead of a suppression (Thews et al. 2001). This is especially true if charm and

bottom quark states (such as the B_c) are also considered, since production of such a state requires initially uncorrelated quark pairs to fuse (Schroedter et al. 2000).

1.5.5 Strangeness enhancement

Strangeness enhancement has long been considered one of the most promising signatures of QGP formation (Rafelski and Muller 1982), as well as a useful tool to study soft matter produced in a heavy ion collision (Rafelski and Letessier 2003a). The basic idea is that $s\bar{s}$ pairs should form much more readily in a QGP than in nuclear collisions through reactions such as



Since gluons are massless and the mass of the light quarks is much less than the QGP temperature, the threshold for forming strange quarks is $2m_s \sim 100-300$ MeV, boosted by chiral symmetry restoration and the abundance of $q\bar{q}$ pairs. In a hadron gas, on the other hand, the threshold energy for the leading strange producing processes



is, respectively, 600 and 800 MeV (note that the first process is also suppressed in a baryon-poor environment).

(Rafelski and Muller 1982; Koch et al. 1986) has shown (Fig. 1.12) that in a thermalized gluon-rich perturbative QGP the $s\bar{s}$ production rate is as much as an order of magnitude greater than the strangeness production rate in a hadron gas at a similar temperature, with gluon-gluon fusion reactions accounting for a

large majority of the production. Due to the faster equilibration time and greater

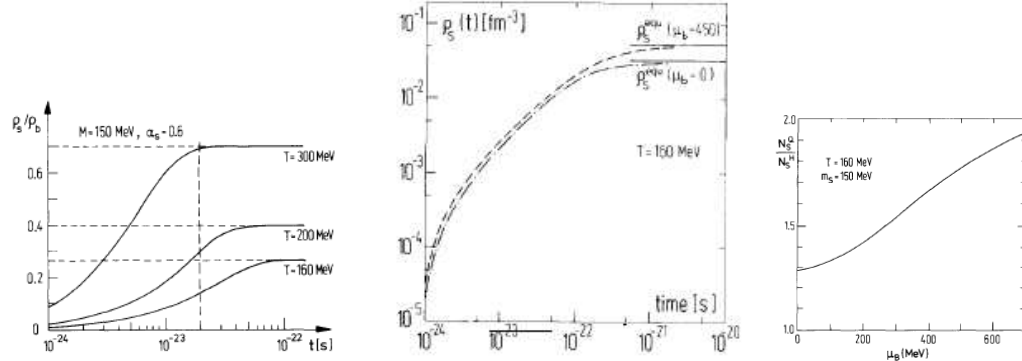


Figure 1.12: Density of strange quarks with respect to time calculated in a QGP (left, normalized to baryon density with $m_s=150\text{MeV}$) and a hadron gas (middle) kinetic production models. As can be seen, equilibration time is significantly shorter for the QGP phase. In addition, as the panel on the right shows, equilibrium strangeness quark content will be stronger in the QGP phase at all chemical potentials.

equilibrium strange quark density, therefore, a system which has undergone a QGP phase transition will exhibit an enhancement of strange quarks with respect to a system which has not. This enhancement will translate into an even greater enhancement of strange hadrons after hadronization. Multi-strange hadrons (ϕ, Ξ, Ω) and their anti-particles will be particularly enhanced, since their production in a hadron gas has a particularly high energy threshold ($p\bar{p} \rightarrow \Omega\bar{\Omega}$, requiring protons with momentum of 700MeV each) or a sequence of many reactions (e.g. $\pi\bar{p} \rightarrow K\bar{\Lambda}, \pi\bar{\Lambda} \rightarrow K\bar{\Xi}, \pi\bar{\Xi} \rightarrow K\bar{\Omega}$). In a hadronizing strangeness-rich QGP, on the other hand, multi-strange baryons form by recombination of strange quarks, and should not be as suppressed according to most hadronization models (Fig. 1.13 left).

Hence, to test for QGP one has to look for strange particles in a nucleus-nucleus collision and compare with p-A or p-p. A clear enhancement, significantly

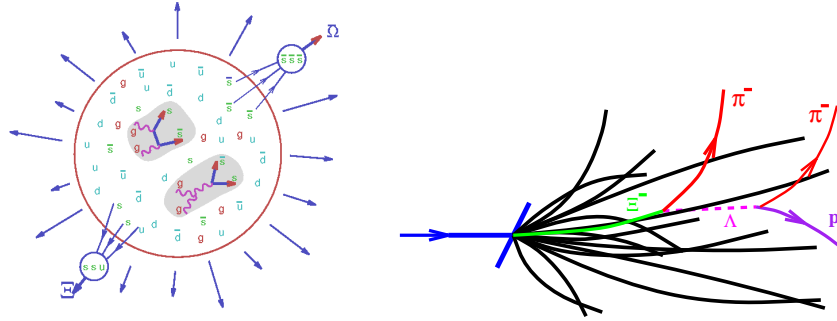


Figure 1.13: Left: Production of multi-strange hadrons through combination of strange quarks from a QGP. Right: Detection of strange particles from a heavy ion collision due to decay topology.

raising with particle strangeness content, would constitute evidence for deconfinement. Experimentally, this is facilitated by the fact that strange particles decay weakly, with a lifetime comparable to the time of flight. Hence, they can be reconstructed through decay topology (Fig. 1.13 right).

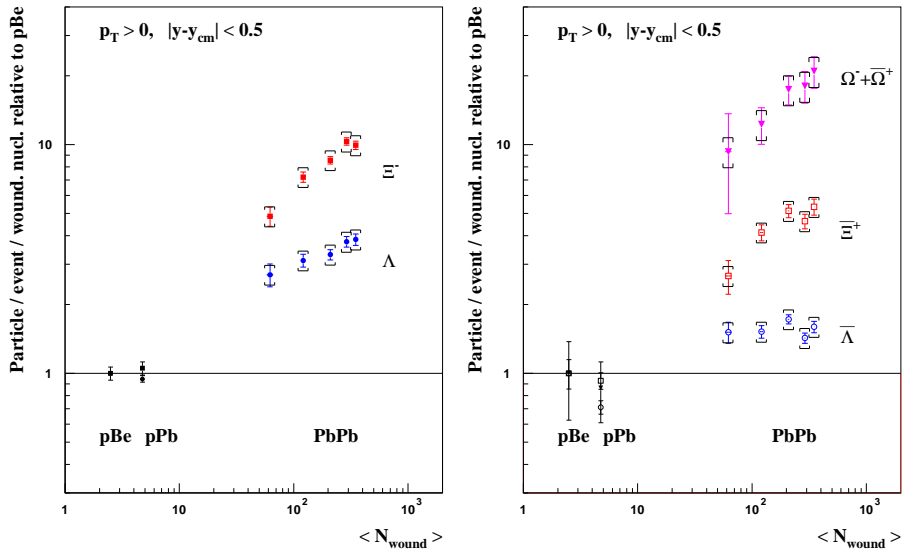


Figure 1.14: The nuclear modification factor (see section 1.5.1) for the production of hyperons as measured by the NA57 experiment, normalized by the number of participants. Particle yields for p-p and Pb-Pb collisions are compared to p-Be, plotted against the number of participants, calculated within the Wounded nucleon model (see section 1.5.1).

As Fig. 1.14 shows, a very clear experimental enhancement has indeed been detected by the WA97 and NA57 collaborations (Andersen et al. 1999) (whose narrow-acceptance telescope is particularly suited to look for multi-strange particles). The enhancement in all strange particles, and its rise with strangeness content, constituted a crucial part of the supporting evidence for CERN's claim to have produced deconfined matter (Heinz and Jacob 2000). Microscopic nuclear interaction models have so far been unable to even come close to reproducing the observed enhancement (Antinori et al. 1999).

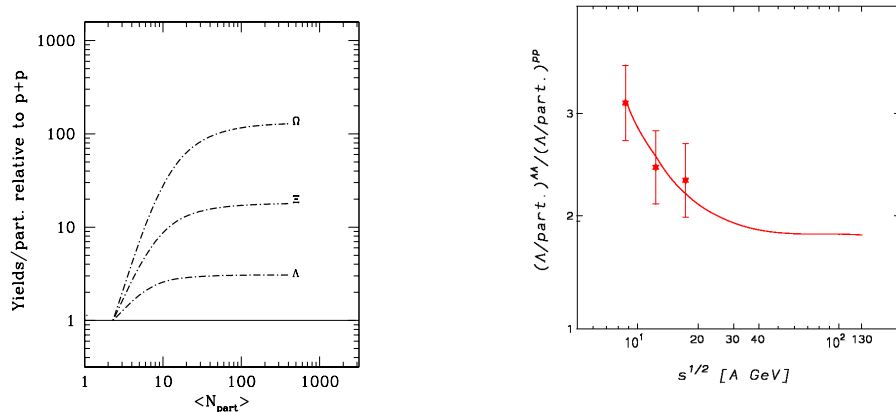


Figure 1.15: Nuclear modification factor for Λ (right) and Λ, Ξ, Ω (left) production calculated within a canonical statistical hadronization model. The result is plotted against the number of participants N_{part} (left) and center of mass collision energy per nucleon (right).

One alternative explanation which would account for the observed enhancement pattern is canonical suppression (Tounsi et al. 2003). Postulating that collisions in p-p and p-A systems achieve chemical equilibration, the small volume of these systems necessitates that the canonical (rather than grand-canonical) ensemble be used to calculate strange particle yields. This means that, rather than

introducing a chemical potential for strangeness, only outgoing states with exact strangeness conservation are counted in the statistical averaging. As Fig. 1.15 shows, this leads to a sharp drop in strangeness as system volume decreases below a critical value, with the effect being greater as strangeness content increases.

This explanation, however, has several problems. For a start, it is not at all clear that equilibrium statistical mechanics can be used to describe a p-p and p-A system. NA57 p-p and p-Pb data are well described through the uRQMD nuclear microscopic model (Antinori et al. 1999), where chemical equilibration is not assumed or indeed predicted.

In addition, as Fig. 1.15 (left) shows, the pattern of enhancement is not predicted correctly by the canonical picture: the canonical picture has a sharp suppression at small volume and a long plateau as volume becomes large and the canonical and grand-canonical pictures coincide. Experimentally, however, strangeness scales linearly with number of participants in all (p-p,p-Be,p-Pb,Pb-Pb) collisions. The scaling in the Pb-Pb system is steeper, but still linear with centrality, in accordance with a higher $s\bar{s}$ production per unit volume per unit time. This is expected from QGP-based kinetic production (Rafelski and Letessier 2002).

A final distinguishing test between canonical suppression and QGP production is to lower the collision energy. As Fig. 1.15 (right) shows, the canonical model predicts an increase of enhancement (going to ∞ as the collision energy approaches the Ξ and Ω threshold). The QGP model predicts a decrease, with a sharp discontinuity at the energy where the QGP is not formed anymore. Lower energy SPS runs will shortly measure the energy dependence of enhancement and definitely clarify the situation.

1.5.6 Collectivity

The argument used in the derivation of strangeness enhancement can also be applied to argue that in a quark-gluon plasma system local thermal equilibrium will be reached on a much shorter timescale than in a system with hadronic degrees of freedom. Hence, the fact that most soft observables can be described through collective dynamics (thermo and hydrodynamics) is a good indication that QGP has formed. Are the particle yields described by a temperature and chemical potential? Are particle momentum distributions characterized by one temperature and collective flow? How well does a hydrodynamic approach describe the system? A good part of the subsequent chapters will be devoted to addressing these topics, so we will not dwell on them in detail here beyond mentioning some motivational issues.

Any system, including a hadronic gas, will evolve collectively if given enough time. However, a quark-gluon plasma, with its light colored degrees of freedom, should be much more efficient as an entropy generator than a hadron gas. Hence, we should expect a much stronger collective signal in a QGP than in a collection of hadrons.

In this respect, we shall mention that microscopic hadronic simulations (Bratkovskaya et al. 2004) show that hadronic systems at SPS and RHIC energies do not have the time to develop a significant amount of collective flow, and hence mass dependence of the apparent temperature (inverse slope of the logarithm of the transverse mass distribution) should not be large. This is true for p-p but not A-A data (see Fig. 1.16). This is even more true in the case of anisotropic flow (discussed in detail in chapter 6). The evolution of anisotropy is described so well by the hydrodynamic picture that a very early system thermalization is required

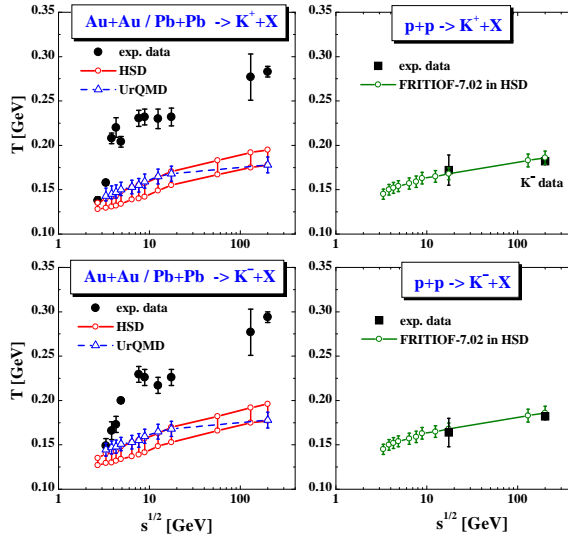


Figure 1.16: Mass dependence of the apparent temperature (inverse slope in a logarithmic graph) as calculated by uRQMD and HSD models (see section 1.5.1 for references).

(Heinz and Kolb 2002). It is very difficult to see how a hadronic model could achieve such a short thermalization timescale.

It should also be mentioned that statistical production from an entropy-rich QGP is likely to look quite different from freeze-out of an interacting hadron gas. In case of a first-order phase transition or sharp cross-over, the system might evolve out of equilibrium at the transition, and post-phase transition interactions can potentially destroy evidence for the earlier equilibration. Given this, it is remarkable that several experiments found particles and antiparticles to have exactly the same inverse slopes (Bruno et al. 2003) (see Fig. 1.17). In an interacting hadron gas, anti-particles should annihilate at a strongly p_T dependent cross-section.

Because of the large amount of entropy expected to be generated through QGP equilibration, it has also been suggested that to find the phase transition we should look for a jump in the entropy per strangeness, entropy per baryon number,

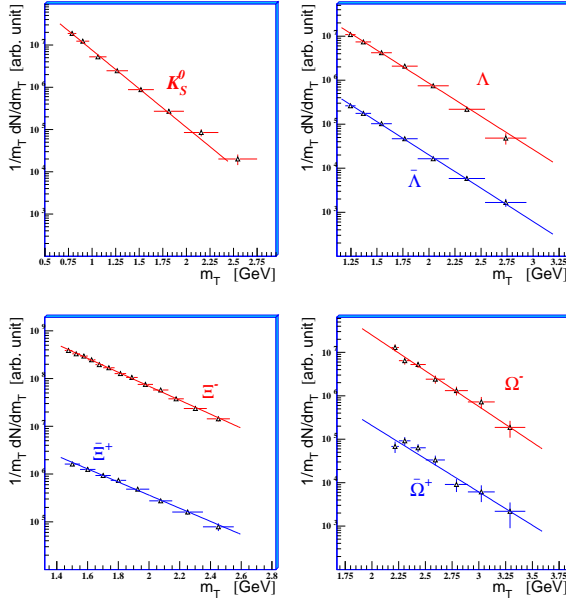


Figure 1.17: Transverse mass distributions for particle and anti-particles as measured by the WA97 experiment .

or entropy per energy (Letessier et al. 1992). A recent systematic experimental study (Gazdzicki 2004) uses this reasoning to cite the kink observed in π (\sim entropy) production at ~ 4 GeV (see Fig. 1.18 (Left)) as well as the flattening of the K/π ratio (see Fig. 1.18 (right)) as evidence for deconfinement.

1.5.7 QGP evolution

Concluding this overview of signatures, it is necessary to underline one of the most remarkable, and problematic aspects of the study of QGP in heavy ion collisions: the range of physical approaches which needs to be implemented to study the system. At each stage of the system's evolution, the relevant physics and useful approximations are in general completely different from that of the other phases. In addition, different signatures probe different stages of this evolution.

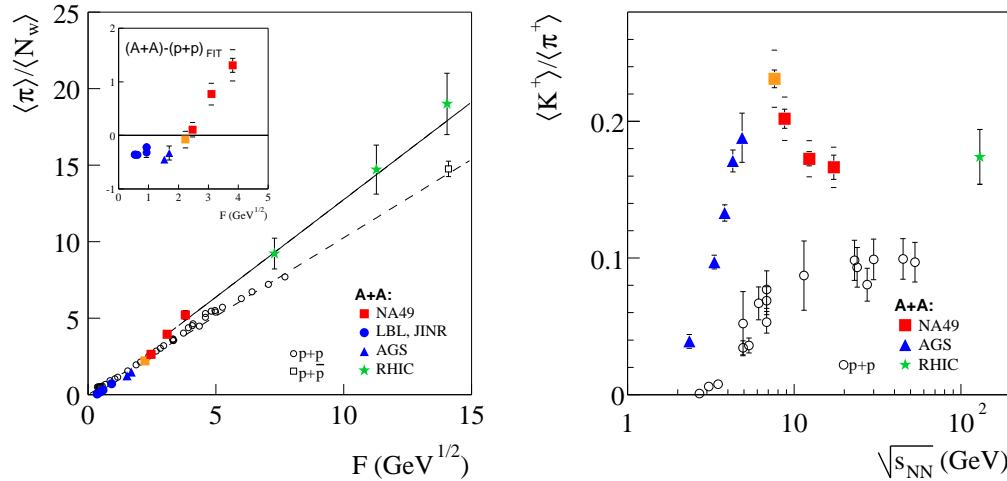


Figure 1.18: Left: π production per wounded-nucleus a function of energy for A-A vs p-p collisions, plotted against Fermi's energy measure $F = (\sqrt{s_{NN}} - 2m_N)^{3/4} / \sqrt{s_{NN}}^{1/4}$, where $\sqrt{s_{NN}}$ is the average of the center of mass energy per nucleon-nucleon collision. Right: K/π ratio in nucleus-nucleus collisions as a function of $\sqrt{s_{NN}}$.

We shall give a chronological layout of the possible evolution of a QGP fireball, together with the methods which can be used to describe it.

Initial collision The short and energetic initial collision is usually approximated through a parton cascade model (Geiger 1993). In this picture, the colliding partons are described as flat “pancakes” of quarks and gluons, with the structure functions extrapolated from nucleus deep inelastic scattering. The collision dynamics is then governed by pQCD.

Recently, an alternative/complementary approach has emerged: That of the Color Glass Condensate (Iancu et al. 2002). From saturation physics one can argue that at high energy heavy ion collisions the gluon occupation number is significantly larger than one. Hence, the colliding system can be modeled as an incoherent classical $SU(3)$ field.

Hydrodynamic evolution Somehow (the details are not entirely clear), the initial system reaches local thermal equilibrium in a (hopefully!) deconfined phase. In this case, thermalization times will be very fast (Rafelski and Muller 1982) and hence the mean free path very small. The bulk evolution of the system can then be optimally described by relativistic hydrodynamics.

As we shall see later in the thesis, however, thermal and chemical equilibrium can be two very different things. Chemical equilibration is therefore not necessarily as fast, and in fact does not necessarily occur for all quantities. This aspect of QGP evolution is best modeled by transport theory, with the collision terms given by quantum field theory (Rafelski and Muller 1982),(Kapusta et al. 1991),(Wang et al. 1995).

Hadronization This is the big unknown. Quite simply, there is no rigorous physical way to approach it. It is non-perturbative, so Feynman diagrams will not work. It is also likely to be a far from equilibrium process, so it is doubtful that lattice QCD will work as more than a qualitative indication of what's going on.

All we are left are effective models, based on basic physics such as thermodynamics, relativity and conservation laws. One way to make quantitative predictions is entropy maximization. This leads to statistical hadronization, the subject of this thesis. Another recently proposed ansatz is the coalescence/recombination of partons (Fries et al. 2003). This picture has been proven to explain a range of phenomena at intermediate p_T . However, it cannot as yet be formulated self-consistently in a soft regime, where particle mass

is non-negligible, as it violates energy-momentum conservation (as well as entropy non-decrease). Perhaps, in the future, it will be possible to combine this approach with statistical hadronization (Biro and Muller 2004).

It should be noted that some observables described in this section do not have to undergo hadronization. Photons and dileptons leave the QGP with no further interactions. The impact of hadronization on jets is also dynamically not relevant. Since hadronization is a soft process, it will not change the momentum distribution of the jet significantly, but will simply “dress” the outgoing quark in a hadronic coating.

Soft probes (strangeness, charm, collectivity), on the other hand, will undergo a potentially non-trivial hadronization before reaching the observer. This means understanding hadronization is a crucial step in understanding soft physics. It also means, however, that soft probes are tools in understanding the phase transition from a quark-gluon plasma to a hadron gas.

Post-hadronization evolution It is far from obvious that hadrons stop interacting after they form. In fact, one of the most important questions one can ask about hadronization is the extent of interactions which follow it.

One thing which is certain is that hadronic phase space is very different from quark-gluon plasma phase space. Hence, an equilibrated quark-gluon plasma will probably produce an out-of-equilibrium hadron gas. Equilibration times for a hadron gas are much slower than for a QGP, since the lightest color-neutral boson has a mass of 137 MeV. Hence, the best way to analyze such a system is through transport theory. Collision terms are measured experimentally in elementary collisions or calculated through effective field theory

techniques. Quantum molecular dynamics models (Bass et al. 1998; Ehehalt and Cassing 1996) are based on this approach.

Final freeze-out At this stage, particles decouple from the system and reach the observer. It is sometimes fashionable to talk about a “chemical freeze-out” (when inelastic collisions cease) and “thermal freeze-out” (when particles stop interacting altogether). A look at particle reaction data shows that this description is inappropriate: Inelastic reactions, such as strange quark exchange, can be just as low-threshold as elastic hadronic reactions. It is better to talk about hadronization (when hadrons become appropriate degrees of freedom) and freeze-out.

1.6 The scope of this thesis

This thesis, therefore, explores the effect of statistical hadronization on the observed soft particle abundances and spectra in heavy ion collision. We shall concentrate on hyperons, given their relevance to strangeness enhancement. However, non-strange hadrons shall also be examined.

We shall use experimental data (from SPS and RHIC) to constrain the statistical hadronization picture, and differentiate between freeze-out scenarios. We will test these scenario’s ability to constrain both hadron yields and spectra, as well as direct detection of unstable short-lived resonances.

Some of the questions which we would like to ask are:

- What are the temperature and chemical potentials characterizing the system?

- Is there evidence of transverse flow and other collective effects?
- Does statistical hadronization happen in chemical equilibrium, or are non-equilibrium effects important?
- What is the dynamics of statistical hadronization? How does particle emission proceed in spacetime?
- What is the significance of the post-hadronization interacting hadron gas phase? What is its impact on observables?
- What is the experimental data's sensitivity to these observables? What is the significance of fit results, and how can they be further confirmed?

In the second chapter, we shall review relativistic statistical mechanics and how it applies to hadronization. We shall also describe how a variety of different freeze-out scenarios arise out of statistical hadronization. In chapters 3 and 4 we will use statistical hadronization to describe particle spectra measured, respectively, in SPS and RHIC experiments. In chapter 5, we will use yields of short-lived resonances as a way to differentiate between the different freeze-out models and to constrain freeze-out dynamics. In chapter 6 we shall use azimuthal asymmetry in less than central collisions as a tool to study freeze-out. Finally, we will give a few conclusions and an outlook on unresolved issues.

CHAPTER 2

Statistical hadronization: an overview

2.1 Introduction

The use of statistical mechanics to describe production of strongly interacting particles was pioneered by Fermi (Fermi 1950) and developed by Pomeranchuk (Pomeranchuk 1951), Landau (Landau 1953) and Hagedorn (Hagedorn 1965). Indeed, Hagedorn’s observation (Hagedorn 1965) that an infinite number of hadrons of increasing mass leads to an exponential density of states, and hence to a critical temperature where the canonical partition function diverges, provided a piece of evidence for a QCD phase transition before even the discovery of quarks.

The basic idea of this approach is that in a high-energy process driven by strong interaction a large number of particles is likely to be produced (Fermi 1950). In these circumstances, the dynamic part of the reaction cross-section will average out, and be considered a “volume” constant. The distribution of each particle (1...N) will then be given by the corresponding phase space weight ¹

$$dN_1 \propto \prod_{i=2}^N \int \frac{d^3 p_i}{E_i} \delta(p_{total}^\mu - \sum_{i=1}^N p_i^\mu) \quad (2.1)$$

It can be shown (Fermi 1950; Hagedorn 1965; Rischke 2002) that in the many-body infinite energy limit this distribution approaches an exponential, with the slope

¹See appendix C

related to the energy per particle (canonical limit). If the phase space in Eq. (2.1) also provides for quantum number conservation, it becomes possible to derive a grand-canonical limit.

The statistical model has been applied to every experimentally studied strongly interacting system, from $e^+e^- \rightarrow \text{hadrons}$ to heavy ions (Becattini et al. 2003). It is not obvious, however, that particles described by such a statistical model are effectively thermalized. In particular, a quark-gluon plasma, should exhibit a further degree of equilibration: The fact that its composed of colored, massless degrees of freedom means it should achieve local thermalization in a timescale considerably shorter than its evolution. It is therefore expected that the QGP evolves as a continuous fluid.

2.2 Thermodynamics and hydrodynamics from Kinetic theory

Thermodynamics and hydrodynamics also arise as a $\tau \rightarrow \infty$ limit to the Boltzmann transport equation governing many-particle distributions

$$\frac{df(x, p)}{d\tau} = \left(\frac{1}{m} p^\mu \frac{\partial}{\partial x^\mu} + F^\mu \frac{\partial}{\partial p^\mu} \right) f(x, p) = C[f](x, p) \quad (2.2)$$

Where $C[f]$ is the Entropy-generating particle collision term. We can describe the collision term semi-classically, by taking the cross-sections calculated in quantum field theory $\sigma(P, P' \rightarrow p, p')$ but assuming that the distributions of the particles are uncorrelated beyond Quantum statistics requirements. For a theory invariant

under time reversal, and considering just two body interactions²

$$c[f](x, p) = \int d^3[x', X, X', p, P, P'] \delta^4(P + P' - p - p') \sigma(P, P' \Leftrightarrow p, p') \quad (2.3)$$

$$\{[f(X, P)f(X', P') + Ff(X, P')f(X', P)] - [f(x, p)f(x', p') + Ff(x, p')f(x', p)]\}$$

where F ensures the Fermion-Boson anti-symmetrization requirement

$$F = \begin{cases} -1 & \text{Fermions} \\ 1 & \text{Bosons} \\ 0 & \text{Boltzmann(Distinguishable)} \end{cases} \quad (2.4)$$

The Boltzmann H-theorem, generalized to quantum statistics (Lifshitz and Pitaevskii 1981) states that Entropy

$$S = \int d^3[x', X, X', p, P, P'] (-f(x, p) \ln[f(x, p)] - F(1 + Ff(x, p)) \ln[1 + Ff(x, p)]) \quad (2.5)$$

will always monotonically increase, until detailed balance is reached, $C[f]$ will go to 0 and f reduces to the entropy-maximizing Fermi-Dirac, Bose Einstein or Maxwell-Boltzmann distribution

$$f_0(p^\mu, x) = \frac{1}{\lambda_q^{-1} e^{u_\mu(x)p^\mu/T} + F} = \sum_{n=1}^{\infty} F^{n-1} \lambda_q^n e^{nu_\mu p^\mu/T} \quad (2.6)$$

This will happen after “many” collisions will have taken place

$$\tau_\infty >> \frac{1}{\langle \sigma \rangle \langle \frac{N}{V} \rangle} \quad (2.7)$$

(τ_∞ is actually reached quite quickly in a strongly interacting system with high particle density)

²In general, the frequency of many-body interactions goes as a power of the mean-free-path, $\langle \sigma \rangle_{n_{body}} (\langle N/V \rangle)^{-n_{body}}$. Hence, $C[f]$ is actually a perturbative series and Eq. (2.3) is the first term. Both a QGP (Rafelski and Muller 1982) and a hadron gas (Bass et al. 1998) have been described using just the two-body term. However, this approach will break down in the non-perturbative limit, or equivalently when long-range correlations become too large for the semi-classical approximation. A QGP hadronization can not therefore be described this way.

f_0 in Eq. (2.6) is characterized by temperature T and fugacity λ , as well as $u^\mu(x) = \gamma(1, \vec{v})$, the 4-velocity vector representing the motion of the volume element. If the interactions will be strong enough that the mean free path of the particles is negligible with respect to the collective motion motion of the system

$$\frac{df(x, p)}{d\tau} \gg \frac{1}{\tau_\infty} \quad (2.8)$$

the system will always have local thermal equilibrium and evolve as a continuous fluid

$$\partial_\mu T^{\mu\nu} = 0 \quad (2.9)$$

$$\partial_\mu n^\mu = 0 \quad (2.10)$$

where $T^{\mu\nu}$ is the energy-momentum tensor and $\partial_\mu n^\mu$ is the number current (for any conserved current such as isospin, strangeness, etc.) We can express these quantities in terms of pressure (P), energy density (ϵ) and number density

$$T^{\mu\nu} = \int \frac{p^\mu p^\nu}{E} f_0(p^\mu, x) = Pg^{\mu\nu} + (P + \epsilon)u^\mu u^\nu \quad (2.11)$$

$$n^\mu = \int n \frac{p^\mu}{E} f_0(p^\mu, x) \quad (2.12)$$

Hence, if we know the equation of state of our fluid we will be able to close our system of equations and evolve the system from any set of initial conditions.

2.3 Statistical hadronization and the Cooper-Frye formula

QGP, with its high number density of strongly interacting particles, is a good candidate for an equilibrated fluid. However, this situation will change in the QGP-HG transition, in which the 10 colored massless partons become over 200 color-neutral hadrons.

The Boltzmann formalism of Eq. (2.2) can not, as far as we can see, be applied to hadronization, since the assumptions that go in it (weakly correlated particles scattering locally) do not apply to a non-perturbative quantum phase transition. However, we know from lattice QCD that hadronization is a relatively fast process, and obviously hadronization of a large thermally equilibrated system can not decrease entropy. For this reason, and the fact that color-neutral hadrons are more weakly interacting than quarks, it is very likely that an equilibrated entropy-rich QGP will emit hadrons according to phase space as described in section 2.1.

If the system is large, energy and quantum number conservation can be accomplished by Lagrange multipliers, so, in the rest-frame with respect to the collective flow the hadrons will be distributed according to f_0 as given in Eq. (2.6).

the post hadronization hadron current will be given by

$$j^\mu = \int d^3p \frac{p^\mu}{E} f_0(u_\mu p_{hadron}^\mu, T, \lambda_{hadron}) \quad (2.13)$$

where the Hadron fugacity is given by the product of the fugacities of its constituent quarks quantum (not necessarily the QGP's chemical potentials, as we'll see later)

$$\lambda_{hadron} = \prod_q \lambda_q \quad (2.14)$$

Using the “fast hadronization” assumption again, we can define a “Freeze-out hypersurface” defining a locus in space-time from which these statistically hadronizing particles are emitted, labeled by a 4-vector Σ^μ . Since Σ^μ is a 3-surface in Minkowski 4-space, it can always be expressed as a function of three parameters (u, v, w) . Its element can then be given in a Lorentz-covariant way using Stokes's theorem

$$d^3\Sigma_\mu = \epsilon_{\mu\nu\alpha\beta} \frac{\partial\Sigma^\nu}{\partial u} \frac{\partial\Sigma^\alpha}{\partial v} \frac{\partial\Sigma^\beta}{\partial w} \quad (2.15)$$

where $\epsilon_{\mu\nu\alpha\beta}$ is the Levi-Civita symbol. the number of particles produced in such a volume element is then Lorentz-invariant, and computable in the volume element's rest frame as

$$j_\mu d^3\Sigma^\mu = dN \quad (2.16)$$

combining Eq. (2.13) and Eq. (2.16) we obtain the famous Lorentz-Invariant Cooper-Frye formula (Cooper and Frye 1974)

$$E \frac{dN}{d^3p} = \int d^3\Sigma_\mu p^\mu f(p_\mu u^\mu, T, \lambda) \quad (2.17)$$

If hadronization of the full volume takes a lot of time, the emitted particle can find itself in the QGP again if $p^\mu \Sigma_\mu < 0$. It is still unclear how to handle this in a rigorous way, but typically one just truncates the distribution to exclude this unphysical region (perhaps adjusting the limits of integration to conserve energy, entropy etc.) (Bugaev 1996),(Anderlik et al. 1999)

$$E \frac{dN}{d^3p} = \int d^3\Sigma_\mu p^\mu f(p_\mu u^\mu, T, \lambda) \Theta(\Sigma_\mu p^\mu) \quad (2.18)$$

where $\Theta(x)$ is the step function.

Since all hadrons apart from the pion are considerably heavier than the typical hadronization temperature ($p_\mu u^\mu > m >> T$), the sum in Eq. (2.6) can be truncated at $n=0$, corresponding to the Boltzmann approximation

$$f(p_\mu) = \lambda e^{-p_\mu u^\mu / T} \quad (2.19)$$

2.3.1 Total particle yields

If the thermodynamic parameters T, λ do not vary within the hadronizing volume, the total number of particles will be independent of Σ^μ and u^μ . To see this, we

integrate the Cooper-Frye formula over momentum space

$$N = \int dN = \int \frac{d^3p}{E} p^\mu d^3\Sigma_\mu \lambda e^{p_\mu u^\mu / T} \quad (2.20)$$

and insert a $u_\mu u^\mu$ ($= 1$) in the integrand. The two integrals then decouple

$$N = \left[\int d^3\Sigma_\mu u^\mu \right] \left[\int d^3p \frac{p^\mu u_\mu}{E} e^{p_\mu u^\mu / T} \right] \quad (2.21)$$

The first integral is just a normalization constant. Since $p^\mu u_\mu = E_{rest}$, we are left with

$$N = Vg \int d^3p \lambda e^{-\sqrt{p^2+m^2}/T} \quad (2.22)$$

where g is the particle degeneracy (For a colorless particle, it will be equal to $2S+1$ where S is the spin)³. Using the Bessel function definition (Gradshteyn and Ryzhik 1989)

$$K_n(x) = \frac{2^n n!}{(2n)!} x^{-n} \int_0^\infty \frac{dz}{\sqrt{z^2+x^2}} z^{2n} e^{-\sqrt{z^2+x^2}} \quad (2.23)$$

we can find N analytically

$$N = g \frac{4\pi}{(2\pi)^3} m^2 \lambda T K_2 \left(\frac{m}{T} \right) \quad (2.24)$$

The energy density in a rest frame with respect to the collective flow also follows

$$\epsilon = \int d^3p \sqrt{p^2+m^2} \lambda e^{-\sqrt{p^2+m^2}/T} = g \frac{4\pi}{(2\pi)^3} m^3 \lambda T \left(\frac{3T}{m} K_2 \left(\frac{m}{T} \right) + K_1 \left(\frac{m}{T} \right) \right) \quad (2.25)$$

Comparing Eq. (2.19) and Eq. (2.6) it can be seen that these formulae can be generalized to the Fermi-Dirac and Bose-Einstein distribution by the substitution

$$\lambda T K_l \left(\frac{m}{T} \right) \rightarrow \sum_{n=1}^{\infty} (\pm 1)^{n+1} \frac{T}{n} \lambda^n K_l \left(\frac{nm}{T} \right) \quad (2.26)$$

³It is perhaps not immediately intuitive how a non interacting gas dispersion relation can be used to describe a strongly interacting system. The “trick”, here, is that we will generate all the strongly excited states (resonances) in the data book, and the strong interaction excited states can be considered, to a good approximation, as narrow resonances. As was explicitly shown (Dashen and Rajaraman 1974) if resonances are narrow enough, an ideal gas of resonances is an appropriate description. As this section shows, our approximation can be improved through finite width effects

If the particle has a finite width, the Bessel function will be further integrated over the range of masses to take the mass spread into account. For a resonance with width, we obtain

$$N_i(m_i) \rightarrow \frac{1}{N_0} \sum_{\forall i \rightarrow j} \int_{m_{threshold}}^{\infty} n_i(M) F_{\Gamma}(M, \Gamma_i(b_{i \rightarrow j}, M)) dM \quad (2.27)$$

where

- $b_{i \rightarrow j}$ is the decays branching ratio
- $m_{threshold}$ is the threshold mass for the decay, $\sum_j m_j$
- $F_{\Gamma}(M, \Gamma_i) = \frac{\Gamma \Gamma_i}{(M - m_i)^2 + \Gamma_i^2/4}$ is the Breit-Wigner formula
- $\Gamma_i(b_{i \rightarrow j}, M)$ is the energy-dependent width for the decay under consideration.

In general, this is a non-trivial particle dependent function. Here, we only consider the dominant energy dependence of the width, namely the decay threshold energy phase space factor. The explicit form for decays with low relative angular momentum has been studied through corresponding reverse production cross-sections, and found to be (Terazawa 1995; Gounaris and Sakurai 1968; Pratt and Bauer 2003)

$$\Gamma_i(b_{i \rightarrow j}, M) = b_{i \rightarrow j} \left[1 - \left(\frac{m_{threshold}}{m} \right)^2 \right]^{l+\frac{1}{2}} \Gamma^* \quad (2.28)$$

where l is the relative angular momentum of the decay and Γ^* is the energy-independent constant found in the particle data book (Hagiwara et al. 2002)

N_0 is the Breit-Wigner and phase space normalization

$$N = \int_{m_{threshold}}^{\infty} F_{breit-wigner}(M, \Gamma_i(b_{i \rightarrow j}, M)) dM \quad (2.29)$$

$$= \int_{m_{threshold}}^{m_1} F_{breit-wigner}(M, \Gamma_i(b_{i \rightarrow j}, M)) dM + \int_0^1 \frac{m_1 \Gamma_i(b_{i \rightarrow j}, \frac{m_1}{z})}{(m_1 - m_i z)^2 + \frac{\Gamma^2(b_{i \rightarrow j}, \frac{m_1}{z}) z^2}{4}} dz^4$$

2.4 Treatment of resonance decays

Most of the 200 particles produced in statistical hadronization will be short-lived resonances, whose decay is undetectable through an analysis of the particle trajectories as it happens after the particle was produced. More complicated cascades, with sequential decays, are also possible. While the number of particles made from these decays is suppressed by the high mass of the resonance, they are also enhanced by resonance's typically high spin degeneracy and the fact that many particles are produced in a typical decay (Fig. (2.1) left).

The expected yield of observed “light” particles will then have to include the products of all resonance decays of short-lived products. As Fig. 2.1 (right) shows, there is no way that this contribution can be neglected. However, on the bright side, resonances are an important tool for QGP diagnostics: Since their quark numbers are the same as the base particles, their relative abundance is controlled by the temperature only. Their abundance is also sensitive to post-hadronization dynamics (see chapter 5). In short, resonances will be a very sensitive freeze-out probe, one which will be explored from different angles in the next chapters of this thesis.

⁴This change of variables, $\frac{m_1}{m} = z$, used within our programs, is absolutely essential for the numerical evaluation of the integral. Otherwise, the result will be plagued by Γ -dependent systematic errors, since N converges slowly as the upper limit of the numerical integration $\rightarrow \infty$. On the other hand, the integral with changed variables is also prone to error if the width is too small, since the Gaussian integration might miss the peak. The solution, which our calculations implement (Torrieri et al. 2004), is to split the integral in two parts: $\int_{m_{threshold}}^{\infty} = \int_{m_{threshold}}^{m_0+2\Gamma} + \int_{m_0+2\Gamma}^{\infty}$. The first part can be done through conventional integration, the second through variable change

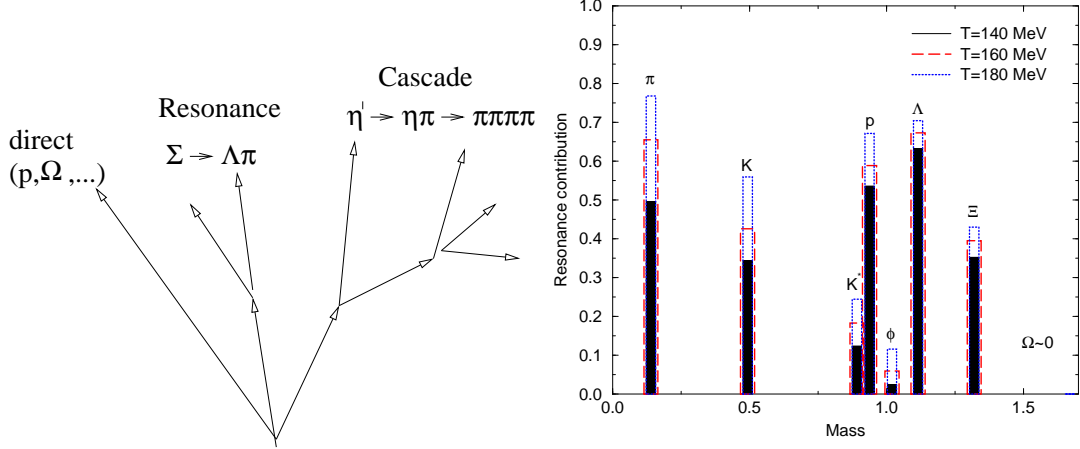


Figure 2.1: Left: Typical resonance decay patterns. Right: Resonance contribution to observed particle yield as a function of freeze-out temperature .

To include resonances in particle yields and ratios, it is enough to sum the resonance decay products to the base yields

$$N_i \rightarrow N_i + \sum_{\forall j \rightarrow i+...} b_{j \rightarrow i+...} N_j \quad (2.30)$$

where N_i is given as in Eq. (2.24) and $b_{j \rightarrow i+...}$ is the branching ratio. The only technical difficulty in this calculation is that decay products in the particle data book (Hagiwara et al. 2002) are given up to Clebsh-Gordan coefficient factor of Isospin. In case of two-body decays, we calculated C-G coefficients automatically using the algorithms in CERNLIB (Various 1999). Three body decays, are a bit more problematic, since there are several possible ways of combining partial isospin sums. We averaged over these, giving $(J, m_a$ and j_i, m_i refer to the total and z

isospin components of the resonance and decay products respectively)

$$b_{j \rightarrow 12} = b_{0 \rightarrow 12}^0 (\langle J_0 m_0 | j_1 j_2 m_1 m_2 \rangle)^2 \quad (2.31)$$

$$\begin{aligned} b_{j \rightarrow 123} &= b_{0 \rightarrow 123}^0 \frac{1}{3} \left[\sum_{j_{12}} (\langle J_{12} m_{12} | j_1 j_2 m_1 m_2 \rangle \langle J_0 m_0 | j_{12} j_3 m_{12} m_3 \rangle)^2 \right. \\ &\quad + \sum_{j_{13}} (\langle J_{13} m_{13} | j_1 j_3 m_1 m_3 \rangle \langle J_0 m_0 | j_{13} j_2 m_{13} m_2 \rangle)^2 \\ &\quad \left. + \sum_{j_{23}} (\langle J_{23} m_{23} | j_2 j_3 m_2 m_3 \rangle \langle J_0 m_0 | j_{23} j_1 m_{23} m_1 \rangle)^2 \right] \end{aligned} \quad (2.32)$$

2.4.1 Spectra

The contribution of resonances to particle spectra is non-trivial, since the full kinematics of the decay has to be understood. However, the resonance contribution to spectra is where the data is really sensitive to freeze-out dynamics since post-hadronization interactions might re-thermalize resonance decay products. Hence, searching for a bona-fide resonance contribution which could be reconstructed by invariant mass is a stringent test of fast statistical freeze-out.

In analogy with Eq. (2.30) we assume that

$$E_1 \frac{dN_1}{d^3 p_1} = \left(E_1 \frac{dN_1}{d^3 p_1} \right)_{direct} + \sum_{\forall j \rightarrow 12..n} \left(E_1 \frac{dN_1}{d^3 p_1} \right)_{j \rightarrow 12..n} \quad (2.33)$$

where the first term is given by the Cooper-Frye formula and the second gives the distribution of decay products in a cascade. Assuming j is also produced through statistical hadronization, all is left is to find $E_1 \frac{dN_1}{d^3 p_1}$ in terms of $E_j \frac{dN_j}{d^3 p_j}$ (which will again be given by the Cooper-Frye formula. The relations we will develop will themselves be recursive, to handle the case when j has a cascade component).

We shall assume that all the short-lived resonances have decayed. We shall also assume that lots of particles are emitted in all directions, thereby averaging

over any matrix-element dependence on factors such as spin. The distribution of the resonance decay product momenta will then be given simply by the integral over the available region of the Lorentz-invariant phase space⁵.

$$\left(E_1 \frac{d^3 N_1}{d^3 p_1} \right)_{j \rightarrow 12..n} = B \int \frac{d^3 p_j}{2E_j} \int T_n \left(E_j \frac{d^3 N_j}{d^3 p_j} \right) \quad (2.34)$$

$$T_n = \prod_{i=2}^n \frac{d^3 p_i}{2E_i} \delta \left(\sum_{i=2}^N p_i - p_1 \right) \delta \left(\sum_{i=2}^N E_i - E_1 - E_j \right) \quad (2.35)$$

B is a normalization factor to make sure that

$$\frac{N_{j \rightarrow 12..n}}{N_j} = b_{j \rightarrow 12..n} \quad (2.36)$$

Two body decay

For a two-body decay, $j \rightarrow 12$, we can go to the resonance's rest frame (denoted by the $*$) where

$$E_1^* = \frac{1}{2m_1} (m_1^2 + m_j^2 - m_2^2) \quad (2.37)$$

$$p_1^* = \sqrt{E_1^* - m_1^2} = -p_2^* \quad (2.38)$$

and take advantage of energy conservation and Lorentz-invariance

$$p_{j\mu} p_1^\mu = p_{j\mu}^* p_1^{\mu*} = E_1^* m_j \quad (2.39)$$

hence, the integral in Eq. (2.34) for just two bodies reduces to

$$E_1 \frac{dN_1}{d^3 p_1} = B \int \frac{d^3 p_j}{E_j} \delta \left(\frac{p_{j\mu} p_1^\mu}{m_j} - E_1^* \right) \left(E_j \frac{dN_j}{d^3 p_j} \right) \quad (2.40)$$

After expanding the delta function argument explicitly we get a condition in terms of the transverse mass and momentum (m_T, p_T) and rapidity (y)⁶

$$\frac{m_{T1} m_{Tj} \cosh(y_1 - y_j) - p_{T1} p_{Tj} \cos(\theta_1 - \theta_j)}{m_j} - E_1^* = 0 \quad (2.41)$$

⁵See appendix C

⁶See appendix A

Rearranging this becomes

$$(e^{y_j-y_1})^2 - 2Ae^{y_j-y_1} + 1 = 0 \quad (2.42)$$

$$A = \frac{m_j E_1^* + p_{T1} p_{Tj} \cos(\theta_1 - \theta_j)}{m_{T1} m_{Tj}} \quad (2.43)$$

Which introduces constraints linking rapidity, transverse mass and relative angle

$$y_j = y_1 + \ln(A \pm \sqrt{A^2 - 1}) \quad A > 1 \quad (2.44)$$

Eq. (2.44) can be used to eliminate rapidity from the integration and to introduce integration constraints on m_T :

$$\frac{m_j E_1^* + p_{T1} p_{Tj} \cos(\theta_1 - \theta_j)}{m_{T1} m_{Tj}} > 1 \quad (2.45)$$

together with $|\cos(\theta_1 - \theta_j)| \leq 1$ leads to

$$m_j E_1^* - p_{T1} p_{Tj} > m_{T1} m_{Tj} \quad (2.46)$$

with the limiting cases

$$m_j E_1^* - p_{T1} \sqrt{m_{Tj}^2 - m_j^2} = m_{T1} m_{Tj} \quad (2.47)$$

Rearranging and squaring, we get

$$p_{T1}^2 (m_{Tj}^2 - m_j^2) = (m_j E_1^* - m_{T1} m_{Tj})^2 \quad (2.48)$$

putting this in the quadratic form and remembering that $m_{T1}^2 - p_{T1}^2 = m_1^2$

$$m_1^2 m_{Tj}^2 - 2m_{Tj} m_{T1} m_j E_1^* + m_j^2 (p_{T1}^2 + E_1^{*2}) = 0 \quad (2.49)$$

Using the quadratic formula, we get two solutions (a factor of 2 cancels out from top and bottom)

$$m_{Tj} = \frac{m_{T1} m_j E_1^* \pm \sqrt{(m_{T1} m_j)^2 - m_1^2 m_j^2 (E_1^{*2} + p_{T1}^2)}}{m_1^2} \quad (2.50)$$

which simplify since

$$\begin{aligned} \sqrt{m_{T1}^2 m_j^2 E_1^{*2} - m_1^2 m_j^2 p_{T1}^2 - m_1^2 m_j^2 E_1^{*2}} &= m_j \sqrt{m_{T1}^2 E_1^{*2} - m_1^2 p_{T1}^2 - m_1^2 E_1^{*2}} \\ &= m_j \sqrt{p_{T1}^2 E_1^{*2} - p_{T1}^2 m_1^2} = m_j p_{T1} p_1^* \end{aligned} \quad (2.51)$$

If one puts this into Eq. (2.50) one gets

$$m_{Tj}^\pm = \frac{m_j}{m_1^2} (m_{T1} E_1^* \pm p_{T1} p_1^*) \quad (2.52)$$

reassuringly, this is always physical since $m_{T1} E_1^* > p_{T1} p_1^*$

In a similar vein, Eq. (2.44) yields the constraints for the relative angle θ_j .

Putting in the form of A (Eq. 2.43) into Eq. (2.44) and manipulating one gets

$$\frac{-m_j E_1^* + m_{T1} m_{Tj}}{p_{T1} p_{Tj}} < \cos(\theta_j - \theta_1) \quad (2.53)$$

$$\theta_1 - \arccos\left(\frac{-m_j E_1^* + m_{T1} m_{Tj}}{p_{T1} p_{Tj}}\right) < \theta_j < \theta_1 + \arccos\left(\frac{-m_j E_1^* + m_{T1} m_{Tj}}{p_{T1} p_{Tj}}\right) \quad (2.54)$$

Putting everything together, we finally have an analytically solvable expression for the decay products distribution in terms of the resonance distribution

$$E_1 \frac{dN_1}{d^3 p_1} = B \int_{m_T^-}^{m_T^+} m_{Tj} dm_{Tj} \int_{\theta^-}^{\theta^+} d\theta_j \int dy_j \delta(y_j = y_1 + \ln(A \pm \sqrt{A^2 - 1})) \left(E_j \frac{dN_j}{d^3 p_j} \right) \quad (2.55)$$

$$A = \frac{m_j E_1^* + p_{T1} p_{Tj} \cos(\theta_1 - \theta_j)}{m_{T1} m_{Tj}} \quad (2.56)$$

$$\theta^\pm = \theta_1 \pm \arccos\left(\frac{-m_j E_1^* + m_{T1} m_{Tj}}{p_{T1} p_{Tj}}\right) \quad (2.57)$$

Integrating over Eq. (2.56) to find N_1/N_j we discover that the normalization has to be

$$B = \frac{b_{j \rightarrow 1}}{4\pi p^*} \quad (2.58)$$

An important simplification arises in the rapidity-invariant limit (Bjorken 1983):

In this case, the integral over the δ function in Eq. (2.55) has no effect, and the different Fourier components of the distributions

$$E_1 \frac{dN_1}{d^3 p_1} = v_{10} + v_{11} \cos(\theta) + v_{12} \cos(2\theta) \dots \quad (2.59)$$

$$E_j \frac{dN_j}{d^3 p_j} = v_{j0} + v_{j1} \cos(\theta) + v_{j2} \cos(2\theta) \dots \quad (2.60)$$

do not mix (ie v_{J_0} has no effect on $v_{1m \neq i}$) (Baran et al. 2003)

If the original distribution function is azimuthally invariant (no θ dependence), Eq. (2.55) simplifies to (Sollfrank et al. 1990)

$$\frac{dN}{dm_{T1}^2 dy_1} = \frac{b}{4\pi p_1^*} \int_{y_-}^{y_+} dy_j \int_{m_{T-}}^{m_{T+}} dm_{Tj}^2 J \frac{d^2 N_j}{dm_{Tj}^2 dy_j}, \quad (2.61)$$

$$J = \frac{m_j}{\sqrt{p_{Tj}^2 p_{T1}^2 - (m_R E_1^* - m_{Tj} m_{T1} \cosh(y_j - y_1)^2)}}, \quad (2.62)$$

$$y_{\pm} = y_1 \pm \sinh^{-1} \left(\frac{p_1^*}{m_{T1}} \right) \quad (2.63)$$

$$m_T^{\pm} = m_j \frac{E_1^* m_{T1} \cosh(y_j - y_1) \pm p_{T1} \sqrt{p_1^{*2} - m_{T1}^2 \sinh^2(y_j - y_1)}}{m_{T1}^2 \sinh^2(y_j - y_1) + m_1^2} \quad (2.64)$$

Decays of three bodies and more

The strategy to pursue if there are more than 3 bodies in the decay is to change variables from p_1, p_2, \dots, p_n to $p_1, p_2, \dots, p_{n-1}, s_{2..n}, p_{2..n}$ where

$$s_{2..n} = \left(\sum_{i=2}^n E_i \right)^2 - \left(\sum_{i=2}^n p_i \right)^2 \quad (2.65)$$

is the invariant mass of “all the other” decay products (Byckling and Kajantie 1969) and $p_{2..n}$ is their combined momentum. The invariant phase-space in Eq. (2.34)

becomes, applying the δ function in Eq. (2.40)

$$E_1 \frac{dn_1}{d^3 p_1} = B \int_{s_-}^{s_+} ds_{2..n} \left| \frac{\partial(p_1, p_2, \dots, p_{n-1}, s_{2..n}, p_{2..n})}{\partial(p_1, \dots, p_n)} \right| \quad (2.66)$$

$$\begin{aligned} & \int \frac{d^3 p_j}{E_j} \delta \left(\frac{p_{j\mu} p_1^\mu}{m_j} - E_1^* \right) \int T_{n-1} \left(E_j \frac{d^3 N_j}{d^3 p_j} \right) \\ & E_{2..n}^2 = \sqrt{p_{2..n}^2 + s_{2..n}} \\ & E_1^2 = \sqrt{p_{2..n}^2 + m_1} \end{aligned} \quad (2.67)$$

here T_n is given as in Eq. (2.34), the Jacobian is

$$\left| \frac{\partial(p_1, p_2, \dots, p_{n-1}, s_{2..n}, p_{2..n})}{\partial(p_1, \dots, p_n)} \right| = \frac{\sqrt{m_j - (s_{2..n} + m_1)^2} \sqrt{m_j - (s_{2..n} - m_1)^2}}{m_j} \quad (2.68)$$

and the limits of integration are given by energy conservation

$$s_- = \left(\sum_{i=2}^n \right)^2 \quad s_+ = (m_j - m_1)^2 \quad (2.69)$$

Thus, the n-body decay can be expressed as a convolution of a 2-body and an n-1 body decay, and further convoluted to n 2-body decays.

Unsurprisingly, the decay products of the cascades such as

$$\eta' \rightarrow \eta \pi \rightarrow \pi \pi \pi \pi \quad (2.70)$$

(Fig. 2.1 left) will have a very similar distribution: $E_j \frac{dN_j}{d^3 p_j}$ of the intermediate state (η in Eq. (2.70)) will be fed back into a formula such as Eq. (2.34), and the only difference from Eq. (2.66) is that the intermediate mass is a constant

$$\left| \frac{\partial(p_1, p_2, \dots, p_{n-1}, s_{2..n}, p_{2..n})}{\partial(p_1, \dots, p_n)} \right| \rightarrow \delta(s - m_{intermediate}) \quad (2.71)$$

or a Lorentzian if $\Gamma \neq 0$.

If the resonance distribution is azimuthally invariant Eq. (2.66) for the 3-body case simplifies to (Sollfrank et al. 1990)

$$\frac{dN_1}{d^3 p_1} = B \frac{\sqrt{m_j - (s_{2..n} + m_1)^2} \sqrt{m_j - (s_{2..n} - m_1)^2}}{m_j} \left(E_{s \rightarrow 23} \frac{dN_{s \rightarrow 23}}{d^3 p_{s \rightarrow 23}} \right) \quad (2.72)$$

$$B = \frac{m_j b_{j \rightarrow 123}}{2\pi Q[(m_j + m_1)^2, (m_j - m_1)^2, (m_2 - m_3)^2, (m_2 + m_3)^2]} \quad (2.73)$$

$$Q[a, b, c, d] = \int_c^b \frac{dx}{x} \sqrt{(a-x)(b-x)(x-c)(x-d)} \quad (2.74)$$

where $\left(E_{s \rightarrow 23} \frac{dN_{s \rightarrow 23}}{d^3 p_{s \rightarrow 23}}\right)$ is given by Eq. (2.61).

From the above discussion, it is clear that in general an n-body decay will involve $2n + 1$ numerical integrals. Cascades of n steps with a n_i decay at each step will require a total of $\sum_{i=1}^n n_i$ integrals to find the final decay products from the resonance distribution.

It is clear that in general Monte-Carlo integration becomes the only way to evolve decays beyond a simple topology. Algorithms such as MAMBO (Kleiss and Stirling 1992) can generate points with a uniform density in n-body phase space. In the subsequent chapters we will use MAMBO to perform integrals within the Monte-Carlo program, and multi-dimensional Gaussian integration (Various 1999) in our fits. The latter, therefore, can only accommodate a restricted number of resonances where the decay topology is not too complicated.

2.5 What kind of statistical hadronization?

The formation of QGP should be accompanied by statistical hadronization at some point: This, in a sense, true by definition, since phase transitions characterize equilibrated systems. However, by itself, statistical hadronization is not a proof of quark gluon plasma formation, since any system will thermalize after enough time as discussed in section 2.2.

While, as discussed in sections 1.5.5 and 1.5.6, the equilibration time of a

system of quarks should be larger by an order of magnitude than that of a system of hadrons, hence evidence of early thermalization can be construed as a QGP signature, some thought should be put into whether statistical hadronization of a QGP can be distinguished from freeze-out of an equilibrated hadronic system.

An obvious signal to look for is whether the hadron formation temperature approaches the temperature predicted by lattice for deconfinement. However, as explained in chapter 1, lattice results have still to converge on a definite value for the phase transition temperature. In addition, if the phase transition is sharp enough, phenomena such as super-cooling can lower the temperature at which hadrons are emitted.

A phase transition from a QGP to a hadron gas should also considerably increase the system's mean free path. Due to this, the Cooper-Frye prescription should be particularly appropriate. While this has certain consequences, which the next two chapters will explore, it is also hardly a definite distinction, due to the Cooper-Frye formula's flexibility in the choice of $d^3\Sigma$ and u^μ (see chapter 4)

Finally, it should be mentioned that the phase space available to QGP is very different to that available to a HG: The lightest degree of freedom in a (perturbative) QGP is massless, with a degeneracy of 16. The lightest degree of freedom in a Hadron Gas, on the other hand, has a mass comparable to the hadronization temperature and a degeneracy of 3. This suggests that, if the phase transition is sharp, statistical emission of hadrons from a QGP will not be based on chemical equilibration at all, but rather on production of hadrons from quarks with thermal weights. Section 2.4.3 describes a statistical hadronization model based on these assumptions.

These considerations suggest that “statistical hadronization” actually encompasses a variety of models, different in both physical interpretation and observational consequences. This is indeed the case. The following two sub-sections describe the two “camps” into which statistical models can be categorized.

2.5.1 Long freeze-out

The most naive model for freeze-out assumes particle formation at the deconfinement temperature, a long-interacting hadron gas phase, and thermal freeze-out at ~ 100 MeV. Superficially, such a picture has experimental support. It is possible to fit hadrons produced at RHIC (Braun-Munzinger et al. 2001) and SPS (Braun-Munzinger et al. 1999) (Fig. (2.2)) using a model based on chemical equilibration $\lambda_q = \lambda_{\bar{q}}^{-1}$ and Eqns. (2.24) and (2.30), and get a temperature of the order of ~ 170 MeV. The chemical potential decreases with higher energy, as expected (see Chapter 1). In this model hadrons will continue interacting, so particle spectra will

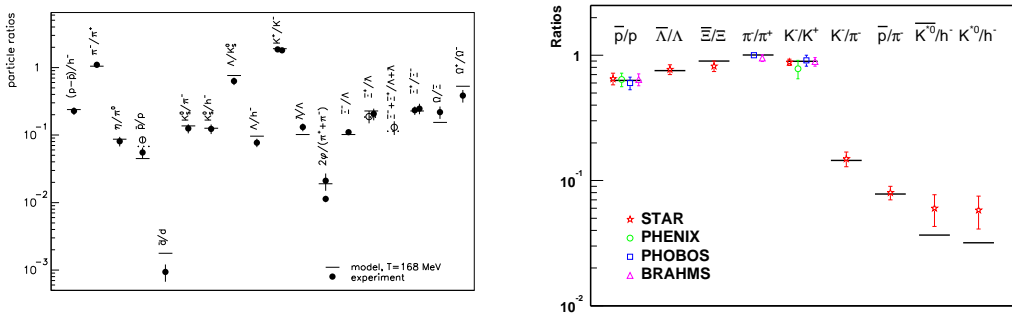


Figure 2.2: Equilibration fits for SPS (left) and RHIC (right) energies. The $\chi^2/\text{DoF} = 38/16$ at the SPS and $5.7/7$ at RHIC.

have to be modeled with a different set of thermodynamic parameters. Experiments have done these fits, neglecting resonance abundances, and have found a spectra

freeze-out temperature of 100MeV for all particles except Ξ s and Ω , consistent with a staged thermal freeze-out (Adams et al. 2003b),(Afanasiev et al. 2003) where particles with fewer interactions with pions (particularly the Ω , as there is no $\Omega\pi$ resonance) freeze-out earlier.

Σ^μ in the Cooper-Frye formula will then not be a good physical description of particle emission, since particles will not be emitted from a definite point in spacetime, but will emerge from a “freeze-out hyper-volume” (a continuous limit of fewer and fewer interactions). However, the Cooper-Frye description can still be used as a prescription to switch from a continuous medium to a gas of hadrons (not necessarily at a phase transition, but simply the space-time region the mean free path becomes “large”) (Teaney et al. 2001)

This picture, however, has problems both at a fundamental level and in terms of experimental agreement. The fits in Fig. 2.2 actually have a very small statistical significance. The experimental fits performed in (Adams et al. 2003b),(Afanasiev et al. 2003) are demonstrably meaningless, since they do not include resonances which have already been experimentally detected (see chapter 5). On a fundamental level, It is hard to see how entropy gets conserved in a QGP-HG chemically equilibrated phase transition unless the transition is slow enough to permit the system’s volume to increase significantly (something not corroborated by the lattice).

It is also difficult to see why particle spectra should be described by a hydrodynamical model at all, given that an interacting hadron gas at $T = 120 - 170$ should include many out-of-equilibrium inelastic interactions. In particular, the possibility for baryon-antibaryon annihilation at any cross-section makes it puzzling

that the m_T slopes for particle and anti-particle are virtually identical, as shown in chapter one. (Fig. 1.16, (Bruno et al. 2003)). This feature is predicted by hydrodynamic models with a few simple reactions (quark-level kinetics, $gg \leftrightarrow q\bar{q}$), but certainly not in an interacting hadrons gas picture with many particle-specific channels ($\Lambda + \bar{\Lambda} \leftrightarrow$ pions, $p + \bar{\Lambda} \leftrightarrow$ Pions and Kaons, ...).

Another failure of the low temperature scenario is Hanbury-Brown-Twiss interferometry (HBT) applied to π and K. This technique, which relies on bosonic two-particle correlations assuming no quantum mechanics before emission, has been used to estimate the spacetime shape of the system when interactions stop (Wiedemann and Heinz 1999). It has been found that “naive” hydrodynamics with early freeze-out fails to explain the observed correlations (Heinz and Kolb 2002) unless fast emission and a small freeze-out radius (which contradict the model) are introduced by hand.

While the effectiveness of HBT as a description has been questioned in light of its assumptions (For instance, how to properly take short lived resonances (Bolz et al. 1993) and final state interactions (Gastineau and Aichelin 2000; Wong 2004) into account?), the need of hydrodynamic models to introduce fast freeze-out Ad Hoc to even qualitatively explain the data, together with its other failings, is a strong motivation to look for a scenario where fast freeze-out is part of the model, and particles stop interacting soon after formation.

2.5.2 Explosive freeze-out

One framework which would explain the rapid freeze-out and lack of post-hadronization interactions is explosive hadronization of a super-cooled plasma

(Csorgo and Csernai 1994),(Rafelski and Letessier 2000). If the QGP-HG phase transition is first order, at a certain critical temperature/density the two phases will coexist. We can estimate this critical density through the Bag model, described in the previous chapter (section 1.4.1)

$$T_{QGP}^{\mu\nu} = T_{HG}^{\mu\nu} + Bg^{\mu\nu} \quad (2.75)$$

where B is the vacuum pressure/bag constant. If the Quark gluon plasma exhibits strong collective expansion, ie

$$T_{QGP}^{\mu\nu} = Pg^{\mu\nu} + (P + \epsilon)u^\mu u^\nu \quad (2.76)$$

it will expand past the phase of coexistence. The QGP will then experience negative pressure, from the outside vacuum. What happens in this situation is described in hydrodynamics as “viscous fingering” (Sonin 1991): A mechanical instability develops on the surface where the two phases meet, and the lower pressure QGP “fingers” into the higher-pressure vacuum. Hadron emission will then occur through “bubbling” at that surface, as the mechanical instability tears the fireball apart (Fig. 2.3). The hadronization freeze-out surface will then acquire a physical meaning

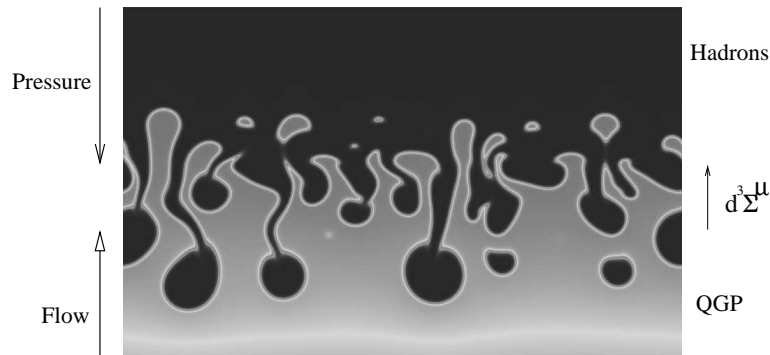


Figure 2.3: How expansion plus vacuum pressure leads to viscous fingering .

as the surface where the two vacua come into contact and viscous fingers develop.

Indeed, the whole freeze-out dynamics is modeled through the choice of Σ^μ and the Matching conditions (Csernai et al. 2003)

$$d^3\Sigma_\mu(T_{QGP}^{\mu\nu} - T_{HG}^{\mu\nu}) = 0 \quad (2.77)$$

$$d^3\Sigma_\mu(n_{QGP}^\mu - n_{HG}^\mu) = 0 \quad (2.78)$$

$$d^3\Sigma_\mu(S_{HG}^\mu - S_{QGP}^\mu) \geq 0 \quad (2.79)$$

Where n^μ refers to any conserved quantum number current (flavor, strangeness, charge etc.). It becomes clear that the last equation is the most problematic. While the first two equations can generally be satisfied through a readjustment of the thermodynamic parameters at freeze-out (Keranen et al. 2003), the entropy of the hadron gas will in general tend to always be much lower than that of the QGP due to the fact that HG degrees of freedom are much more massive. In a slow freeze-out scenario entropy will be generated through flow. If freeze-out is sudden, however, entropy conservation across the freeze-out surface in equilibrium is only possible by either choosing carefully the freeze-out parameters or post-hadronization reheating (release of latent heat) (Keranen et al. 2003).

A more general freeze-out scenario is provided by dropping the assumption that hadronization happens under flavor chemical equilibrium. Chemical equilibrium requires that particle and antiparticle fugacities are inverse of each other

$$\lambda_q = \lambda_{\bar{q}}^{-1} \quad (2.80)$$

which, by the law of mass action, corresponds to the equilibration of creation and annihilation processes

$$q\bar{q} \rightarrow gg \Leftrightarrow gg \rightarrow q\bar{q} \quad (2.81)$$

According to the Boltzmann equation Eq. (2.2) this condition will be reached for

all quark flavors after infinite time. To model the approach of this condition, one defines the phase space occupancy γ_q so that

$$\lambda_q \rightarrow \lambda_q \gamma_q \quad \gamma_q = \gamma_{\bar{q}} \quad (2.82)$$

Equilibrium will then be reached when $\gamma_q = 1$. Several authors have allowed the possibility that strangeness is not yet in chemical equilibration when freeze-out happens (Becattini et al. 2003), but it is still generally assumed that light quarks are equilibrated. It is not immediately clear, however, why any quantum number should be equilibrated at all in a phase transition during dynamic non-equilibrium.

It turns out that if one allows light quark phase space to be overpopulated, i.e. grow above equilibrium ($\gamma_q > 1$), the entropy of the hadron gas starts growing rapidly with γ_q (Letessier et al. 2000) (Fig. 2.4). This region is phase space is kinetically not reachable through a hadron gas evolution such as that described in Eq. (2.2). However, if the particles are emitted from a rapidly non-perturbatively hadronizing $q\bar{q}$ rich QGP, over-saturation might occur. This is the only way found as yet to contain the entropy created during the QGP stage without reheating or expansion (which requires slow hadronization) The value of γ_q is bounded above by the Bose-Einstein condensation condition for pions

$$\frac{1}{\gamma_q^{-2} e^{m_\pi/T} - 1} < \infty, \quad \gamma_q < e^{m_\pi/2T} \quad (2.83)$$

above which a Bose-Einstein Condensate (BEC) of pions forms, which consumes energy while carrying no entropy. The BEC constraint works well with the super-cooling hypothesis, since γ_q has more freedom to rise to the point at which $S_{QGP} < S_{HG}$ only as the critical temperature becomes fairly small $\sim 140\text{MeV}$.

This picture is phenomenologically in accord with the Gribov hadronization

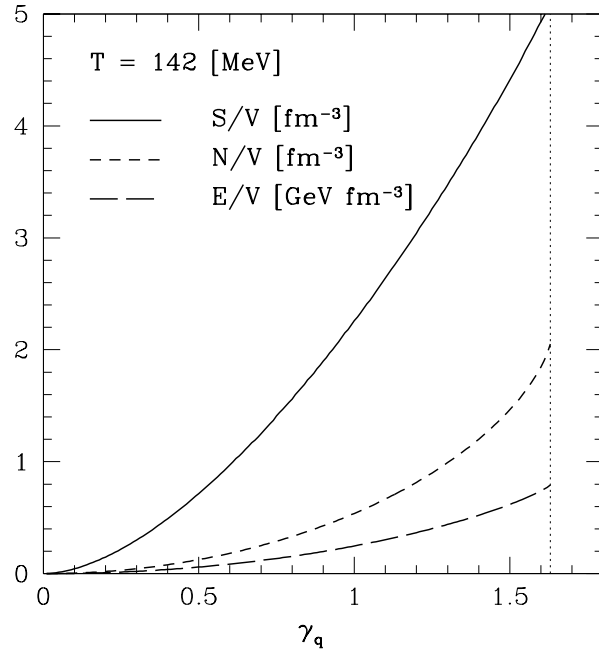


Figure 2.4: Entropy, Energy and number density as $\gamma_q > 1$ increases .

scenario described in section 1.3.1. As energy density reaches a critical value, the color potential between quarks and gluons grows up to the point where it is energetically convenient to fragment gluons into $q\bar{q}$ pairs to maintain large-scale color neutrality. The $q\bar{q}$ phase space is then overpopulated as the gluons are depleted by $g \rightarrow q\bar{q}$ reactions. Tables 2.1 and 2.2 (Rafelski and Letessier 2003a) and (Letessier and Rafelski 2000) make it clear that fits where γ_q is a variable parameter consistently prefer values of γ_q just below the BEC limit. In this minimum, $\mu_s = T \ln(\lambda_s)$ goes to a value very close to 0, in accordance to a scenario where strangeness is

Table 2.1: The chemical freeze-out statistical parameters found for nonequilibrium (left) and semi equilibrium (right) fits to SPS results. We show $\sqrt{s_{NN}}$, the temperature T , light quark fugacity λ_q , strange quark fugacity λ_s , the quark occupancy parameters γ_q and γ_s/γ_q . Bottom line presents the statistical significance of the fit. The star (*) indicates for λ_s that it is a value resulting from strangeness conservation constraint. For γ_q that there is an upper limit to which the value converged, $\gamma_q^2 < e^{m\pi/T}$ (on left), or that the value of $\gamma_q = 1$ is set (on right).

$\sqrt{s_{NN}}$ [GeV]	17.2	12.3	8.75	17.2	12.3	8.75
T [MeV]	135 ± 3	135 ± 3	133 ± 2	157 ± 4	156 ± 4	154 ± 3
λ_q	1.69(5)	1.98(6)	2.56(6)	1.74(5)	2.03(7)	2.69(8)
λ_s	1.23*	1.27*	1.31*	1.20*	1.24*	1.24*
γ_q	1.68*	1.68*	1.69*	1*	1*	1*
γ_s/γ_q	0.91(6)	0.83(4)	0.85(6)	0.66(4)	0.60(4)	0.67(5)
χ^2/dof	11.4/6	4.3/2	2.3/4	23/7	8.9/3	4.0/5

produced through annihilation and gluon fusion reactions. These fit's statistical significance is markedly better than fits based on the equilibrium hypothesis.

2.6 How to falsify freeze-out models

Sudden non-equilibrium freeze-out has therefore passed the elementary comparison with experimental data. It can fit observed hadron yields to an acceptable statistical significance. It also seems that super-cooling can explain the small volume and fast emission times inferred by HBT observations (Csernai et al. 2003), though this has yet to undergo a quantitative corroboration.

However, the sudden freeze-out picture allows for much more stringent falsifiability tests to be made, since it demands that all soft variables be described by the same set of statistical mechanics parameters. The rest of this thesis performs

Table 2.2: freeze-out statistical parameters found for non-equilibrium (left) and $\gamma_q = 1, \gamma_s$ fitted (right) fits to RHIC results. We show $\sqrt{s_{NN}}$, the temperature T , baryochemical potential μ_b , strange quark chemical potential μ_s , strangeness chemical potential μ_S , the quark occupancy parameters γ_q and γ_s/γ_q , and in the bottom line the statistical significance of the fit. The star (*) indicates that there is an upper limit on the value of $\gamma_q^2 < e^{m_\pi/T}$ (on left), and/or that the value is set (on right).

$\sqrt{s_{NN}}$ [GeV]	200	130	200	130
T [MeV]	143 ± 7	144 ± 3	160 ± 8	160 ± 4
μ_b [MeV]	21.5 ± 31	29.2 ± 4.5	24.5 ± 3	31.4 ± 4.5
μ_s [MeV]	2.5 ± 0.2	3.1 ± 0.2	2.9 ± 0.2	3.6 ± 0.2
μ_S [MeV]	4.7 ± 0.4	6.6 ± 0.4	5.3 ± 0.4	6.9 ± 0.4
γ_q	$1.6 \pm 0.3^*$	$1.6 \pm 0.2^*$	1^*	1^*
γ_s/γ_q	1.2 ± 0.15	1.3 ± 0.1	1.0 ± 0.1	1.13 ± 0.06
χ^2/dof	$2.9/6$	$15.8/24$	$4.5/7$	$32.2/25$
P_{true}	$90\%+$	$95\%+$	65%	15%

some of these falsifiability tests, which can be broadly grouped in three categories.

Particle spectra In the sudden hadronization picture, particles form from a transversely expanding system and undergo little or no re-interaction after formation. Therefore, the same temperature which describes hadron abundances should, with the addition of transverse flow, also be able to describe the shape of hadron spectra. Moreover, because of the absence of the hadron gas phase, the number of hadrons in each particle species is unchanged since formation, except for the decay of short-lived resonances.

Therefore, spectra should be normalized through hadronic chemical potentials, and the resonance admixture into the spectra should be prominently present. The non-equilibrium parameters γ_q fitted in table 2.2 should also be necessary to describe particle spectra. These predictions are tested in detail within the

next two chapters.

Short-lived resonances Short lived resonances (strong excited states) provide a direct test of post-hadronization interactions, since their final yield will be affected by them. The sudden freeze-out model demands, therefore, that their abundance be determined by the same temperature and chemical potentials that determine long-lived particles. Any deviation from this can be attributed to post-hadronization dynamics. This is explored quantitatively in chapter 5.

Exotica (Pentaquarks etc.) Pentaquarks should be strongly enhanced in a non-equilibrium model: Their mass seems to be similar to that of other short-lived resonances (Diakonov et al. 1997), but, of course, they have a different number of quarks (5 in the pentaquark case). Hence, in non-equilibrium models they should be enhanced with respect to similar baryons by a factor of $\sim \gamma_q^2$. This is a large difference for $\gamma_q \sim 1.5$. This is also explored in chapter 5.

Freeze-out dynamics If hadronization happens through a vacuum instability at the QGP-HG contact surface, the freeze-out hypersurface $d^3\Sigma^\mu$ acquires a physical significance connected to the confining phase transition. Therefore

- Experimental data should strongly prefer a particular choice of $d^3\Sigma^\mu$
- The preferred $d^3\Sigma^\mu$ should be localized on a surface moving with time across the fireball.

Chapter 4 will explore whether the $d^3\Sigma^\mu$ choice can be made through an analysis of particle spectra alone. Chapters 5 and 6 will provide ways to constrain $d^3\Sigma^\mu$ further.

CHAPTER 3

Particle spectra at SPS: a spherical ansatz

3.1 Sudden freeze-out spectra

The WA97 and NA57 experiments have, for the first time, measured the normalized spectra of a wide range of strange hadrons, ranging in mass from the K_S to the Ω (Bruno et al. 2003). The relative yield of these particles has been one of the main pieces of evidence pointing to the formation of quark gluon plasma at SPS energies (Heinz and Jacob 2000). Correspondingly the spectra's variety can provide a very stringent constraint on the system's freeze-out conditions.

In particular, when sudden QGP breakup occurs, the spectra of hadrons are not formed at a range of stages in fireball evolution, but arise rather suddenly. Most importantly, particles of very different properties are produced by the same mechanism and thus are expected to have similar m_\perp -spectra as is indeed observed (Bruno et al. 2003). The reported symmetry of the strange baryon and antibaryon spectra is strongly suggesting that the same reaction mechanism produces Λ and $\bar{\Lambda}$ and Ξ and $\bar{\Xi}$. This is a surprising, but rather clean experimental fact, which we will interpret quantitatively in this paper.

When the momentum distributions of final state particles stop evolving during the fireball evolution, we speak of thermal freeze-out. Because a spectrum of

strange hadrons includes directly produced, and heavy resonance decay products, one can determine the freeze-out temperature and dynamical velocities of fireball evolution solely from the study of precisely known shape of the particle spectra. We demonstrate this in some detail in section 3.5. The physical mechanism is that the freeze-out temperature determines the relative contribution of each decaying resonance while the shape of each decay contribution differs from the thermal shape, see section 3.3.

We note that we make in our analysis the tacit assumption that practically all decay products of resonances are thermally not re-equilibrated, which is equivalent to the assumption of sudden freeze out. This is consistent with our finding that the m_\perp strange baryon and antibaryon distributions of $\Lambda, \bar{\Lambda}, \Xi, \bar{\Xi}$ froze out near to the condition at which the chemical particle yields were established.

One of the key objectives of this work is to present a comparison between thermal and chemical freeze-out analysis results for temperature, (explosion) collective velocity and other chemical and dynamical parameters. It is important to realize that particle spectra and yields are sensitive to magnitude of collective matter flow, in which produced particles are born, for somewhat different reasons: 1) in thermal analysis the collective flow combines with thermal freeze-out temperature to fix the shape of each particle spectrum, and temperature is also controlling the relative yield of contributing resonances – see previous paragraph for a here relevant tacit assumption – thus both T and v are fixed by the shape of m_\perp data; 2) in chemical analysis the particle yields required are obtained integrating spectral yields, with experimental acceptance in p_\perp, y implemented. Since many particles have a too small particle momentum to be usually observed, the acceptance-cut

yields used in chemical analysis depend quite sensitively on parameters which deform the soft part of the spectra without changing the number of produced particles, such as is the flow velocity. For this reason precise particle spectra and yields are allowing to draw conclusions about the proximity of thermal and chemical freeze-out conditions.

3.2 Spherically symmetric freeze-out

Collisions at the SPS are characterized by a high degree of stopping power: Most of the primordial particles lose their longitudinal momentum in the initial collision, and the mid-rapidity region has a high particle/antiparticle imbalance (Appelshauser et al. 1999) and hence baryochemical potential. Hence, it is reasonable to assume that the system will not have a longitudinal rapidity structure at freeze-out. One such emission surface which has the advantage of analytical simplicity is spherically symmetric freeze-out. Such an ansatz is also favoured by hydrodynamic evolution, since the hydrostatic force per unit volume is minimized.

We proceed to construct a spherically symmetric freeze-out hypersurface, in which the freeze-out time depends on the radius alone

$$\Sigma^\mu = \begin{pmatrix} t_f(r) \\ r \sin(\theta) \cos(\phi) \\ r \sin(\theta) \sin(\phi) \\ r \cos(\theta) \end{pmatrix} \quad (3.1)$$

Parameterizing this surface in terms of r, θ, ϕ we get, according to Eq. (2.15), an

emission element of this form:

$$d^3\Sigma^\mu = r dr d\theta \begin{pmatrix} 1 \\ \frac{\partial t_f}{\partial r} \sin(\theta) \cos(\phi) \\ \frac{\partial t_f}{\partial r} \sin(\theta) \sin(\phi) \\ \frac{\partial t_f}{\partial r} \cos(\theta) \end{pmatrix} \quad (3.2)$$

combining this emission shape with a spherically symmetric flow we get an explicit form from the Cooper-Frye formula (where θ is the configuration space emission coordinate and ϕ the particle momentum coordinate).

$$E \frac{dN}{d^3p} = N \prod \lambda_i \gamma_i \int r^2 dr \int \sin(\theta) d\theta \left(E - p_T \frac{\partial t_f}{\partial r} \cos(\theta - \phi) \right) e^{-\frac{\gamma}{T}(E - v p_T \cos(\theta - \phi))} \quad (3.3)$$

Using modified Bessel functions, the integral over θ can be done analytically

$$E \frac{dN}{d^3p} = N \int r^2 dr \sqrt{\frac{T}{\gamma v p_T}} \left(E I_{1/2} \left(\frac{\gamma v p_T}{T} \right) - p_T \frac{\partial t_f}{\partial r} I_{1/2} \left(\frac{\gamma v p_T}{T} \right) \right) \quad (3.4)$$

and the Normalization N includes the degeneracy and chemical potentials

$$N = g_i \prod \lambda_i \gamma_i \quad (3.5)$$

This approach can be generalized to B-E and F-D statistics, relevant for π , as, for realistic chemical potentials, these distributions can be represented as a converging series of Boltzmann-like therm

$$\lambda e^{-\frac{p_\mu u^\mu}{T}} \rightarrow \sum_{n=0}^{\infty} (\pm 1)_{BE/FD}^n \lambda^{n+1} e^{-(n+1)\frac{p_\mu u^\mu}{T}} \quad (3.6)$$

For a real hydrodynamical system the integration over r will not be trivial, since flow will be a non-trivial, equation of state dependent function of r . For our fit, we shall average the system using one flow.

$$E \frac{dN}{d^3p} = N V E \frac{dN}{d^3p} (\langle v \rangle, \langle \gamma \rangle) \quad (3.7)$$

The consequences of such averaging will be explored in the next chapter in detail

3.3 Thermal freeze-out analysis of SPS data

In recent months experiment WA97 determined the absolute normalization of the published m_{\perp} distribution (Bruno et al. 2003), and we took the opportunity to perform the spectral shape analysis and will compare our results to those obtained in chemical yield analysis (Letessier and Rafelski 2000) in order to check if the thermal and chemical freeze-out conditions are the same. Our analysis continues and this report gives its current status.

We report here a simultaneous analysis of absolute yield and shape of WA97 results of six m_{\perp} -spectra of Λ , $\bar{\Lambda}$, Ξ , $\bar{\Xi}$, $\Omega + \bar{\Omega}$, $K_s = (K^0 + \bar{K}^0)/2$ in four centrality bins. If thermal and chemical freeze-outs are identical, our present results must be consistent with earlier chemical analysis of hadron yields. Since the experimental data we here study is dominated by the shape of m_{\perp} -spectra and not by relative particle yields, our analysis is de facto comparing thermal and chemical freeze-outs.

We have found, as is generally believed and expected, that all hadron m_{\perp} -spectra are strongly influenced by resonance decays. Thus we apply standard procedure to allow for this effect (Sollfrank et al. 1990) and described in the previous chapter.

Since particle spectra we consider have a good relative normalization, only one parameter is required for each centrality in order to describe the absolute normalization of all six hadron spectra. This is for two reasons important:

- a) we can check if the volume from which strange hadrons are emitted grows with centrality of the collision as we expect;
- b) we can determine which region in m_{\perp} produces the excess of Ω noted in the

chemical fit (Letessier and Rafelski 2000) is coming from.

However, since the normalization V_{QGP} common for all particles at given centrality comprises additional experimental acceptance normalization, we have not determined the value of the fireball emission volume at each centrality. Hence we will be presenting the volume parameter as function of centrality in arbitrary units.

The best thermal and chemical parameters are found by minimizing the total relative error χ^2 as defined in Appendix B, where the data points are given by the WA97 (Bruno et al. 2003) spectra for K^0 , Λ , $\bar{\Lambda}$, Ξ , $\bar{\Xi}$, $\Omega + \bar{\Omega}$. We have checked the validity of the statistical analysis by the usual method, i.e. omission of some data in the fit.

Only in case of Kaons we find any impact of such a procedure. Noting that the statistical error of kaon spectra is the smallest, we have established how a systematic error which could be for Kaons greater than statistical error would influence our result. For this purpose we assign to K^0 experimental results in most of our analysis an ‘error’ which we arbitrarily have chosen to be 5 times greater than the statistical error. In this way the weight of the kaon spectra in the analysis is greatly reduced. In the first result figure below (Fig. 3.1) we present both results, standard K^0 error and enlarged error. We see that while in individual result some change can occur, overall the physical result of both analysis are consistent. Thus we can trust in the combined study of hyperon and kaon data. This conclusion is reaffirmed in section 3.5, where we will see that the minimization of χ^2 involve more or less pronounced minima, depending on the error size of the kaon spectra, see Fig. 3.12. In most calculations we present in this paper we will be using, unless otherwise said, hyperon results combined with the Kaon data with 5 times enlarged

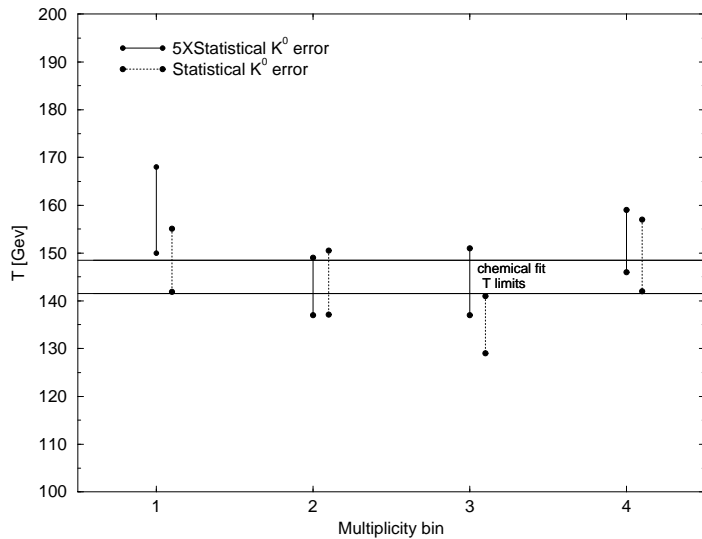


Figure 3.1: (color on-line) Thermal freeze-out temperature T for different centrality bins compared to chemical freeze-out analysis shown by horizontal solid lines. Original statistical error is used in the dotted results, five times statistical error for kaon data is used in solid vertical lines.

statistical error. We believe that in this way we will err on the conservative side in our physical conclusions.

3.4 Overview of the results

We show here a slate of results obtained within the approach outlined above. First we address the parameters determining the shape of the m_{\perp} distributions, that is $T, v, \frac{\partial t_f}{\partial r}$.

As function of the centrality bin we show in Fig. 3.1 the freeze-out temperature T of the m_{\perp} spectra. The horizontal lines delineate range of result of the most recent chemical freeze-out analysis, see Ref. (Letessier and Rafelski 2000). It is reassuring that we find a result consistent with the purely chemical analysis of data that included non-strange hadrons (Letessier and Rafelski 2000). There is

no indication of a significant or systematic change of T with centrality. This is consistent with the belief that the formation of the new state of matter at CERN is occurring in all centrality bins explored by the experiment WA97. Only most peripheral interactions produce a change in the pattern of strange hadron production (Ambrosini et al. 1999). The (unweighted) average of all results shown in Fig. 3.1 produces a freeze-out temperature at the upper boundary of the the pure chemical freeze-out analysis result, $T \simeq 145$ MeV. It should be noted that in chemical analysis $\frac{\partial t_f}{\partial r} = v$ (Letessier and Rafelski 2000), which may be the cause of this slight difference between current analysis average and the earlier purely chemical analysis result.

The magnitudes of the collective expansion velocity v and the break-up (hadronization) speed parameter $\frac{\partial t_f}{\partial r}$ are presented in Fig. 3.2. For v (lower part of the figure) we again see consistency with earlier chemical freeze-out analysis results, and there is no confirmed systematic trend in the behavior of this parameter as function of centrality.

Though within the experimental error, one could argue inspecting Fig. 3.2 that there is systematic increase in transverse flow velocity v with centrality and thus size of the system. This is expected, since the more central events comprise greater volume of matter, which allows more time for development of the flow. Interestingly, it is in v and not T that we find the slight change of spectral slopes noted in the presentation of the experimental data (Bruno et al. 2003).

The value of the break-up (hadronization) speed parameter $\frac{\partial t_f}{\partial r} [= 1/(\partial r_f / \partial t_f)]$ shown in the top portion of Fig. 3.2 is near to velocity of light which is highly consistent with the picture of a sudden breakup of the fireball. This

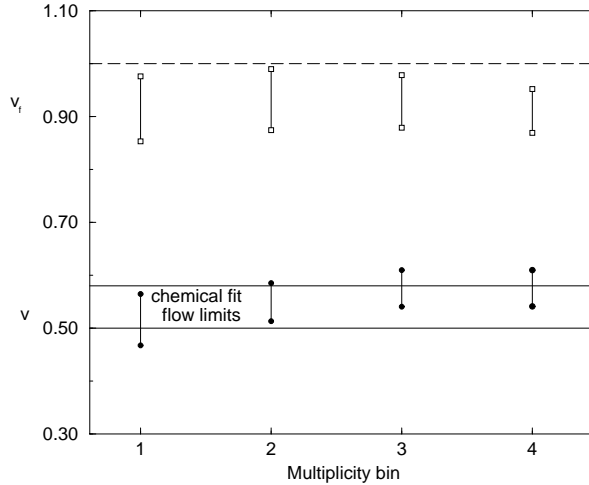


Figure 3.2: (color on-line) Thermal freeze-out flow velocity v (top) and break up (hadronization) velocity $\frac{\partial t_f}{\partial r}$ for different centrality bins. Upper limit $\frac{\partial t_f}{\partial r} = 1$ (dashed line) and chemical freeze-out analysis limits for v (solid lines) are also shown.

hadronization surface velocity $\frac{\partial t_f}{\partial r}$ was in the earlier chemical fit set to be equal to v , as there was not enough sensitivity in purely chemical fit to determine the value of $\frac{\partial t_f}{\partial r}$.

Unlike the temperature and two velocities, the overall normalization of hadron yields, V^h must be, and is strongly centrality dependent, as is seen in Fig. 3.3. This confirms in quantitative way the believe that the entire available fireball volume is available for hadron production. The strong increase in the volume by factor 6 is qualitatively consistent with a geometric interpretation of the collision centrality effect. Not shown is the error propagating from the experimental data which is strongly correlated to the chemical parameters discussed next. This systematic uncertainty is another reason we do not attempt an absolute unit volume normalization.

The 4 chemical parameters $\lambda_q, \lambda_s, \gamma_q, \gamma_s/\gamma_q$ are shown in the following Figures 3.4,3.5. These parameters determine along with V^h the final particle yield. Since we have 5 parameters determining normalization of 6 strange hadron spectra, and as discussed we reduce the statistical weight of Kaons, there is obviously a lot of correlation between these 4 quantities, and thus the error bar which reflects this correlation, is significant.

The chemical fugacities λ_q and λ_s shown in Fig. 3.4 do not exhibit a systematic centrality dependence. This is consistent with the result we found for T in that the freeze-out properties of the fireball are seen to be for the temperature and chemical potential values independent of the size of the fireball. Comparing to the earlier chemical freeze-out result in Fig. 3.4 one may argue that there is a systematic downward deviation in λ_q . However, this could be caused by the fact that the chemical freeze-out analysis allowed for isospin-asymmetric $\Xi^-(dss)$ yield (Letessier and Rafelski 2000), while our present analysis is not yet distinguishing light quarks.

The ratio γ_s/γ_q shown in bottom portion of Fig. 3.5 is systematically smaller than unity, consistent with many years of prior analysis: when $\gamma_q = 1$ is tacitly chosen, this ratio is the value of γ_s in analysis of strange baryons. We have not imposed a constraint on the range of γ_q (top of Fig. 3.5) and thus values greater than the pion condensation point $\gamma_q^* = e^{m_\pi/2T} \simeq 1.65$ (thick line) can be expected, but in fact do not arise.

It is important to explicitly check how well the particle m_\perp -spectra are reproduced. We group all bins in one figure and show in Figs. 3.6, 3.7, 3.8, 3.9 in

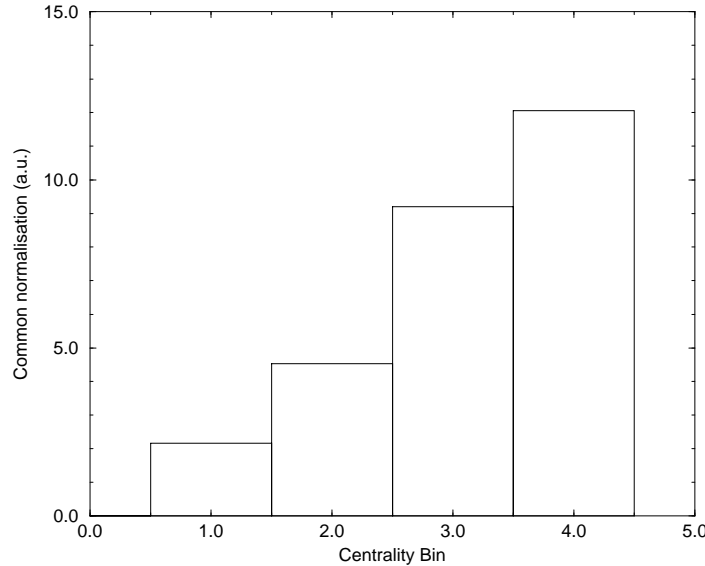


Figure 3.3: Hadronization volume (arbitrary units) for different centrality bins.

sequence Λ , $\bar{\Lambda}$, Ξ , $\bar{\Xi}$. It is important to note that there are some significant deviations which appear to be falling outside of the trend set by the other measurements. –this occurs for Λ as well but remains invisible in the figure due to the smallness of the experimental error bar. Overall, the description of the shape of the spectra is very satisfactory.

We also describe the K_0 data extremely well, especially in the m_\perp range which is the same as that for hyperons considered earlier, as is seen in Fig. 3.10. We recall that these results were obtained reducing the statistical significance of Kaon data, and thus the conclusion is that hyperons predict both the abundance and shape of kaon spectra. Moreover, all the strange hadron spectra can be well described within the model we have adopted.

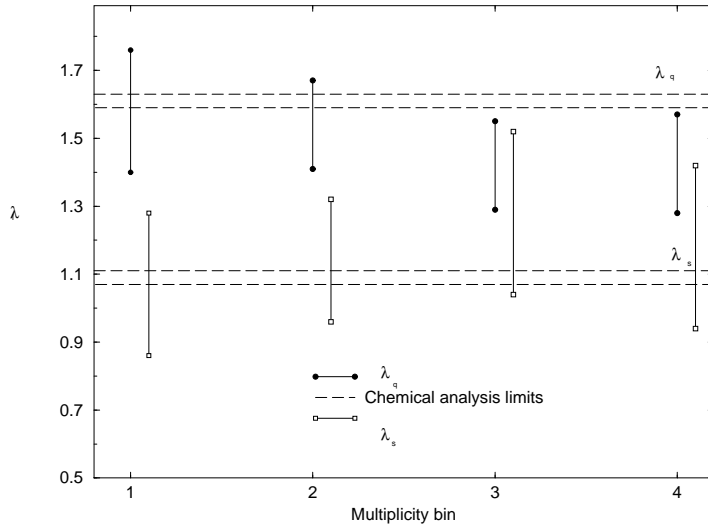


Figure 3.4: Thermal analysis chemical quark fugacity λ_q (top) and strange quark fugacity λ_s (bottom) for different centrality bins compared to the chemical freeze-out analysis results.

3.5 Statistical significance of the results presented

We have analysed the validity and consistency of our data analysis by exploring χ^2/DoF profiles. These are obtained by fixing the value of one of the parameters (we consider $T_f, v, \partial t_f / \partial r_f = 1 / \partial t_f$), and computing the related χ_T^2/DoF , the total error divided by degrees of freedom. These are the number of measurements minus number of parameters, DoF is typically 33 in this data analysis. All curves must have the same χ_T^2/DoF at the minimum and this minimum must point to the value of parameters we report. For the temperature T we produced two results shown in Fig. 3.12, in the bottom section for experimental (statistical) K^0 measurement error, and in the top part for the five times enlarged error. We recall that both results are presented in Fig. 3.1. We note that there is a pronounced χ_T^2/DoF minimum shown on logarithmic scale) for all 8 results of which the average value

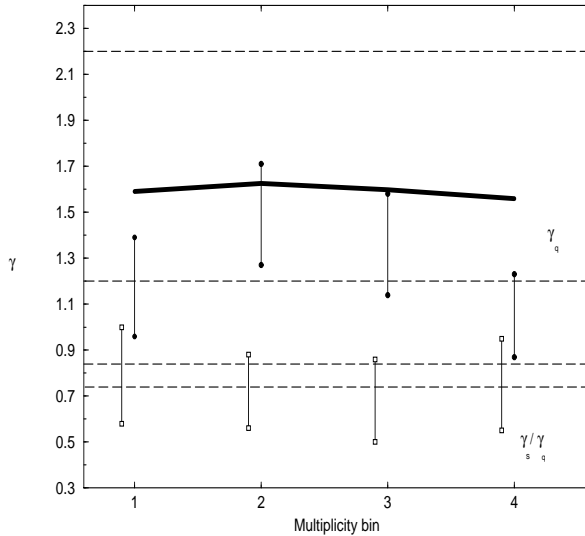


Figure 3.5: Thermal analysis chemical quark abundance parameter γ_q (top) and γ_s/γ_q (bottom) for different centrality bins compared to the chemical freeze-out analysis. Thick line: upper limit due to pion condensation.

is at $T = 145$ MeV. We show in Fig. 3.13 the profile of $\chi^2_{\text{T}}/\text{DoF}$ for the collective flow velocity v (top) and the freeze-out surface $\partial t_f/\partial r_f = 1/\frac{\partial r_f}{\partial t_f}$ motion (bottom) being fixed. These minima can be shown on linear scale. We note a mild secondary minimum in the region $v \simeq 0.25\text{--}0.35$. However, the minima we find at $v = 0.5\text{--}0.58$ are by far more significant. $\partial t_f/\partial r_f = 1/\frac{\partial r_f}{\partial t_f}$ is converging to a sharp minimum seen in bottom portion of Fig. 3.13 at a value consistent with the sudden breakup scenario. It is necessary to include $\partial t_f/\partial r_f = 1/\frac{\partial r_f}{\partial t_f}$ along with v in the analysis to find this result, which was not always done in other studies of particle spectra.

3.6 Omega spectra

In Fig. 3.14 all four centrality bins for the sum $\Omega + \bar{\Omega}$ are shown. We see that we systematically under predict the two lowest m_{\perp} data points. Some deviation at

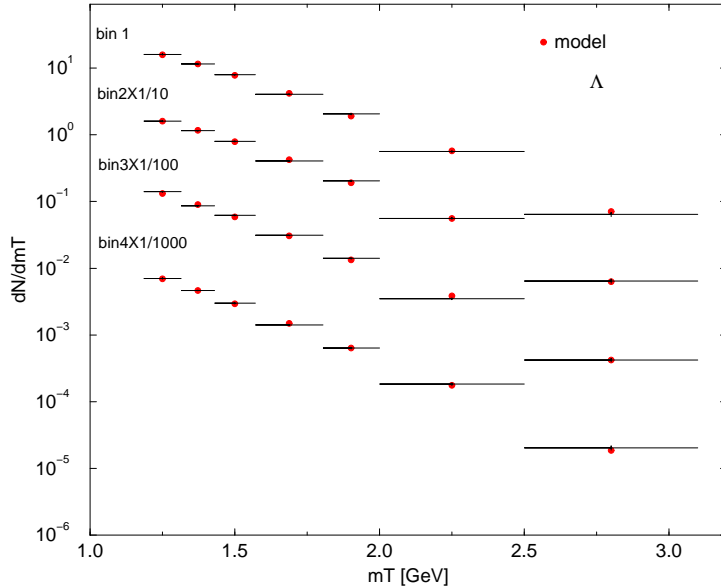


Figure 3.6: (color online) Thermal analysis m_T spectra: Λ .

high m_\perp may be attributable to acceptance uncertainties, also seen in the the Ξ result presented earlier in Fig. 3.9. We recall that there is a disagreement with the Omega yields in the chemical analysis, which thus does not include in the analysis the production of Ω . In the here presented analysis we see that this disagreement is arising at low momentum.

The low- m_\perp anomaly also explains why the inverse m_\perp slopes for $\Omega, \bar{\Omega}$ are smaller than the values seen in all other strange (anti)hyperons. One can presently only speculate about the processes which contribute to this anomaly. We note that the 1–2s.d. deviations in the low m_\perp -bins of the $\Omega + \bar{\Omega}$ spectrum translates into 3s.d. deviations from the prediction of the chemical analysis. This is mainly a consequence of the fact that after summing over centrality and m_\perp , the statistical error which dominates $\Omega + \bar{\Omega}$ spectra becomes relatively small, and as can be seen the low m_\perp excess practically doubles the Ω yield.

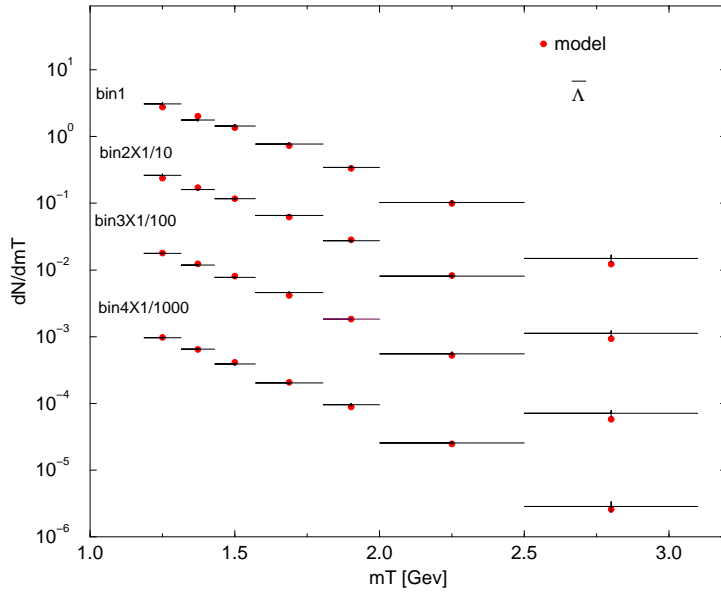


Figure 3.7: (color online) Thermal analysis m_T spectra: $\bar{\Lambda}$.

3.7 Discussion of SPS spectra

Our thermal freeze-out analysis confirms that CERN-SPS results decisively show interesting and new physics, and confirms the reaction picture of a suddenly hadronizing QGP-fireball with both chemical and thermal freeze-out being the same. In our view driven by internal pressure, a quark-gluon fireball expands and ultimately a sudden breakup (hadronization) into final state particles occurs which reach detectors without much, if any, further rescattering. The required sudden fireball breakup arises as the fireball super-cools, and in this state encounters a strong mechanical instability (Letessier and Rafelski 2000). Note that deep super cooling requires a first order phase transition.

The remarkable similarity of m_{\perp} spectra reported by the WA97 experiment

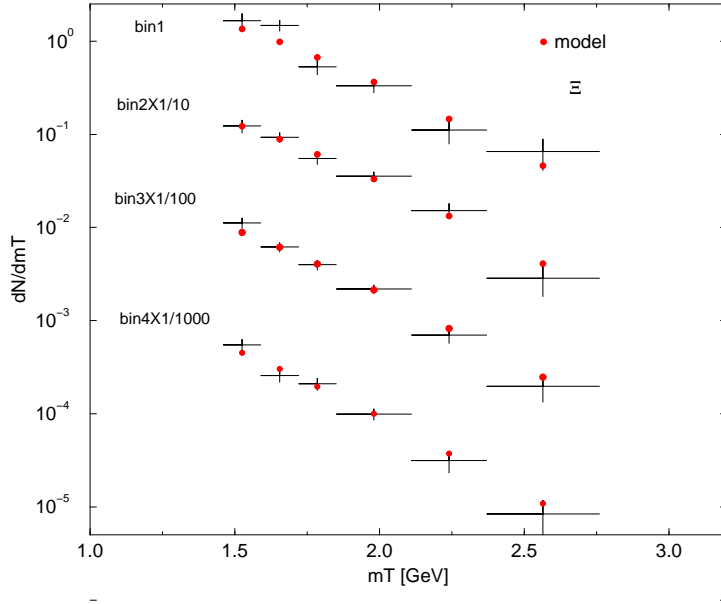


Figure 3.8: (color online) Thermal analysis m_T spectra: Ξ .

is interpreted by a set of freeze out parameters, and we see that production mechanism of Λ , $\bar{\Lambda}$, and Ξ , $\bar{\Xi}$ is the same. This symmetry, including matter–antimatter production is an important cornerstone of the claim that the strange antibaryon data can only be interpreted in terms of direct particle emission from a deconfined phase.

The reader must remember that in presence of conventional hadron collision based physics, the production mechanism of antibaryons is quite different from that of baryons and a similarity of the m_T spectra is not expected. Moreover, even if QGP is formed, but a equal phase of confined particles is present, the annihilation of antibaryons in the baryon rich medium created at CERN-SPS energy would deplete more strongly antibaryon yields, in particular so at small particle momentum, with the more abundant baryons remaining less influenced. This effect is not observed (Bruno et al. 2003).

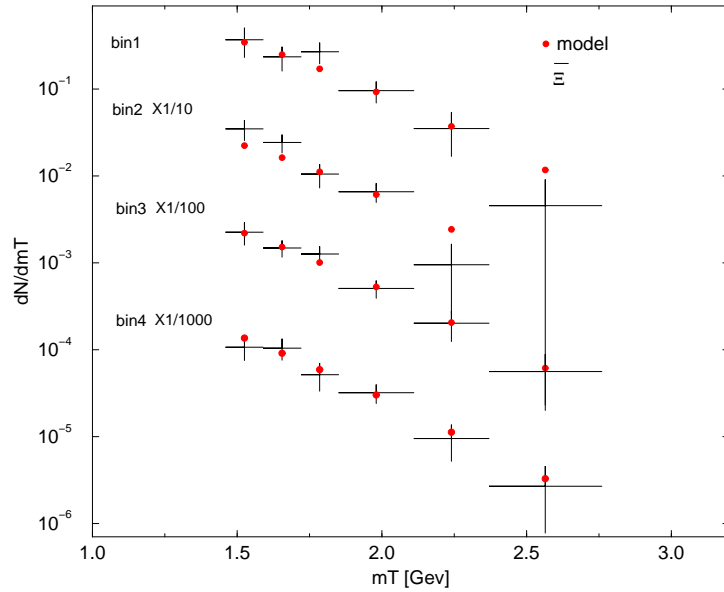


Figure 3.9: (color online) Thermal analysis m_T spectra: Ξ .

Similarity of m_{\perp} -spectra does not at all imply in our argument a similarity of particle rapidity spectra. As hyperons are formed at the fireball breakup, any remaining longitudinal flow present among fireball constituents will be imposed on the product particle, thus Λ -spectra containing potentially two original valence quarks are stretched in y , which $\bar{\Lambda}$ - y -spectra are not, as they are made from newly formed particles. All told, one would expect that anti-hyperons can appear with a thermal rapidity distribution, but hyperons will not. But both have the same thermal-explosive collective flow controlled shape of m_{\perp} -spectra.

We have shown that thermal freeze-out condition for strange hadrons ($K_s^0, \Lambda, \bar{\Lambda}, \Xi, \bar{\Xi}$) agrees within error with chemical freeze-out and we have confirmed the freeze-out temperature $T \simeq 145$ MeV. These findings about the similarity of thermal and chemical freeze-out were controversial, when the experimental single

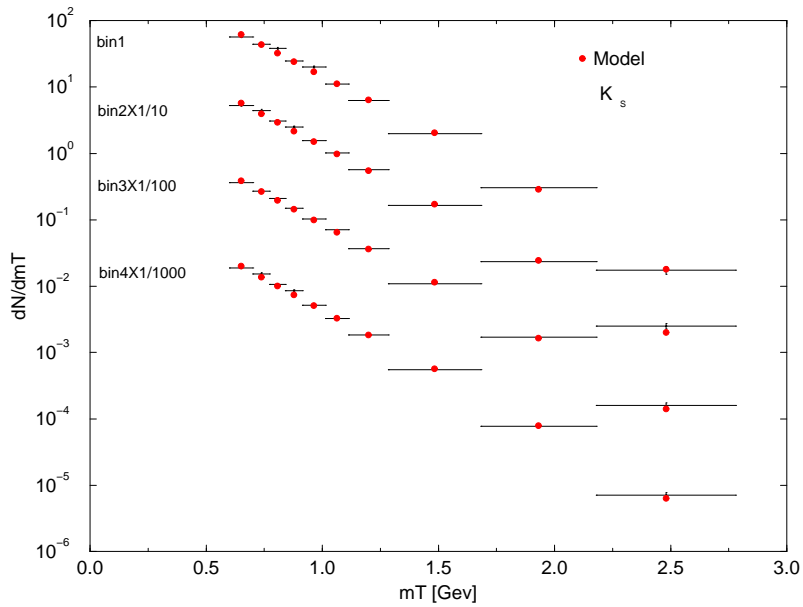


Figure 3.10: (color online) Thermal analysis m_T spectra: K_s .

particle spectra were lacking precision, since pion spectra and two particle correlation analysis did not yield this result. However, this paper studies the precise hyperon and kaon m_\perp spectra which reach to relatively low p_\perp and compares with definitive chemical analysis of SPS data. The two particle correlation analysis involves pions, which unlike strange hadrons here considered, are potentially witnesses to other physics than the properties of dense and hot quark-gluon phase.

We were able to determine the freeze-out surface $1/\frac{\partial r_f}{\partial t_f} = \partial t_f/\partial r_f$ dynamics and have shown that the break-up velocity $\frac{\partial t_f}{\partial r}$ is nearly the velocity of light, as would be expected in a sudden breakup of a QGP fireball. A study with $\partial t_f/\partial r_f$ has not been previously considered, and only collective flow is included in the description of the particle source. In our analysis we find a slight increase of the transverse

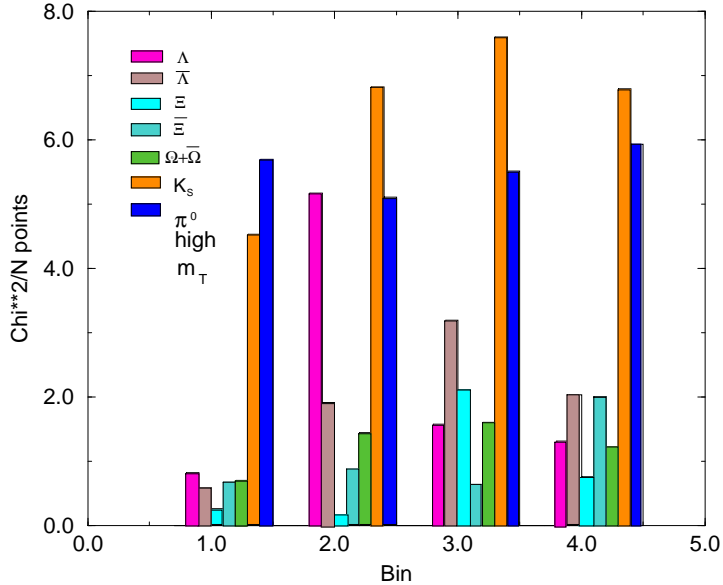


Figure 3.11: (color online) χ^2/Dof per particle data point. As can be seen, K_s (error given by the experiment) gives the dominant discrepancy .

expansion velocity with the size of the fireball volume, but consistently $v \leq 1/\sqrt{3}$.

We have reproduced the strange particle spectra in all centrality bins. Our findings rely strongly on results obtained by WA97 at smallest accessible particle momentum, and this stresses the need to reach to smallest possible p_\perp in order to be able to explore the physics of particle freeze-out from the deconfined region. Moreover, we demonstrated that the experimental production data of $\Omega + \bar{\Omega}$ has a noticeable systematic low p_\perp enhancement anomaly present in all centrality bins. This result shows that it is not a different temperature of freeze-out of $\Omega + \bar{\Omega}$ that leads to more enhanced yield, but a soft momentum secondary source which contributes almost equal number of soft $\Omega + \bar{\Omega}$ compared to the systematic yield predicted by the other strange hadrons.

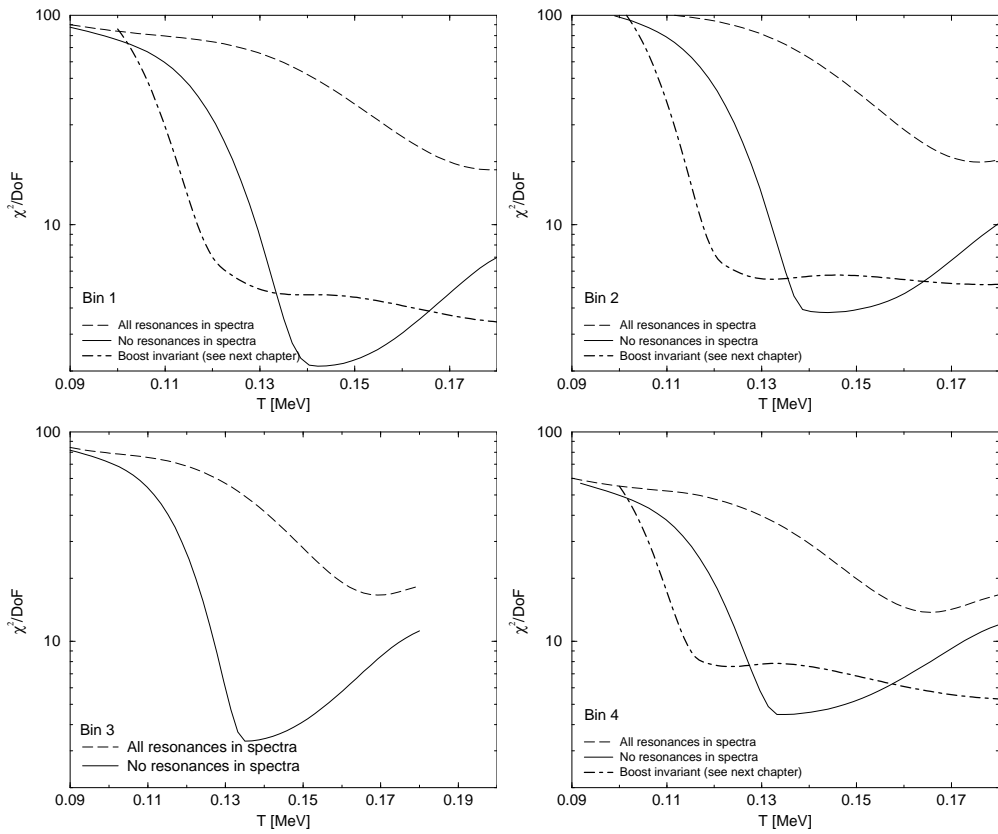


Figure 3.12: The total error divided by degrees of freedom for different centrality bins, shown as function of (fixed) freeze-out temperature T , bottom for the experimental value of the (statistical) K^0 error, top for the 5 times enlarged kaon data statistical errors.

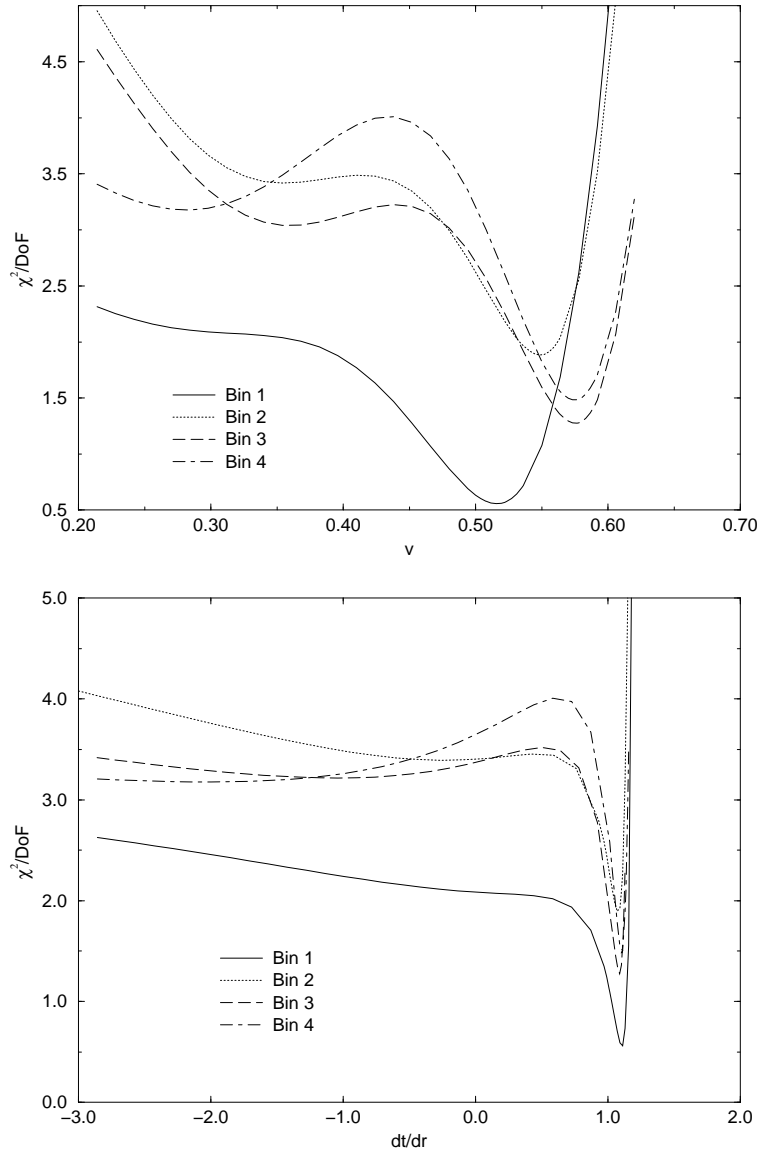


Figure 3.13: The total error divided by degrees of freedom for different centrality bins, shown as function of (fixed) flow velocity v on top and for (fixed) freeze-out surface $\partial t_f / \partial r_f = 1 / \frac{\partial r_f}{\partial t_f}$ dynamics on the bottom.

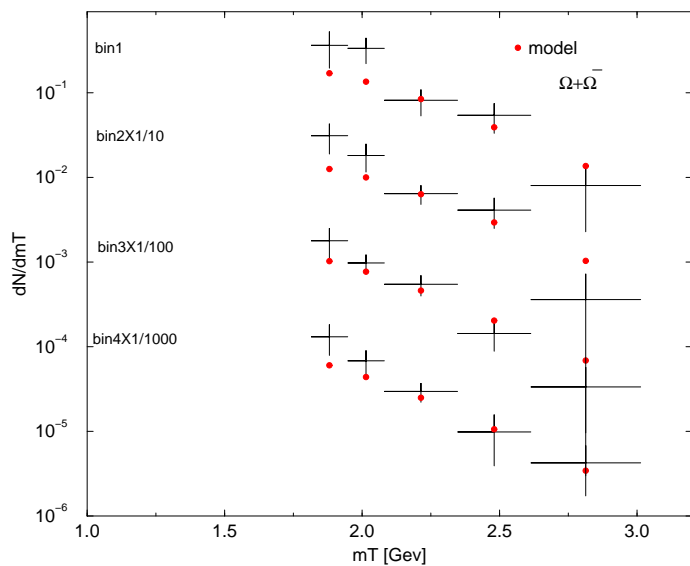


Figure 3.14: (color online) Thermal analysis m_T spectra: $\Omega + \bar{\Omega}$.

CHAPTER 4

Particle spectra at RHIC: A boost-invariant ansatz

4.1 Boost-invariant statistical hadronization

4.1.1 General remarks

The advent of RHIC data has coincided with the consensus that a model based on statistical hadronization, combined with transverse expansion, can explain both the abundancies and the transverse momentum distributions of hadrons produced in heavy ion collisions. The fitted parameters, and in particular the temperature, however, have varied considerably, ranging from as low as 110 MeV (Burward-Hoy 2003; Afanasiev et al. 2003) to 140 MeV (Rafelski and Letessier 2003d) to as high as 160 and 170 MeV (Baran et al. 2004; Braun-Munzinger et al. 2001).

Such discrepancies are not very surprising, since the models differ considerably. However, this means that before we can say that the freeze-out temperature has been determined, we must understand precisely the origins of these differences, and try to ascertain which model is “the best”, both in terms of physical reasonableness and as an ansatz to fit the data. We shall proceed to give an overview of the ways in which these models differ.

Firstly, spectra are normalized very differently in different models. Some recent work fits the particle slopes only (Burward-Hoy 2003; Hohne et al. 2003;

Sandor et al. 2004; Adams et al. 2003b), treating the normalization of each particle as a free parameter. This approach can be argued for assuming a long-lived post-hadronization “interacting hadron gas phase” in which individual hadron abundances subject to inelastic interactions evolve away from chemical equilibrium. This particular reaction picture clashes with e.g. the fact that short-lived resonance ratios can be described within the statistical hadronization model using the chemical (statistical hadronization) freeze-out temperature obtained in stable particle studies ((Braun-Munzinger et al. 2001) and next chapter). This implies that in principle the relative normalization of the particle spectra should be derived from a hadronization scenario involving flavor chemical potentials. In fact a study of RHIC spectra finds that the normalization can be accounted for (Baran et al. 2004), and that the chemical equilibration temperature also describes particle spectra well. This is suggesting that any post-hadronization re-interaction phase is short and has minor influence on the particle yields.

The problem is that the different ways to derive hadronization particle distributions have a profound effect on the resulting fitted temperature. Temperature affects the absolute number of particles through several mechanisms and anti-correlates with the phase space occupancy parameters $\gamma_i, i = u, d, s$ (Letessier and Rafelski 2000). It has been found that the introduction of these parameters, motivated by the need to conserve entropy at hadronization (Letessier and Rafelski 2000) decrease the χ^2 / per degree of freedom considerably and lowers the freeze-out temperature by 30 MeV (Letessier and Rafelski 2000). Other workers assume the light flavors are in chemical equilibrium (Becattini et al. 2003; Braun-Munzinger et al. 1999; Braun-Munzinger et al. 2001; Baran et al. 2004).

Additionally, when fitting the particle spectra, the system's spatial shape and the way the freeze-out progresses in time have a considerable effect on the form of particle distributions, and hence on the fitted temperature and matter flow. The impact of freeze-out geometry and dynamics on particle spectra were examined well before RHIC data became available (Sollfrank et al. 1990) and it was realized that an understanding of freeze-out is essential for the statistical analysis of the fireball (Heinz and Kolb 2002). Even though this matter has been clearly recognized, a systematic analysis of how freeze-out geometry affects particle distributions is for the first time attempted here. In fact, each of the models used in the study of particle spectra (Hohne et al. 2003; Adams et al. 2003b; Burward-Hoy 2003; Baran et al. 2004) employs a different choice of freeze-out geometry, based on different, often tacitly assumed, hadronization scenarios. Thus an understanding for the influence of hadronization mechanism is impossible to deduce from this diversity.

4.1.2 Freeze-out geometry

At RHIC collision energies the measured $dN/d\eta$ (Olszewski et al. 2002; Staszek et al. 2002) indicates that around mid-rapidity the system conditions can be approximated by the Bjorken picture (Bjorken 1983).

To describe particle spectra measured around mid-rapidity, therefore, boost invariance becomes the dominant symmetry on which freeze-out geometry should be based. We shall construct a general hadronization scenario, combining the cut Cooper-Frye formula (Eq. (2.18)) with boost-invariance.

A particle's energy at rest with respect to the collective flow is given by

combining the flow field (parametrized by the transverse and longitudinal rapidities $y_{L,T}$ as well as the emission angle θ) with the observed particle's momentum (parametrized by the rapidity y , transverse momentum p_T and angle ϕ)

$$u^\mu = \begin{pmatrix} \cosh(y_L) \cosh(y_T) \\ \sinh(y_T) \cos(\theta) \\ \sinh(y_T) \sin(\theta) \\ \sinh(y_L) \cosh(y_T) \end{pmatrix}, \quad p^\mu = \begin{pmatrix} m_T \cosh(y) \\ p_T \cos(\phi) \\ p_T \sin(\phi) \\ m_T \sinh(y) \end{pmatrix} \quad (4.1)$$

The rest energy will then be

$$p_\mu u^\mu = m_T \cosh(y_T) \cosh(y - y_L) - \sinh(y_T) \cos(\theta - \phi) p_T. \quad (4.2)$$

The requirement for the Bjorken picture is that the emission volume element has the same y_L dependence:

$$p_\mu d^3\Sigma^\mu \sim A \cosh(y - y_L) + B. \quad (4.3)$$

This constrains the freeze-out hypersurface to be of the form

$$\Sigma^\mu = (t_f \cosh(y_L), x, y, t_f \sinh(y_L)). \quad (4.4)$$

Here t_f is a parameter invariant under boosts in the z direction, whose physical significance depends on the model considered.

For central collisions, a further simplifying constraint is provided by the cylindrical symmetry, which forces t_f , as well as y_L and y_T , to be independent of the angles θ and ϕ . The freeze-out hypersurface can be parametrized, in this case, as

$$\Sigma^\mu = (t_f(r) \cosh(y_L), r \sin(\theta), r \cos(\theta), t_f(r) \sinh(y_L)), \quad (4.5)$$

$$d^3\Sigma^\mu = t_f r dr d\theta dy_L \left(\cosh(y_L) \frac{\partial t_f}{\partial r} \cos(\theta), \frac{\partial t_f}{\partial r} \sin(\theta), \sinh(y_L) \right) \quad (4.6)$$

And the emission element takes the form

$$p^\mu d^3\Sigma_\mu = \left[m_T \cosh(y - y_L) - p_T \frac{\partial t_f}{\partial r} \cos(\theta - \phi) \right] t_f r dr d\theta dy_L, \quad (4.7)$$

with the same dependence on the angle as Eq. (4.2).

Putting Eq. (4.2) and Eq. (4.7) together, the particle's momentum distribution function in the Boltzmann approximation is given by

$$E \frac{dN}{d^3p} \propto \left[m_T \cosh(y - y_L) - p_T \frac{\partial t_f}{\partial r} \cos(\theta - \phi) \right] \exp \left[-\frac{m_T \cosh(y_T) \cosh(y - y_L) - \sinh(y_T) \cos(\theta - \phi) p_T}{T} \right] t_f r dr d\theta dy_L \quad (4.8)$$

(the quantum statistics case, relevant for π , can be obtained through the prescription in Eq. (3.6)). For an approximately boost-invariant cylindrical system we can use Bessel functions to perform the integrals over y_L and θ analytically

$$K_n(z) = \int_{-\infty}^{\infty} \cosh(ny) e^{-\cosh(y)} dy \quad (4.9)$$

$$I_n(z) = \frac{1}{2\pi} \int_0^{2\pi} \cos(n\theta) e^{-\cos(\theta)} d\theta \quad (4.10)$$

and obtain

$$E \frac{dN}{d^3p} \propto m_T I_0(\alpha p_T) K_1(\beta m_T) - p_T \frac{\partial t_f}{\partial r} I_1(\alpha p_T) K_0(\beta m_T) \quad (4.11)$$

What distinguishes the models currently considered is the time component of the freeze-out surface. The most general freeze-out hypersurface compatible with cylindrical symmetry is provided by Eq. (4.5). Generally, t_f (a generic function of r) represents the time, in a frame co-moving with the longitudinal flow, at which the surface at distance r freezes out.

The fits in Refs. (Burward-Hoy 2003; ?; Adams et al. 2003b) are based on a particular case of such a freeze-out surface, in which t_f is completely independent

of r ($\partial t_f / \partial r = 0$). Such a picture's physical reasonableness can be questioned, e.g., why should spatially distant volume elements, presumably with different densities and moving at different transverse velocities, all freeze out simultaneously in a longitudinally co-moving frame?. However, such a simple model can perhaps serve as an approximation.

More generally, the “burning log” model, discussed in the last chapter for the spherically symmetric case, assumes that the emission occurs through a three-dimensional hadronization surface which is moving at a constant “velocity” ($\partial t_f / \partial r$) throughout the fireball. Both boost-invariant and spherically symmetric versions of burning log model were considered. Even if the hadronization velocity encompasses an extra parameter, it is worth considering since it is based on a physically motivated hadronization picture. Moreover, the burning log picture is a suitable framework in the study of sudden hadronization. Sudden hadronization occurs when the fireball encounters a mechanical instability, which combined with the fireball's high transverse flow ensures that the emission surface spreads to the interior of the fireball with $\partial t_f / \partial r \simeq c$. All of the indications suggested for such a picture seem to be borne out by both SPS and RHIC data (Letessier and Rafelski 2000; Rafelski and Letessier 2003d).

An approach based on the hypothesis of initial state “synchronization” by the primary instant of collision and the following independent but equivalent evolution of all volume elements assumes that each element of the system undergoes freeze-out at the same proper time τ . In this framework each fireball element expands and cools down independently, hadronizing when its temperature and density

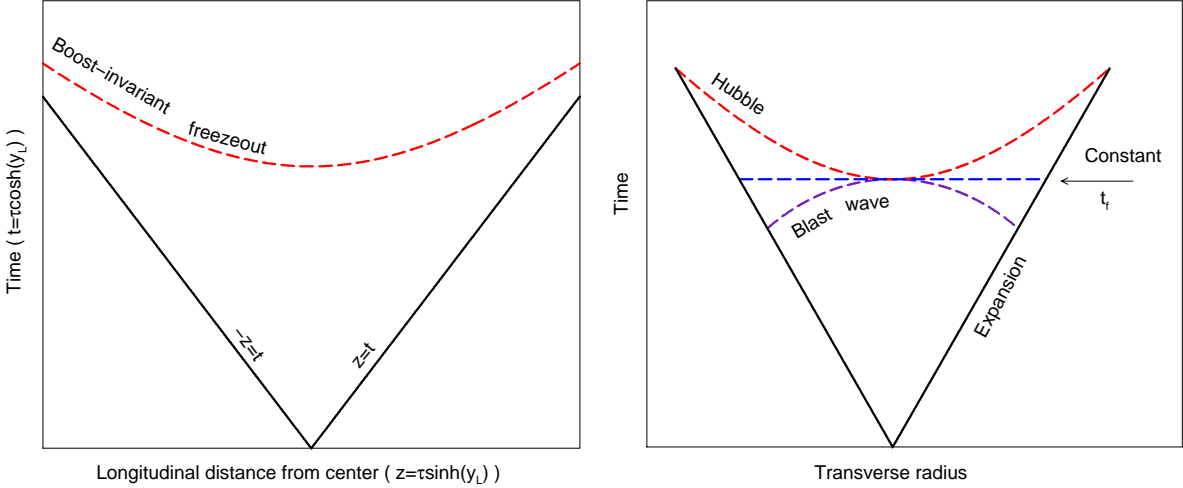


Figure 4.1: (Color on-line) While boost-invariance fixes the longitudinal freeze-out structure (left), several scenarios exist for the transverse dependence of freeze-out (right). For spherical freeze-out, only plot on the right applies .

Table 4.1: (Color on-line) Freeze-out hypersurfaces at contours of constant radii.

Surface	Σ^μ	$E \frac{dN}{dp^3}^{-1}$
Constant t_f $\partial t_f / \partial r = 0$	$\begin{pmatrix} t_f \\ \vec{r} \end{pmatrix}$	$m_T K_1(\beta m_T) I_0(\alpha p_T)$
Hubble (constant τ_f)	$\tau_f \begin{pmatrix} \cosh(y_L) \cosh(y_T) \\ \sinh(y_T) \cos(\theta) \\ \sinh(y_T) \sin(\theta) \\ \sinh(y_L) \cosh(y_T) \end{pmatrix}$	$m_T \cosh(y_T) I_0(\alpha p_T) K_1(\beta m_T) - p_T \sinh(y_T) I_1(\alpha p_T) K_0(\beta m_T)$
burning log (boost invariant)	$\begin{pmatrix} t_f(r) \cosh(y_L) \\ r \cos(\theta) \\ r \sin(\theta) \\ t_f(r) \sinh(y_L) \end{pmatrix}$	$m_T I_0(\alpha p_T) K_1(\beta m_T) - p_T \frac{\partial t_f}{\partial r} I_1(\alpha p_T) K_0(\beta m_T)$
burning log (spherical)	$\begin{pmatrix} t_f \\ r \vec{e}_r \end{pmatrix}$	$e^{-E/T} \sqrt{\frac{T}{p_T \sinh(y_T)}} (E I_{1/2}(\alpha p_T) - p_T \frac{\partial t}{\partial r} I_{3/2}(\alpha p_T))$

reach the critical value. This model was successfully used to describe RHIC m_T -spectra (Baran et al. 2004). In this approach t_f in Eq. (4.5) is equal to $\tau \cosh(y_T)$ and the hadronization hypersurface in Eq. (4.6) becomes proportional to the flow vector:

$$\Sigma^\mu = \tau u^\mu \quad (4.12)$$

$$d^3\Sigma^\mu = \tau r dr d\theta dy_L u^\mu = dV u^\mu \quad (4.13)$$

$$r = \tau \sinh(y_T). \quad (4.14)$$

In this hadronization model the heavy ion fireball behaves similarly to the expanding Hubble universe. In the ‘Hubble’ scenario, the Cooper-Frye formula reduces to the Touscheck Covariant Boltzmann distribution (Letessier and Rafelski 2002; Touschek 1968; Hagedorn et al.).

$$\frac{V_0 d^3 p}{(2\pi)^3} e^{-E/T} \rightarrow \frac{V_\mu p^\mu}{(2\pi)^3} d^4 p 2\delta_0(p^2 - m^2) e^{-p_\mu u^\mu/T} \quad (4.15)$$

$$V^\mu = V_0 u^\mu \quad (4.16)$$

(Where V is the co moving fireball’s volume element in the local rest frame.)

To summarize and illustrate the diversity of distinct hadronization geometries we present in Table 4.1 and Fig. 4.1 the freeze-out scenarios examined here. As we shall see the choice of freeze-out geometry produces in a fit of experimental data a non trivial effect capable of altering significantly the understanding of statistical hadronization parameters.

4.1.3 Flow profile

Hydrodynamical expansion of the fireball implies in general that each volume element will have a different density and transverse expansion rate. For this reason,

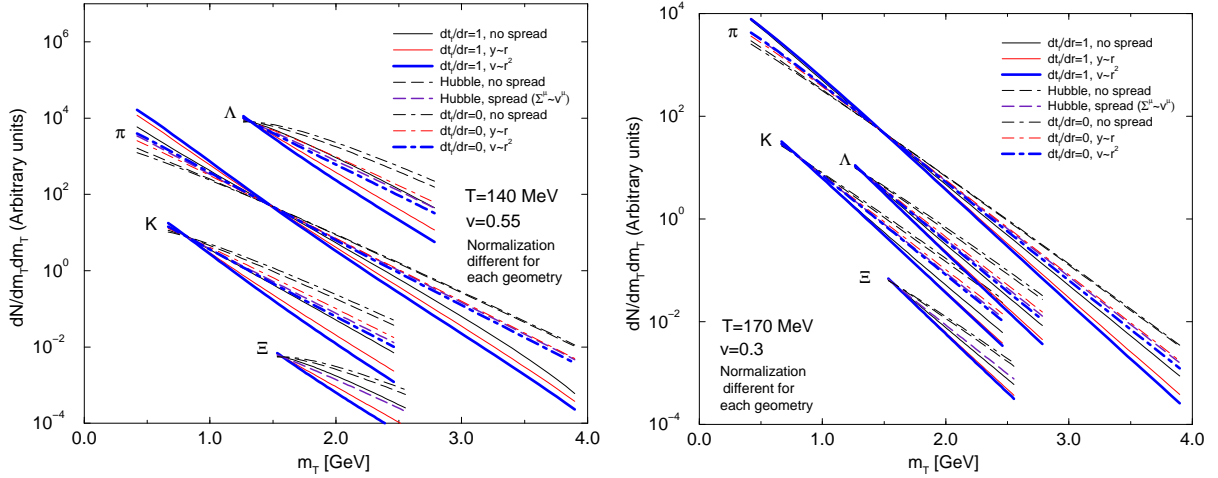


Figure 4.2: (Color on-line) π, K, Λ and Ξ m_T distributions obtained with different freeze-out models and flow profiles. For this and subsequent figures, a uniform density profile was assumed .

the integral over $d^3\Sigma$ can span a range of flows, weighted by density. In first approximation one can fit data using just an “average” flow velocity throughout the entire fireball (Sandor et al. 2004; Torrieri and Rafelski 2001a):

$$\begin{aligned} E \frac{dN}{d^3p} &= \int r dr (E - p_T \frac{dt_f}{dr}) f(T, y_T(r), \lambda) \\ &\propto (E - p_T \frac{dt_f}{dr}) f(T, \langle y_T \rangle, \lambda). \end{aligned} \quad (4.17)$$

However, if one wants to properly identify $\frac{dt_f}{dr}$, the flow profile should be taken into account. Hydrodynamic simulations (Teaney et al. 2001) accompanied by assumption that freeze-out happens when a volume element reaches a critical energy density indicate that the transverse rapidity will depend linearly with the radius i.e. $y_T \sim \tanh(r)$. This condition, however, is appropriate for a static freeze-out and will not in general hold if the freeze-out is sudden. Other flow profiles have been tried in the literature, arising from dynamical hypothesis. For example, the assumption that the freeze-out occurs at the same time t_f results in a quadratic ($v \propto r^2$) flow

profile (Schnedermann and Heinz 1993), which has also been used recently in fits to data (Adams et al. 2003b). In the Hubble fireball (Baran et al. 2004) the freeze-out conditions will also result in a distinctive flow profile. Specifically with $\Sigma^\mu \propto u^\mu$, we have $\gamma v \propto r$.

Density profiles also depend on the assumed initial condition and the equation of state of the expanding QGP. It has been shown (Aggarwal et al. 1999) that different density choices have a considerable effect on both the temperature and flow fits at SPS energies.

Fig. 4.2 shows how the choice in hadronization dynamics and flow profiles at same given freeze-out temperature and transverse flow can result in a range of inverse spectral slopes. Here the density profiles were assumed to be uniform. It is clear that the same freeze-out parameters give rise to a variety of substantially different particle spectra. Conversely, fits to experimental data will only produce reliable information on the freeze-out conditions if and when we have a prior knowledge of the hadronization geometry and dynamics. Therefore, conclusions about statistical model fits, as well as arguments whether freeze-out occurs simultaneously for different particles or not, cannot be answered while the models used to fit the data are plagued by such uncertainties.

We now proceed to use a Monte-Carlo method to calculate the effect these uncertainties have on fitted data. Afterwards, we will apply a range of fits to RHIC models to see if the “right” hadronization model can be isolated from particle spectra alone.

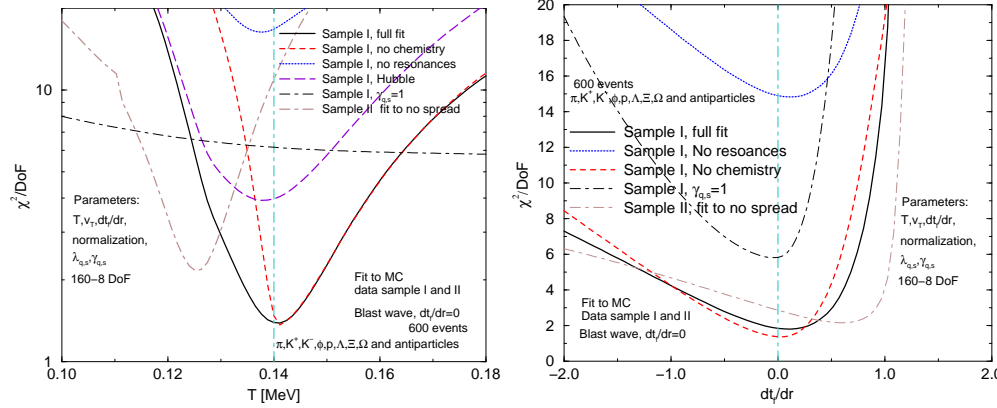


Figure 4.3: (color on-line) Results of fits to Monte-Carlo generated data samples I and II ($\frac{dt_f}{dr} = 0$): χ^2 profiles for temperature (left) and fitted $\partial t_f/\partial r$ (right). The models used in the fits are described in sections 1.1 and 1.2. Full fit includes fitted chemical potentials and $\gamma_{q,s}$, resonances and fitted $\partial t_f/\partial r$. Last profile shows effect of fitting sample II using Eq. (4.17) .

4.2 Sensitivity to model choice

The ambiguities presented in the previous section mean that it is important to study their effect on the statistical model's fitted parameters. One way to do this is to use a Monte-Carlo to generate data according to a particular freeze-out model, and to see what happens if the “wrong” model is used to perform the fit. We have written a Monte-Carlo program which can be used for this purpose. An acceptance/rejection algorithm is used to generate particles in a statistical distribution in the volume element's rest frame. The accepted particles are then Lorentz transformed to the lab frame. (Any flow and density profile, as well as any freeze-out surface can be accommodated). Resonance decays are handled through Eq. (2.34), using the MAMBO algorithm (Kleiss and Stirling 1992) to generate points in phase space. Output can be used to generate spectra or fed into a microscopic model such as

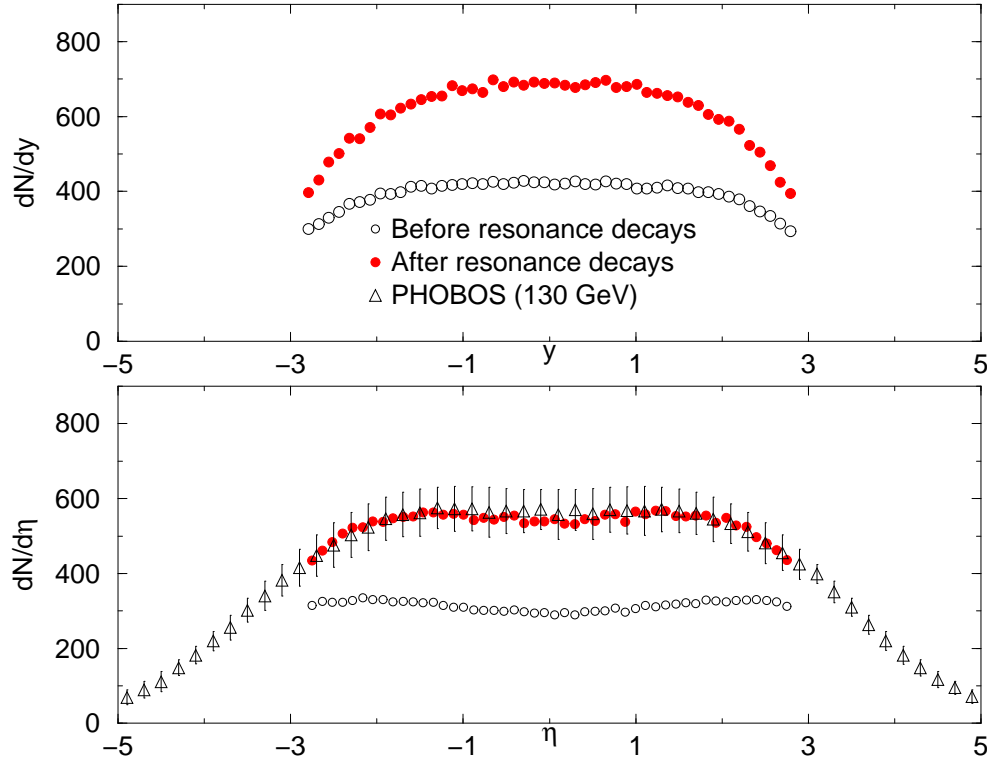


Figure 4.4: (color on-line) $dN_{tot}/d(y, \eta)$ arising from freeze-out of a Bjorken fluid, before (open circles) and after (solid circles) resonance decays. The normalization is arbitrary, chosen to coincide with PHOBOS data (triangles) .

uRQMD (Bass et al. 1998).

The Monte-Carlo output was used to produce the data points in Fig. 4.4. It can be seen that a boost-invariant statistical hadronization can explain the global properties of the system such as $dN_{tot}/d\eta$. It can also be verified that the role of resonances is absolutely crucial. We proceeded to generate three datasets of particles. Each data set had a temperature of 140 MeV, a maximum transverse flow of 0.55, and out of equilibrium chemistry ($\gamma_q = 1.4, \gamma_s/\gamma_q = 0.8$). Generated particles include $\pi, K^+, K^-, p, \bar{p}, \Lambda, \Xi, \Omega$ and their resonances. The three samples differ in their choice of freeze-out geometry (specifically $\partial t_f/\partial r$) and flow profile:

Sample I $\partial t_f/\partial r = 0$ and no flow profile, as fitted in (Sandor et al. 2004)

Sample II $\partial t_f/\partial r = 0$ and a quadratic flow profile, as fitted in (Burward-Hoy 2003; Hohne et al. 2003; Adams et al. 2003b)

Sample III $\partial t_f/\partial r = 1$, the boost-invariant analogue of (Torrieri and Rafelski 2001a).

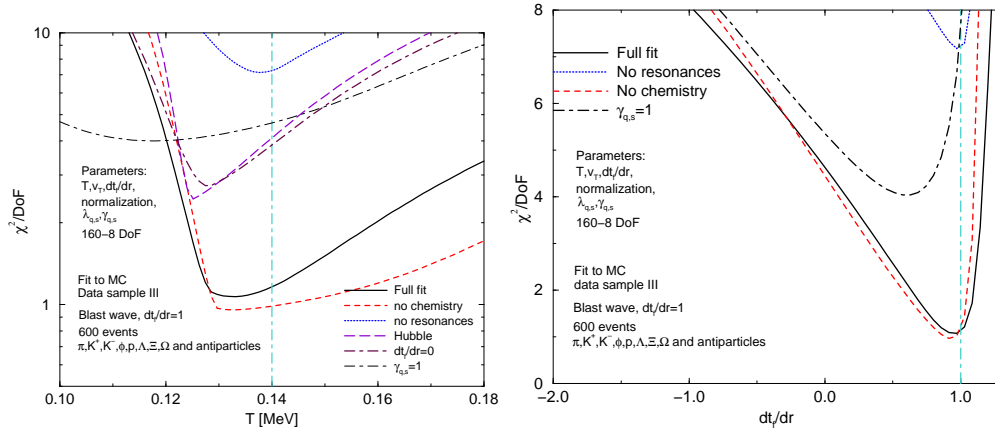


Figure 4.5: (color on-line) Results of fits to Monte-Carlo generated data samples III ($\frac{dt_f}{dr} = 1$): χ^2 profiles for temperature (left) and fitted $\partial t_f/\partial r$ (right). The models used in the fits are described in sections 1.1 and 1.2. Full fit includes fitted chemical potentials and $\gamma_{q,s}$, resonances and fitted $\partial t_f/\partial r$.

We have fitted the three samples to a variety of models, producing χ^2/DoF profiles for freeze-out temperature and the $\partial t_f/\partial r$ parameter. Fig. 4.5 shows the profiles resulting in the fit to sample III while samples I and II are shown in Fig. 4.3. A full chemistry model with resonances (solid black line) seems to be equivalent (as far as the position of the χ^2 minimum and the value of χ^2/DoF) to a fit in which normalization is particle-specific (dashed red line). However, the chemical potential fit has greater statistical significance since considerably more degrees of freedom are required for arbitrary normalization.

If chemical potentials are included resonances become essential since a fit with chemical potentials but no resonances (dotted blue line) loses all statistical significance. Similarly, the physical presence of non-equilibrium ($\gamma_{q,s} \neq 1$) means chemical potentials have to include the non-equilibrium parameter for the fit to be meaningful (black dot-dashed line). The freeze-out geometry does not seem to impact the temperature minimum that much. However, the correct freeze-out geometry can be picked out by a comparison of fits to different models by choosing the model with the lower χ^2/DoF . Moreover, data sensitivity to temperature is strongly affected by freeze-out geometry: Comparing the temperature profiles for different choices of $\partial t_f/\partial r$ (Figs. 4.3 and 4.5) it is apparent that the temperature χ^2 minimum is more definite in the $\partial t_f/\partial r = 0$ case. In the case of explosive freeze-out, the correlation between temperature and other parameters in the fit (notably flow) increases, resulting in a shallow χ^2 increase at larger than minimum temperatures.

Finally it should be noted that flow profile, freeze-out geometry and temperature appear to be strongly correlated. If data sample II is fitted with a distribution with no flow profile (such as Sample I) there is a non-negligible shift in both the fitted temperature and $\partial t_f/\partial r$, and a small rise in χ^2/DoF (Fig. 4.3, brown dot-dashed line).

As fits including both flow profile and resonances are computationally very intensive, we shall have to limit ourselves to the observation that the uncertainty in flow profile is a source of systematic error here. In the following chapter, a probe capable of disentangling flow profile from freeze-out will be developed.

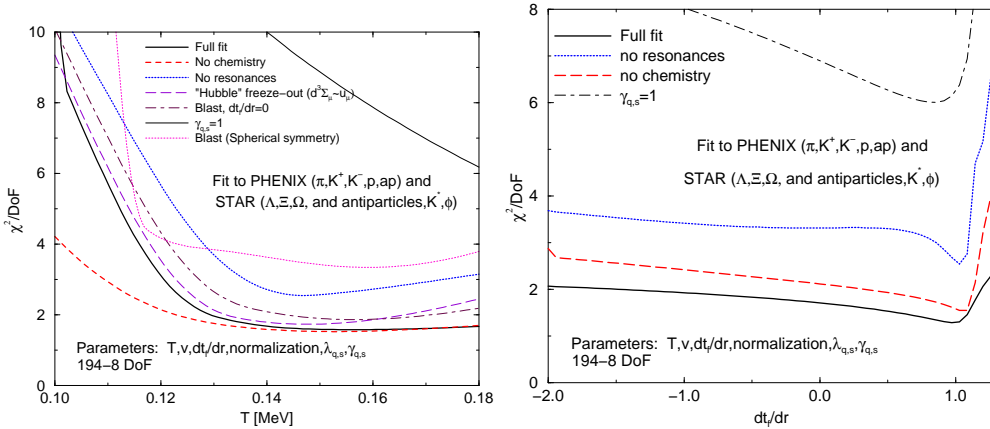


Figure 4.6: (color on-line) Fit to RHIC data profiles for temperature (left) and fitted $\partial t_f/\partial r$ (right). The models used in the fits are described in sections 1.1 and 1.2. Full fit includes fitted chemical potentials and $\gamma_{q,s}$, resonances and fitted $\partial t_f/\partial r$.

4.3 Fit to RHIC data ($\sqrt{s_{NN}} = 130\text{GeV}$)

Finally, we have performed a fit to the available RHIC data. The data sample we used is the same as the one used for the Monte-Carlo, but, since the STAR and PHENIX spectra had different trigger requirements (notably centrality) and acceptance regions, we have used two different system volumes, one for STAR particles and another one for PHENIX.

The results are similar to the Monte Carlo data in many ways. The χ^2/DoF was only slightly larger.

A fit with particle-specific normalization gives a very similar χ^2 and fitted temperature to a fit including chemistry and resonances. If chemistry is included in particle spectra analysis, resonances and non-equilibrium are essential. The fit to freeze-out geometry weakly points to $\partial t_f/\partial r = 1$, a picture that is supported by the temperature χ^2 profile, virtually identical to data sample III. However, we can not

claim our study to be complete in this respect, since we have not yet investigated the effect of including flow profile in the models. As Monte-Carlo simulations have shown, the conclusion can differ once these are taken into account.

Fig. 4.7 shows the hyperon and pion spectra from the global fit of Fig. 4.6. A comparison of the fits on the left panel confirms that a model with no chemistry is about as good at fitting particle spectra as a model with resonances and chemical potentials. However, the second fit also has predictive power: We have used the fitted parameters to predict the m_T spectrum for the Σ^* . Unsurprisingly, we found that the Σ^* should have roughly the same slope as the Ξ s, but its total multiplicity should be about three times as big. We therefore suggest that a greater sample of spectra, in particular more spectra of heavy resonances taken within the same centrality bin as light particles (to make sure both flow and emission volume are the same for each particle) would help in establishing whether chemical potentials are a good way to normalize hadron spectra or not.

The only spectrum which presents a significant systematic deviation for most models is the π^- . As Fig. 4.7 (right panel) shows, most models fail to catch the upward dip of the low momentum pions, and indeed simple transverse expansion predicts the reverse trend (Burward-Hoy 2003; Hohne et al. 2003; Sandor et al. 2004; Adams et al. 2003b). Including resonances, and allowing for $\gamma_q > 1$ helps (the latter is equivalent to postulating a pion “chemical potential” (Tomasik et al. 2003)) However, to fully account for the lowest momentum pions, even addition of resonances and $\gamma_q > 1$ are not enough. One has to add a power-law component to the pion spectrum

$$E \frac{dN}{d^3p} = \left(E \frac{dN}{d^3p} \right)_{cf} + \frac{A}{(p_T + p_{T0})^\alpha} \quad (4.18)$$

This contribution (roughly 6% of the total pion yield in the best fit) also accounts for the highest p_T pions. Such a parametrization has been justified (Hagedorn 1984) and successfully used (Peitzmann 2003) before.

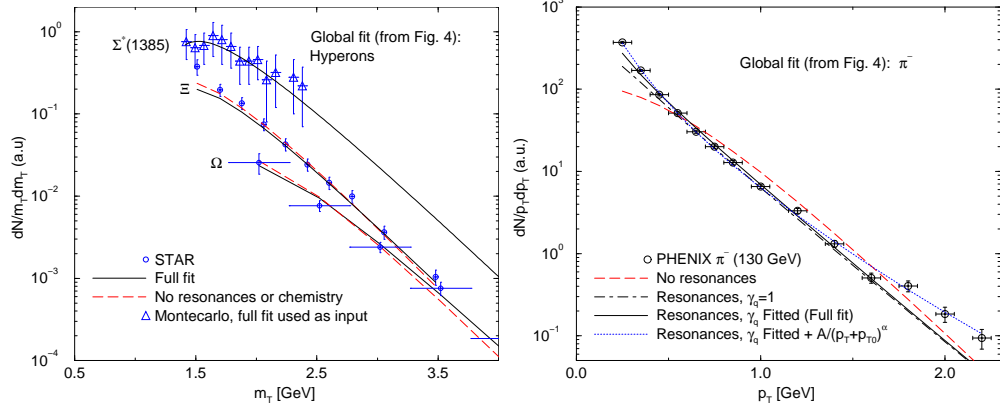


Figure 4.7: (color online) Left: Ξ and Ω m_T distributions, within a global fit including resonances and chemical potentials (Fig. 4.6, solid black) as well as no resonances or chemistry (Fig. 4.6, dashed red). The model with chemical potentials was used to predict the Σ^* m_T distribution using the Monte-Carlo. Right: PHENIX π^- p_T distribution, within the global fit from Fig. 4.6. As can be seen, both resonances and γ_q help, but are not sufficient to explain the pion distribution fully.

Finally, Fig. 4.8 (left) shows the Blast wave fit to the K^* momentum distribution. The fact K^* can be fitted to the same temperature and flow as the stable hadrons is, in itself, remarkable, since it is a short lived resonance detected by invariant mass reconstruction, which potentially decays before freeze-out and whose decay products can be rescattered (and made undetectable) by other particles in the medium. We shall not dwell on this for too long, since the next chapter is mainly devoted to a discussion on directly detectable short-lived resonances. However, it should be mentioned that, as Fig. 4.8 (right) shows, microscopic models predict the rescattering of decay products to be non-trivial and strongly momentum dependant

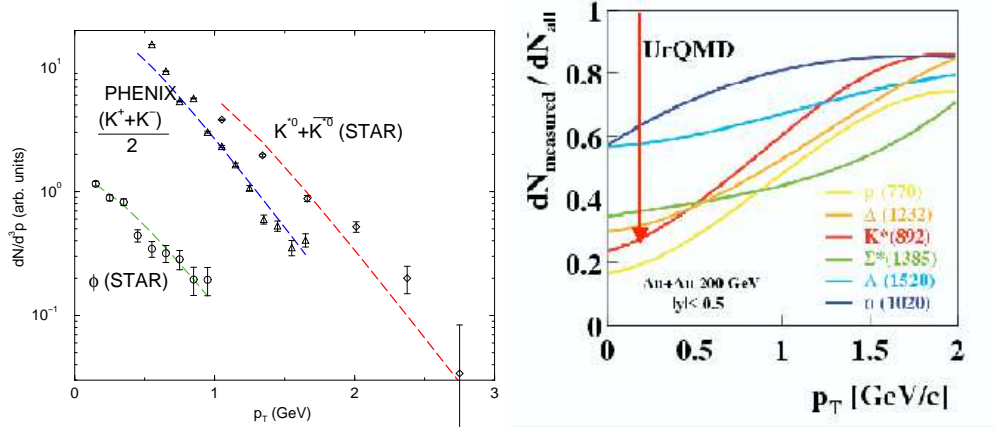


Figure 4.8: (color online)(left) K^* , K^- and ϕ normalized spectra within the global fit using non-equilibrium sudden freeze-out (Fig. 4.6, black). (right) momentum dependence of K^* suppression through rescattering of decay products, calculated in the microscopic hadronic model uRQMD .

(Bleicher and Stocker 2004). Given this, the relative goodness of the fit to K^* data is a strong boost for the sudden freeze-out picture.

The acceptable K^* description within a fit which includes K^+ and K^- is encouraging for another reason: Resonances and absolute normalization in fits with many particles remove the correlation between temperature and flow: It is not possible to adjust the slopes by shifting the temperature and transverse flow along the same contour, since in this case normalization is also affected. However, temperature is still strongly correlated with chemical potentials (especially γ_s and γ_q). However, if the fit includes K^* s and K s, this correlation is removed, since both spectra share a common chemical potential. Shifting the temperature from the minimum will result in a shift of one of these spectra away from the data, no matter what chemical potential is used. For this reason, a common tempeature

minimum in a fit which includes K^* and K_S is an important test the sudden freeze-out model successfully passed. We hope further tests, in the form of more resonance spectra, are forthcoming.

In conclusion, we have given an overview of different hadronization models, and described how they arise from different freeze-out scenarios of a system forming from a thermalized quark gluon plasma. We have also shown, in the boost invariant limit, how the various hadronization ansatzes give rise to quantitative differences in observed particle spectra. We have then used MonteCarlo simulated data to study the sensitivity to model choice of presently available experimental data, and have evaluated different models ability to fit presently existing RHIC data. While data slightly favors a chemical non-equilibrium explosive freeze-out, there is not enough evidence to make a definitive conclusion about this issue. We hope the forthcoming 200 GeV results will clarify this further.

CHAPTER 5

Direct detection of short-lived resonances

5.0.1 Introduction and motivation

The experimental measurement of short-lived hadron resonances can potentially be very useful in clarifying some of the least understood aspects of heavy ion collisions. In general, evolution of a hot hadronic system proceeds according to Fig. 5.1. When mesons and baryons emerge from a pre-hadronic state, presumably quark gluon plasma, their abundances are expected to be fixed by hadronization temperature and chemical fugacities. This stage of fireball evolution is commonly known as chemical freeze-out. After initial hadronization, the system may evolve as an interacting hadron gas. At a certain point (which can vary according to particle species), thermal freeze-out, where hadrons stop interacting, is reached.

A quantitative understanding of the above picture is crucial for any meaningful analysis of the final state particles. Many probes of deconfinement are most sensitive when the dense hadron matter fireball breakup is sudden and re-interaction time short or non-existent. Final state particles could, however also emerge remembering relatively little about their primordial source, having been subject to re-scattering in purely hadronic gas phase. In fact, theoretical arguments have been advanced in support of both a sudden reaction picture (Csorgo and Csernai 1994; Rafelski and Letessier 2000) and a long re-interaction timescale (Braun-Munzinger

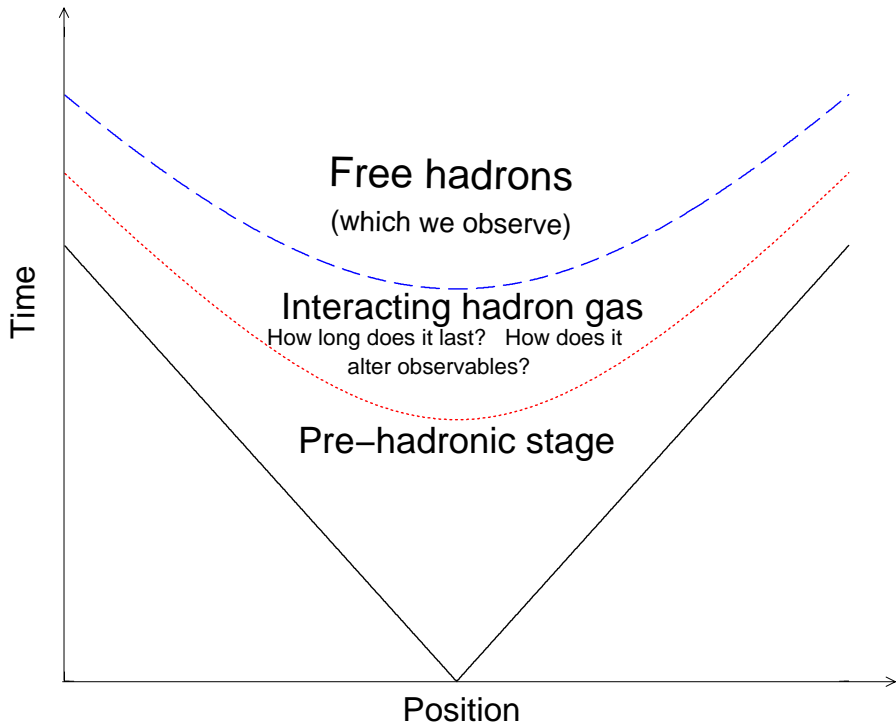


Figure 5.1: Stages of the space-time evolution of a heavy ion collision. At a certain moment in proper time (known as chemical freeze-out), hadrons emerge. The system then evolves as an interacting hadron gas, until thermal freeze-out, the point at which all elastic interactions cease.

et al. 1999; Heinz and Jacob 2000). Both pictures have been applied to phenomenological fits of hyperon abundances and distributions (Akkelin et al. 2002; Arbex et al. 2002; Torrieri and Rafelski 2001a).

It is apparent that hyperon resonances can be crucial in resolving this ambiguity: their initial abundance, compared to stable particles with the same quark composition, depends primarily to the temperature at hadron formation. However, the observed abundance will be potentially quite different, and will strongly depend on the lifetime of the interacting hadron gas phase. Resonances can only be observed via invariant mass reconstruction, and their short lifetime means that they

can decay within the interacting hadron gas (Fig. 5.2). In this case, the decay products can undergo re-scattering, and emerge from the fireball with no memory about the parent resonance. Thus, the observable resonance abundance is sensitive to precisely those parameters needed to distinguish between the sudden and gradual freeze-out models.

In this chapter, we start with a review of presently available experimental data, and the open questions which arise. We then proceed to describe how to calculate the initial resonance abundance and the effect of re-scattering in terms of the hadronization temperature and the lifetime of the interacting hadron gas. We show how these two parameters can be extracted from the experimental observations. Finally, we discuss possible answers to experimental challenges raised in the first section, and suggest ways by which these questions could be resolved by further measurements. Most of this write-up is based on recently published experimental measurements (Friese 2002; Fachini 2002; Adler et al. 2002b; Markert et al. 2002a; Afanasev et al. 2002; Zhang 2004; Salur 2004) and theoretical papers (Torrieri and Rafelski 2002; Rafelski et al. 2001; Torrieri and Rafelski 2001b)

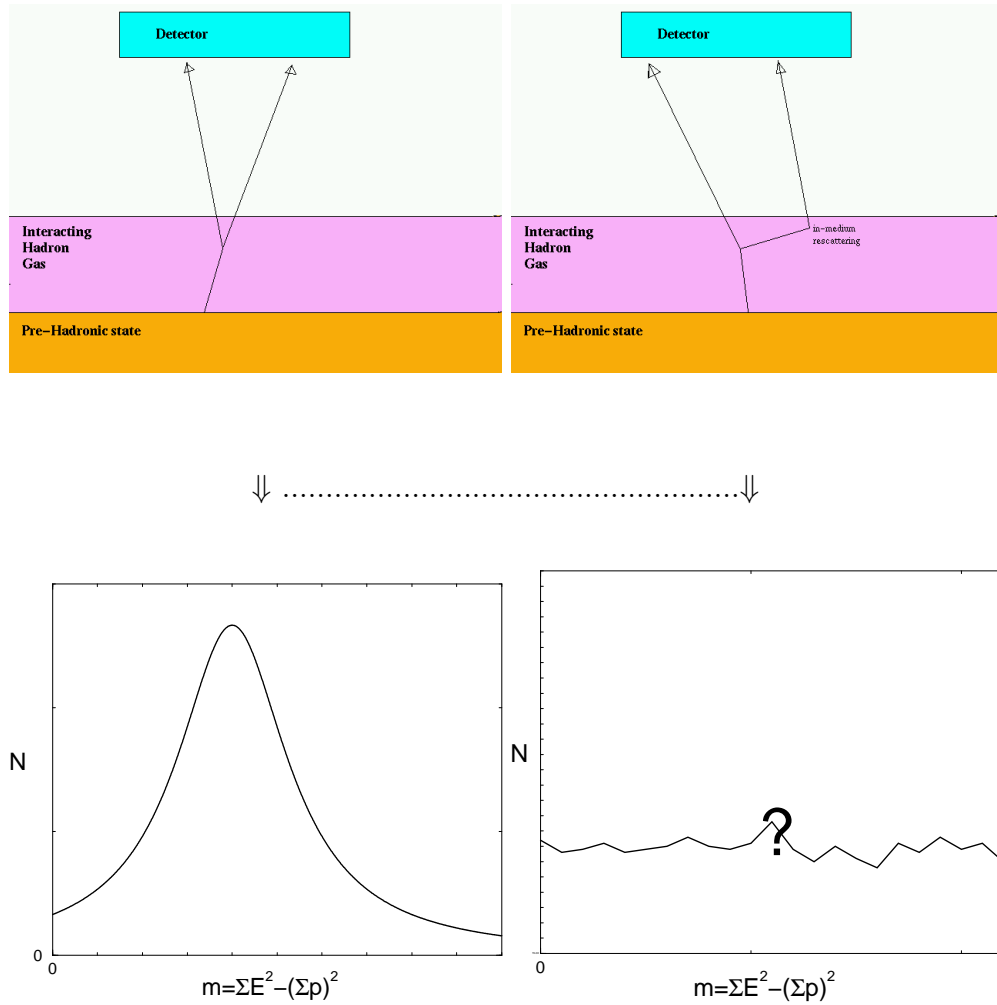


Figure 5.2: How re-scattering can inhibit resonance reconstruction. If the resonance decay products reach the detector without further interactions, their invariant mass distribution should yield a clear peak at the resonance mass. However, if these decay products undergo re-scattering before reaching the detector, the signal may be indistinguishable from the background caused by unrelated particle pairs.

5.1 Can short-lived resonances be explained by a statistical model?

Since its beginning, the RHIC heavy ion program, and in particular the STAR collaboration, has managed to measure an impressive amount of resonance data.

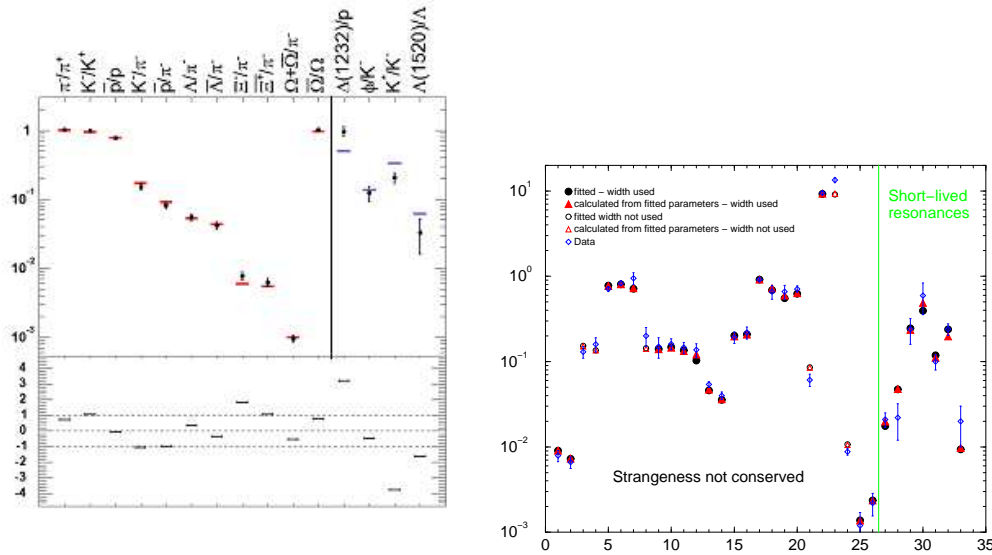


Figure 5.3: (Color on-line) Fits to particle ratios containing several short-lived resonances, using an equilibrium (left) and a non-equilibrium (right) formalism. The fit in (right), was obtained using the SHARE program (See Appendix D).

In addition to the K^* and the $\Lambda(1520)$, the ρ , $f_0(980)$, Δ , Ξ^* and Σ^* have been measured in p-p, and sometimes Au-Au (Fachini 2004; Zhang 2004). Further results in Au-Au collisions are expected soon. Including these particles in a global fit, of the type described in section 2.2.1 places a tight constraint on the temperature, since many of the resonances have the same chemical composition but a different mass from observed “light” particles. Fig. 5.3 shows what happens when such a fit is done. A chemical equilibrium model (Braun-Munzinger et al. 2001) fails to describe short-lived resonances. Under chemical non-equilibrium, however (Fig. 5.3 right), both short-lived and long-lived resonances are described with equal acceptability. In a sense, the proponents of both a long freeze-out stage (which would pull short-lived resonances out of equilibrium) and sudden freeze-out can be satisfied by this result: Proponents of hadronization at $T=170$ MeV can rely on the hypothesis that in-medium interactions will make short-lived resonances unobservable, while

the short-lived data points are well described by the non-equilibrium model, at the same temperature and $\gamma_{q,s}$ as found in earlier fits (Rafelski and Letessier 2003b). We can try to see which of the pictures is right by concentrating on a few particularly simple resonances, and attempting to quantify the effect of a post-hadronization hadron gas phase. This topic will be addressed in the next section.

5.2 Modeling resonances in heavy ion collisions

5.2.1 Direct production at hadronization

We assume that at hadronization, a volume element will be at thermal and chemical equilibrium in its local rest frame. As shown in section 2.2.1, this means that details of flow and freeze-out hypersurface cancel out when the global (4π) ratio, or a mid-rapidity ratio in a Bjorken-type fireball, are considered.

In the Boltzmann approximation (applicable here since $\lambda_{particle} \sim O(1)$ and $m \gg T$), the chemical potential will then cancel out when two particles of the same quark composition are compared. The ratio of the heavier resonance $N^* \rightarrow N\pi$ to the lighter resonance N will then be given by Eq. (2.24))

$$\frac{N^*}{N} = \frac{g^* m^{*2} K_2 \left(\frac{m^*}{T} \right)}{g^* m^{*2} K_2 \left(\frac{m^*}{T} \right) + g m^2 K_2 \left(\frac{m}{T} \right)} \quad (5.1)$$

(Here g is the statistical degeneracy). Ratios where the Boltzmann approximation is applicable and feed-down from particles of different quark constituents is small include Σ^*/Λ and $\Lambda(1520)/\Lambda$. K^{*0}/K^+ and $\overline{K^{*0}}/K^-$ has a larger correction due to $\phi \rightarrow KK^1$, while in other, recently measured ratios ($\Delta/p, \rho/\pi$ (Zhang 2004)) the

¹Of course, the K^{*0}/K^- ratio can be corrected for $\phi \rightarrow K^+K^-$ feed-down, since the NA49 and STAR experiments have published yields for both. We recommend that such a correction

feed-down from particles with a different chemical potential is simply too large to be neglected.

If less than 4π acceptance is observed, we can obtain the equivalent of Eq. (5.1) by integrating Eq. (3.4) and Eq. (4.11) across a finite $y - p_T$ range. As will be shown, the finite acceptance effects will cancel out to a very good approximation if particles of a comparable mass are considered. Hence, Eq. (5.1) can still be used for ratios with a finite acceptance detector.

Table 5.1 summarizes the decay processes considered in our analysis and their parameters (Clebsh-Gordon coefficients have been used to estimate decays such as $(N^{*0} \rightarrow N^+ \pi^-)/(N^{*0} \rightarrow N^0 \pi^0)$).

Table 5.1: Resonances contributing to Λ and K production, with their degeneracies, rest-frame momentum (p^*) and possibility for experimental reconstruction.

g	Reaction	p^*	branching	visible?
≈ 4	$\Sigma^{*0}(1385) \rightarrow \Sigma^0 \pi^0$	127	$\approx 4\%$	No
8	$\Sigma^{*\pm}(1385) \rightarrow \Lambda \pi^\pm$	208	88%	Yes
4	$\Sigma^{*0}(1385) \rightarrow \Lambda \pi^0$	208	88%	No
2	$\Sigma^0 \rightarrow \Lambda \gamma$	74	100%	No
4	$\Lambda(1520) \rightarrow N \bar{K}$	244	45%	Yes
3	$K^{*0}(892) \rightarrow K^+ \pi^-$	291	67%	Yes

In Fig. 5.4 we show the relative thermal production ratios at chemical freeze-out over the entire spectrum of rapidity and m_T (solid lines) and central rapidity range (dashed lines). The sensitivity of resonance yields to hadronization temperature is apparent for all resonances under consideration. In particular, the Σ^* emerges as a very promising candidate for further study. For example, at the lowest be done when presenting future K^* results, as their interpretation becomes considerably more model-independent.

current estimates ($T \simeq 100$ MeV) of the final break up temperature in $158A$ GeV SPS collisions 33% of Λ s are actually primary Σ^* s, the percentage rises to slightly more than 50% if chemical freeze-out occurs at $T = 190$ MeV. For all of these cases, the Σ^* primary yield should be considerably bigger than the Ξ (if the chemical potentials in (Rafelski and Letessier 2003b) are used for the prediction), and the angle between the decay products should be about the same as in the $\Omega \rightarrow \Lambda K$ decay. The NA49 detector in the SPS and the STAR detector at RHIC are both capable to measure hyperon and resonance yields well within the precision required to make a good measurement of the hadronization temperature.

We also note that while the experimentally observed K^* yield is compatible with the produced ratio in the case of non-equilibrium hadronization (Rafelski and Letessier 2003b), the $\Lambda(1520)$ seems very suppressed. To discuss this further, however, an estimation of the effect of re-scattering on resonance abundances is necessary.

5.3 Rescattering

As explained in the introduction, direct observation of resonances relies on invariant mass reconstruction. Therefore, to calculate the observed resonance abundances, rescattering after hadronization will have to be taken into account. This can be looked at within a microscopic model of hadronic matter such as uRQMD. Here, we present such a study using a “back of the envelope” model which nevertheless seems to provide an acceptable quantitative description of how the propagation of resonances and their decay products through opaque matter deviates from an equilibrium prediction.

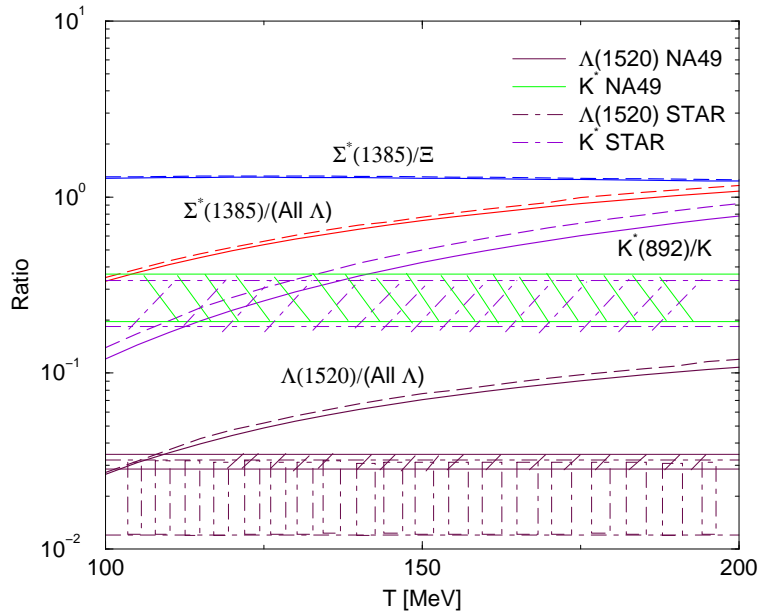


Figure 5.4: Temperature dependence of ratios of Σ^* , K^{*0} and $\Lambda(1520)$ to the total number of observed K , Λ s and Ξ s. Branching ratios are included. Dashed lines show the result for a measurement at central rapidity $\Delta y = \pm 0.5$. The experimental measurements included in the diagram are discussed in the first part of this paper. It should be noted that the K^*/K ratio is actually $\overline{K^*}/K^-$ for the NA49 measurement, and an average $(K^* + \overline{K^*})/(K^+ + K^-)$ for STAR.

We first note in Fig. 5.4, that the relative Σ^*/Ξ signal is remarkably independent (within 5 %) of Temperature. This is because the $\Xi^*(1530)$ contribution cancels nearly exactly the thermal suppression of the Ξ originating in the $\Xi - \Sigma^*$ mass difference. This effect could be used for a direct estimate of the Σ^* lost through rescattering, even without knowledge of the freeze-out temperature, should the chemical parameters (λ_i and γ_i) be independently known (They can be obtained from a fit of the stable particle ratios). A simple test of sudden hadronization model consists in measurement of the ratio Σ^*/Ξ . If it is significantly smaller than unity, we should expect a re-equilibration mechanism to be present. Otherwise sudden hadronization probably applies, since Σ^* emerge from chemical freeze-out without undergoing interactions.

We can, however, go further and use the suppression of the considered

resonances as a tool capable of estimating conditions at particle freeze-out. We consider the decay of a generic resonance N^*

$$N^* \rightarrow Y\pi, \quad (5.2)$$

in a gas of pions and nucleons. We shall assume that one interaction of either Y or π is sufficient for that resonance to be undetectable, and that the decay products travel through the medium with speed v_i (where i can mean either Y or π). The interaction probability is proportional to v_i , the interaction cross-section of the decay product with each particle in the hadronic medium ($\sigma_{ij}(v_i)$, where j can refer to either pions, Kaons, nucleons or antinucleons. Note that the cross-section itself depends, in a generally complicated way, on the incident momentum, and hence on v_i), and the particle density in the fireball ρ_j . ρ_j is increased by a factor $\gamma_i = 1/\sqrt{1 - v_i^2}$ due to Lorentz-contraction, and decreases as time passes because of the fireball's collective expansion (parametrized by the flow velocity v_{flow} , assumed to be of the order of the relativistic sound speed $c/\sqrt{3}$.) The time dependence of the densities will therefore be

$$\rho_j(t) = \gamma_i \rho_{0j} \left(\frac{R}{R + v_{\text{flow}} t} \right)^3, \quad (5.3)$$

and ρ_{0j} , the density of j at hadronization, can be calculated from the chemical freezeout temperatures and chemical potentials. Putting everything together, the rescattering reaction rate is

$$P_i = \sum_{v_i} [\sigma_{i\pi}(v_i) \rho_{0\pi} + \sigma_{iK}(v_i) \rho_{0K} + \sigma_{iN}(v_i) \rho_{0N} + \sigma_{i\bar{N}}(v_i) \rho_{0\bar{N}}] (\gamma v)_i \left(\frac{R}{R + v_{\text{flow}} t} \right)^3, \quad (5.4)$$

If we use the average,

$$\sum_{v_i} \sigma(v_i) v_i \gamma_i \simeq \langle \sigma \rangle \langle \gamma_i v_i \rangle = \langle \sigma \rangle \frac{p_i}{m_i}, \quad (5.5)$$

(where p and m are the resonance's momentum and mass) eq. (5.4) becomes,

$$P_i = [\langle \sigma_{i\pi} \rangle \rho_{0\pi} + \langle \sigma_{iK} \rangle \rho_{0K} + \langle \sigma_{iN} \rangle \rho_{0N} + \langle \sigma_{i\bar{N}} \rangle \rho_{0\bar{N}}] \frac{p_i}{m_i} \left(\frac{R}{R + v_{\text{flow}} t} \right)^3, \quad (5.6)$$

Neglecting in-medium resonance regeneration and particle escape from the fireball, the population equation describing the scattering loss abundance (N_i) is:

$$\frac{dN_i}{dt} = \frac{1}{\tau} N_{N^*} - N_i P_i, \quad i = 1, 2 \quad (5.7)$$

$$\frac{dN_{N^*}}{dt} = -\frac{1}{\tau} N_{N^*} \quad (5.8)$$

The required nucleon and antinucleon density ρ_N is obtained through Eq. (??)

$$\rho_{0N} = \frac{g}{(2\pi\hbar c)^3} 4\pi m^2 (\lambda_q \gamma_q)^3 T K_2\left(\frac{m}{T}\right), \quad (5.9)$$

We consider the nucleons to have a mass of $\simeq 1$ GeV, and a degeneracy of 6, to take the p,n and the thermally suppressed but higher degeneracy Δ contributions into account. the pion density is computed in the massless particle limit, leading to

$$\rho_{0\pi} = \sum \frac{3g}{(2\pi\hbar c)^3} 4\pi m_\pi^2 \gamma_q^{2(n+1)} \frac{T}{n} K_2\left(\frac{nm}{T}\right) \quad (5.10)$$

The model presented here is remarkably insensitive to the individual cross-sectional areas. The values we used in the calculation are given in table 5.2, but order-of-magnitude variations of the more uncertain cross-sections did not produce variations of more than 30%. Similarly, the value of the initial fireball radius R_0 (which is constrained by the entropy per baryon) does not significantly affect the final ratios. This reassures us that had we used a more exact approach than the approximations in Eq. (5.5), the qualitative features of our model would not have changed. The results, however, exhibit a very strong dependence on both the Temperature (which fixes the initial resonance yield as well as the hadron density of the fireball) and fireball lifetime (in a short-lived fireball not many resonances decay, so

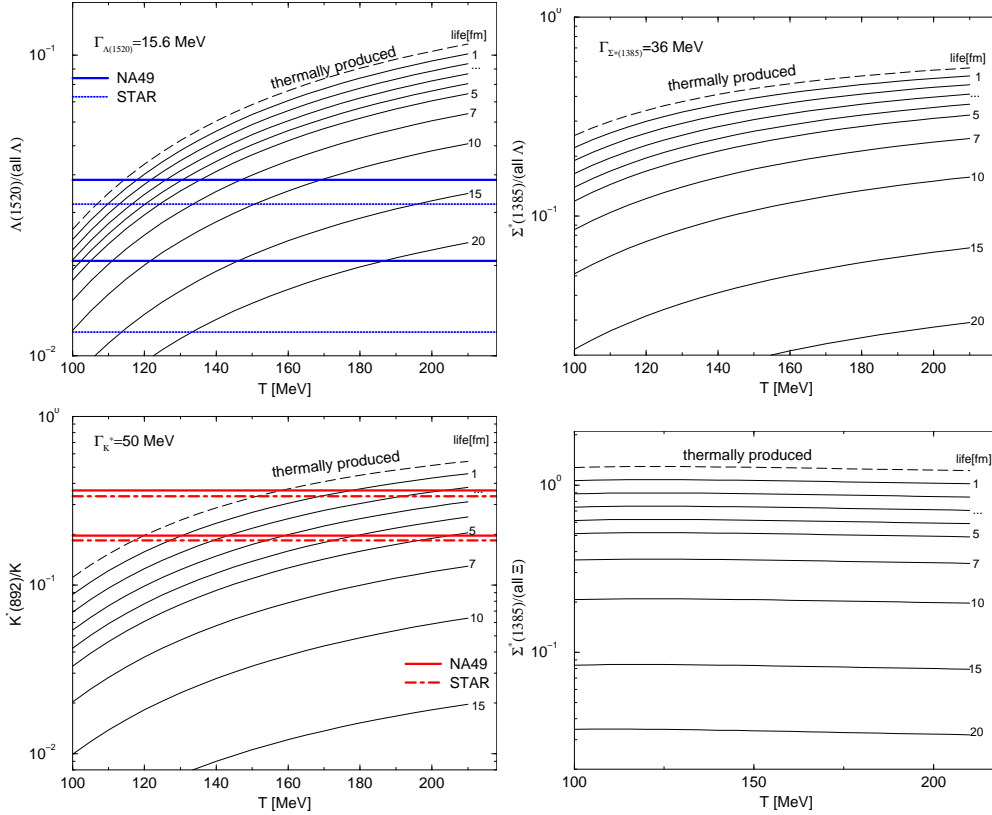


Figure 5.5: Produced (dashed line) and observable (solid lines) ratios $\Lambda(1520)/(total \Lambda)$, $\Sigma^*/(total \Lambda)$, K^{*0}/K and $\Xi/(total \Lambda)$. The solid lines correspond to evolution after chemical freeze-out of 1,2,3,4,5,7,10,15,20 fm/c, respectively. The values at time zero (chemical freezeout) were taken from Fig. 5.4. See Fig. 5.4 caption for the meaning of K, K^* .

their products do not get a chance to rescatter). Fig. 5.5 shows the dependence of the $\Lambda(1520)/\Lambda$, Σ^*/Λ and $K^{*0}(892)/K$ on the temperature and lifetime of the interacting phase. It is clear that, given a determination of the respective signals to a reasonable precision, a qualitative distinction between the high temperature chemical freeze-out scenario followed by a rescattering phase and the low temperature sudden hadronization scenario can be made. We also note that despite the shorter lifetime of the Σ^* and higher pion interaction cross section, more Σ^* decay

products should be reconstructible than in the $\Lambda(1520)$ case, at all but the highest temperatures under consideration. This reinforces our proposal that the Σ^* is a very good candidate for further measurement.

Diagrams such as those in Fig. 5.5 still contain an ambiguity between temperature and lifetime of the interacting hadron gas phase. A low observed ratio can either mean a low freeze-out temperature or a lot of rescattering in a long re-interaction phase. However, this ambiguity can be resolved by looking at a selection of resonances, with different masses and lifetimes. Fig. 5.6 shows how the initial temperature and the lifetime of the re-interaction phase decouple when two resonance ratios are measured simultaneously. A data point on diagrams such as those in Fig. 5.6 is enough to measure both the hadronization temperature and to distinguish between the sudden freeze-out scenario and a long re-interaction phase.

The plots in Fig. 5.6 can also be used as consistency checks for the model: For example, the near independence of Σ^*/Ξ on temperature means that the equal temperature lines in the Σ^*/Ξ vs Σ^*/Λ diagram are nearly insensitive to the details of the rescattering model. Moreover the mass differences and lifetimes of the Σ^* , K^* combine in such a way as to make the $\Sigma^*/(\text{all } \Lambda)$ vs $K^{*0}(892)/(\text{all } K^-)$ diagram fold into a very narrow band. Any serious shortcoming within our rescattering model would be revealed if the observed particle ratios stray from this band.

To understand the low $\Lambda(1520)$ multiplicity measured by NA49 and STAR it should be realized that the $\Lambda(1520)$ is a very unusual particle (Watson et al. 1963). Unlike most other hadronic resonances (Σ^* , K^* , Δ , ρ ecc.), its high spin is due not to valence quark spin configuration but to the fact that the $\Lambda(1520)$ s valence quarks are (using the constituent quark picture) in an $L = 1^-$ state. The dominant decay

Table 5.2: Scattering model parameters

$\sigma_{\pi N}$ (mb)	σ_{KN}	$\sigma_{\pi\pi}$	$\sigma_{\pi K}$	σ_{NN}	$\sigma_{\bar{N}N}$
24	20	40	20	24	50
Γ_{Σ^*}	$\Gamma_{\Lambda(1520)}$			$\Gamma_{K^{*0}(892)}$	
35 MeV		15.6 MeV		50 MeV	
escape rate (fm $^{-3}$)			negligible		
v				0.5	
R(fm)				8 145/T [MeV]	
μ_b				220 MeV	

(N K), however, has to go through a relative momentum L=2 (d-wave) process, through a channel which is very close to threshold production. All this conspires to reduce the $\Lambda(1520)$'s width: Isospin conservation reduces the number of channels it can decay (most notably $\Lambda(1520) \rightarrow \Lambda\pi$ is not allowed), while the high relative angular momentum (and negative space parity) and threshold suppress the decay phase space for both the dominant (NK) and additional ($\Sigma\pi, \Lambda\pi\pi$) $\Lambda(1520)$ decay modes.

Therefore, measurement of the $\Lambda(1520)$ presents both experimental challenges (The high partial wave component introduces an angular/spin dependence of the decay products which is difficult to measure in an unpolarized high multiplicity experiment) and theoretical uncertainties (perhaps new in-medium physics is at work in $L \neq 0$ resonances (Markert et al. 2002b; Zimanyi and Levai 2004)). It should be noticed that, as Fig. 5.7 shows, a 50% suppression of the $\Lambda(1520)$ signal at hadronization would mean the data is perfectly compatible with the sudden freeze-out model described in (Rafelski and Letessier 2000). This strongly suggests that other resonances should be used to constrain the fireball freeze-out properties.

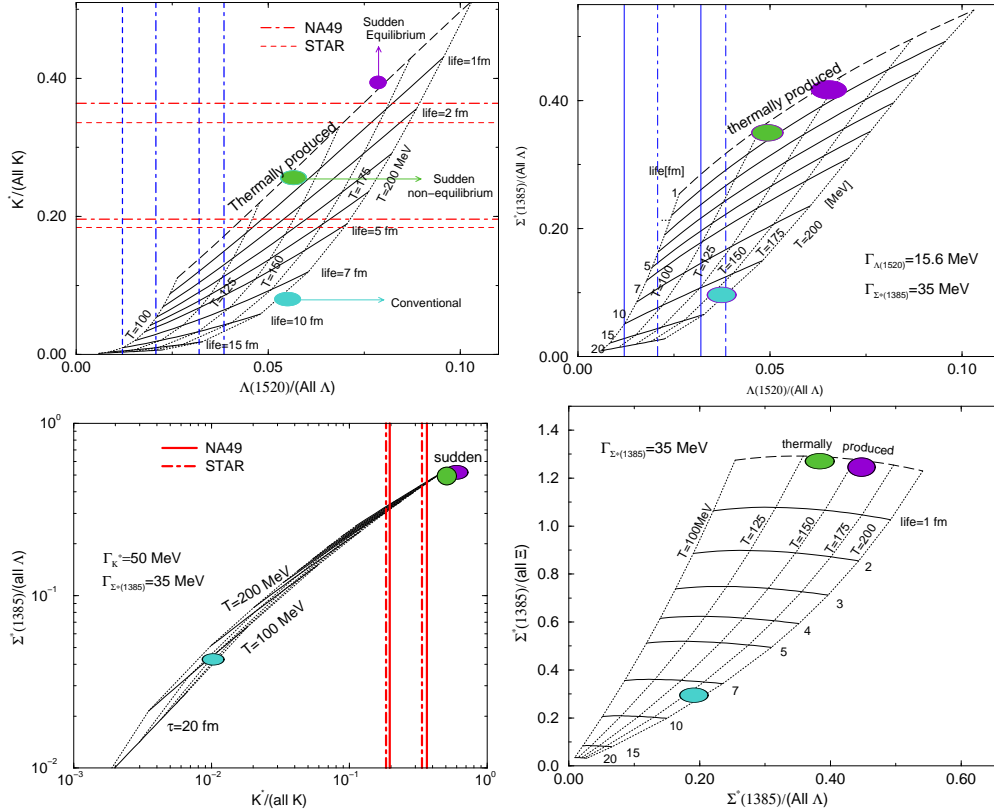


Figure 5.6: How temperature and fireball lifetime decouple when two resonances of different masses and widths are compared. A point on any of the above diagrams is potentially sufficient to fix both of these quantities. The experimental measurements are discussed in the first section. See Fig. 5.4 caption for the meaning of K, K^* .

The non-suppression of the K^* makes it likely that other hadron resonances can also be detectable. The diagrams shown in the previous section make it clear that the Σ^* should be abundantly produced, and it has many characteristics which would make it a logical next step in the study of resonances produced in heavy ion collisions. Ξ^*/Ξ will also be a candidate for this kind of study.

Focusing on these resonances will also make regeneration less likely. In particular, regeneration is less likely to affect the Σ^* detectability: 95% of Σ^* decay

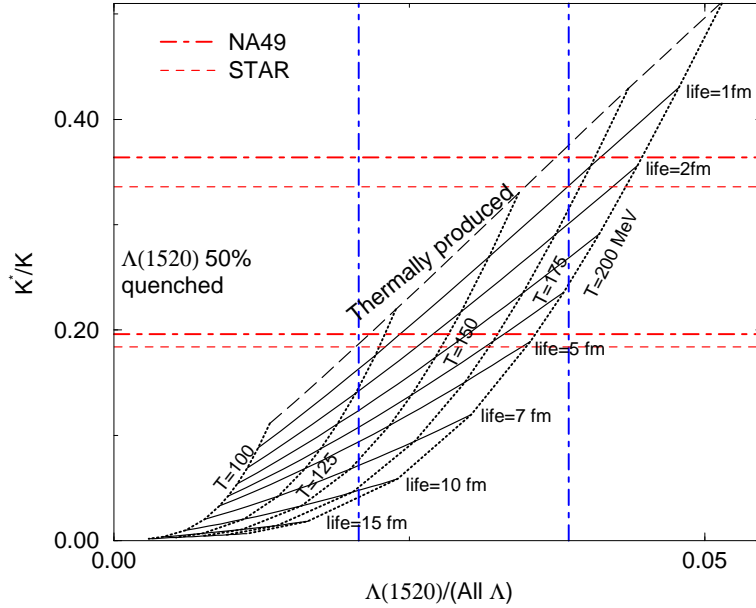


Figure 5.7: K^*/K vs $\Lambda(1520)/\Lambda$ assuming half of the $\Lambda(1520)$ s are suppressed in-medium. See Fig. 5.4 caption for the meaning of K, K^* .

through the p -wave $\Sigma^* \rightarrow \Lambda\pi$ channel. However, regenerating Σ^* s in a gas of Λ s and π s is considerably more difficult, since $\Lambda\pi$ scattering will be dominated by the s -wave $\Lambda\pi \rightarrow \Sigma^\pm$. For these reasons, a measurement of the Σ^*/Λ and Ξ^*/Ξ (which is also unlikely to regenerate due to its small width) should be able to distinguish a sudden hadronization model from a slow sequential freeze-out with certainty.

5.4 Production of pentaquarks

The discovery by the NA49 collaboration (Alt et al. 2004) of a new $\Xi^{--}(1862)$ $I = 3/2$ narrow $\Gamma < 5$ MeV resonance in their pp background, ($\sqrt{s_{NN}} = 17.2$ GeV) demonstrates that heavy ion detectors are capable of discovering states missed at previous energy scans. Statistical hadronization and strangeness enhancement

mean that these states should be produced abundantly in heavy ion collisions. The enhanced production rate, together with experimental capabilities, makes the Heavy ion experiments promising probes for the discovery of new hadronic states.

This newly discovered hadron resonance has, given the mass and charge, an exceedingly narrow width. This feature is common with $\Theta^+(1540)$, another recently reported resonance (Nakano et al. 2003; Barmin et al. 2003; Stepanyan et al. 2003), which decays into the channel with quark content $uudd\bar{s}$ and $I = 0$. This is believed to be the predicted (Diakonov et al. 1997), lowest mass, pentaquark state. The $\Xi^*(1862)$ can be interpreted as its most massive isospin quartet member $ssdd\bar{u}$, $ssud\bar{u}$, $ssu\bar{d}\bar{d}$, $ssu\bar{u}\bar{d}$ with electrical charge varying, respectively, from -2 to $+1$, in units of $|e|$.

Appearance of these new resonances can have many consequences in the field of heavy ion collisions. We at first explore how the introduction into the family of hadronic particles of these two new resonances, $\Theta^+(1540)$ and $\Xi^*(1862)$, influence the results of statistical hadronization fit to relativistic heavy ion hadron production experimental results. We use the same data set as has been employed in Ref (Rafelski and Letessier 2003b) and obtain predictions of how the relative abundances of these new resonant states vary as function of the heavy ion collision energy.

Importantly, only the two already identified states with $I = 0$, and $I = 3/2$ of the anti decuplet, which also includes the $I = 1/2$, and $I = 1$ states are of relevance in the study of the statistical hadronization fits. Thus, in our analysis, we do not depend on the unknown masses of $I = 1/2$, and $I = 1$ states. However, the interpretation of the newly discovered narrow states as pentaquarks enters our

considerations decisively. In our approach (Rafelski and Letessier 2003b), as in other recent work (Becattini et al. 2003), the chemical equilibrium and non-equilibrium is considered. Accordingly, we allow quark pair phase space occupancies, for light quarks $\gamma_q \neq 1$, and/or strange quarks $\gamma_s \neq 1$.

The pentaquark (if this is indeed a pentaquark) valance quark content enters the assigned chemical fugacities and phase space occupancies in a different way than either mesons or baryons. Hence, predictions for the pentaquark yield are likely to be very different whether equilibrium is assumed or not. In particular, if the phase space is saturated above equilibrium, this will yield to a large ($\sim \gamma^3$) enhancement of pentaquarks with respect to hadrons of a similar mass. And nature has been generous enough to provide us with detectable hadrons of a comparable mass and width: The $\Lambda(1520)$ and $\Xi(1530)$, with mass and width nearly identical to Θ^+ .

Since we study at SPS the total particle multiplicities, and at RHIC the central yields which can be considered produced by rapidity-localized fireballs of matter, we require in our fits balance in the strange and antistrange quark content.

There are two independent fit parameters when we assume complete chemical equilibrium, the chemical freeze-out temperature T and the light quark fugacity $\lambda_q = \sqrt{\lambda_u \lambda_d} = e^{\mu_b/(3T)}$. The baryochemical potential μ_b is the physical parameter controlling baryon density. Strangeness conservation fixes the strange quark fugacity λ_s (equivalently, strangeness chemical potential, for more details see, e.g., (Rafelski and Letessier 2003b)). Adding the possibility that the number of strange quark pairs is not in chemical equilibrium, $\gamma_s \neq 1$, we have 3 parameters, and allowing also that light quark pair number is not in chemical equilibrium, we have 4

parameters. These three alternatives will be coded as open triangles, open squares and filled squares, respectively, in all results we present graphically.

We find that the new resonance $\Theta^+(1540)$ influences significantly the statistical hadronization fit to particle production at the lowest SPS energies. In a baryon rich environment the introduction into the fit of $\Theta^+(1540)$, a $b = 1$ baryon with ‘wrong’ strangeness influences the strangeness balance condition, and thus indirectly the individual yields of all strange hadrons. This leads to a reduction in the statistical fit error for our hadronization study of the $40A$ GeV Pb–Pb reactions where we see a significant change in the relative yield of kaons and Λ . We also find changes in the details of the statistical fit parameters. In comparison to (Rafelski and Letessier 2003c), aside of the introduction of the new resonances, we also have harmonized our hadron decay table with those used by the Kraków group (Baran et al. 2004). The improvement of the particle yield fit is both, a theoretical confirmation of the validity of the statistical hadronization model of particle production, and its applicability at low SPS energies. We show how the fit error evolves in Fig. 5.8, which is also presented in the bottom lines of tables 2.1 and 2.2 along with the number of data points and resulting degrees of freedom. Considering the small number of degrees of freedom at SPS, we need $\chi^2/\text{dof} < 1$ to have good significance of the fit². The errors seen in Fig. 5.8 are, for the chemical nonequilibrium case (filled squares), sufficiently small to allow us to conclude that the introduction of $\Theta^+(1540)$ assures that the statistical hadronization works well down to the lowest SPS energies. To compare with earlier results on χ^2/dof , obtained prior to the discovery of these new resonances, see Ref. (Rafelski and Letessier 2003c), figure 16.

²See appendix B

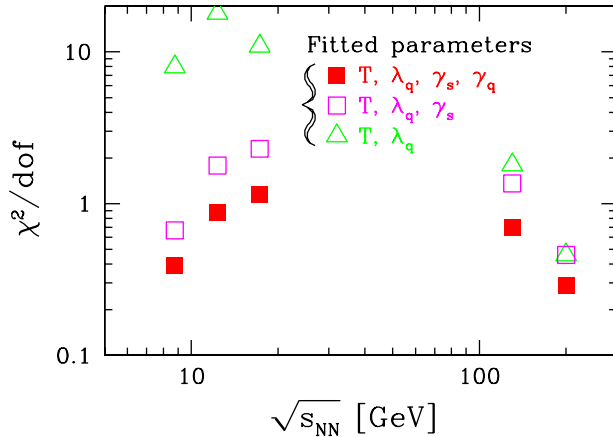


Figure 5.8: (Color online) χ^2/dof for statistical hadronization fits at SPS and RHIC: results are shown for 40, 80, 158A GeV Pb on stationary Pb target collisions and at RHIC for 65+65 and 100+100A GeV Au–Au head on interactions.

An interesting point, seen in Fig. 5.8, is that the chemical equilibrium fit $\gamma_s = 1, \gamma_q = 1$ is rendered unacceptable at all SPS energies in presence of the new resonances. The semi-equilibrium fit, which allows a varying strangeness saturation, but assumes light quark equilibrium is generally resulting in twice as large χ^2 compared to the full non-equilibrium approach. In a study of χ^2 profile as function of γ_q we find a clear and strong minimum for $\gamma_q \rightarrow \gamma_q^{\max} \equiv e^{m\pi/(2T)}$. Acquisition by the fit of this limiting value implies that there is no fitting error in the γ_q presented below.

The chemical freeze-out parameters of the fits considered play a very important role in predicting the (relative) yield of hadronic particles, and this dependence is even stronger for many pentaquark states, due to their unusual quantum numbers. These fit parameters for RHIC are shown in table 2.2, and for SPS in table 2.1 along with the freeze-out temperature. We note that for the full chemical

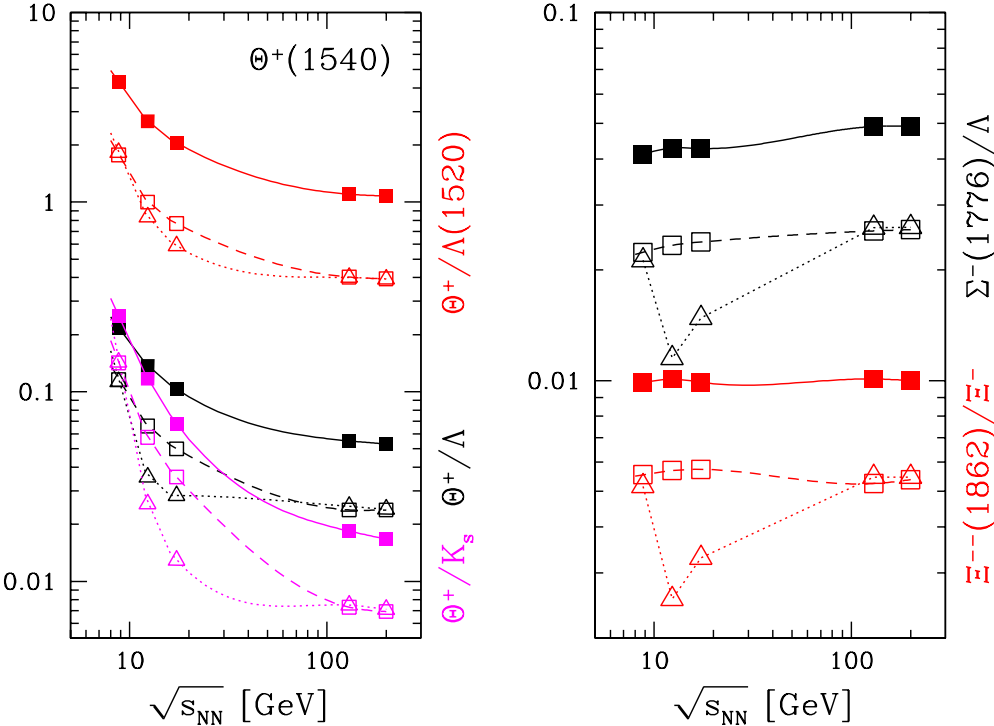


Figure 5.9: (Color online) Yield of $\Theta^+(1540)$ in relativistic heavy ion collisions, based on statistical hadronization fit to hadronization parameters at SPS and RHIC 40, 80, 158A GeV Pb on stationary Pb target collisions and at RHIC for 65+65 and 100+100A GeV Au–Au head on interactions. Relative yields with K_s , Λ , and $\Lambda(1520)$ are shown from bottom to top.

non-equilibrium, the freeze-out temperature is found to be smaller than for semi-equilibrium case. This reduction is over-compensated in pentaquark yields by the significantly increased value of γ_q .

We now consider the relative yields of the new resonances in figures 5.9 (left) and 5.9 (right). These yields vary strongly with collision energy for the case of $\Theta^+(1540)$ in Fig. 5.9 (left), but are rather constant in Fig. 5.9 (right). Certainly our result differs greatly from expectations arising from an earlier study of the statistical model production of the $\Theta^+(1540)$ resonance (Randrup 2003) where the decisive variation of the particle yield with chemical potentials was not explored.

Moreover, the hadron yields, presented in (Randrup 2003), did not include the contributions from decay of short lived hadron resonances. We checked that the relative particle yields shown in (Randrup 2003) for zero chemical potentials and varying temperature are mathematically correct, also as a cross check of our program.

In Fig. 5.9 (left), we show (from top to bottom) the relative yields $\Theta^+(1540)/\Lambda(1520)$, $\Theta^+(1540)/\Lambda$, $\Theta^+(1540)/K_s$ for chemical nonequilibrium (solid lines), semi-equilibrium ($\gamma_q = 1$, dashed lines) and chemical equilibrium (dotted lines). The yields of Λ used here include 50% weak interaction cascade from Ξ .

The reason that the chemical nonequilibrium is leading to greater than equilibrium yields is that the lower hadronization temperature is overcompensated by the chemical factors, e.g., $\Theta^+(1540)/\Lambda(1520) \simeq 1/2 \gamma_q^2 (\lambda_q/\lambda_s)^2$ ignoring the small mass difference. The factor 1/2 is due to the difference in spin degeneracy. The actually observed yield ratio $\Theta^+(1540)/\Lambda(1520)$ is probably going to be still greater: As explained in the previous section, $\Lambda(1520)$ is seen at 50% of the expected statistical hadronization yield in heavy ion collisions. As the $\Theta^+(1540)$ is an L=0 resonance, we predict that its yield should more closely match the statistical model calculation.

In Fig. 5.9 (left), we also recognize that the reason that there is such a significant impact at low SPS energies of $\Theta^+(1540)$ is that it is produced at the level of +10–20% of Λ in fits at 40A GeV. This is due to the large prevailing baryochemical density. Clearly, this is the environment in which one would want to study the properties of this new resonance in more detail. However, at all energies considered, we find that at chemical non-equilibrium the $\Theta^+(1540)$ is more abundant compared to $\Lambda(1520)$ and thus this new resonance could become an important probe

of the hadronization dynamics, provided detection issues, such as different branching ratios and experimental acceptances for the analyzed decays, $(\Lambda(1520) \rightarrow pK^+)$ and $(\Theta^+ \rightarrow pK_S)$ are resolved.

The observation of the pattern of relative yield of $\Theta^+(1540)$, seen in Fig. 5.9 (left), would firmly confirm the 4-quark, one anti quark content of this state. Namely, were for example the $\Theta^+(1540)$ another tri-quark baryon state, the yield ratio with (strange) baryons would be quite flat as function of collision energy. We further note that the absolute magnitude of the relative yield, seen in Fig. 5.9 (left), will be of help in establishing the degree of chemical equilibration.

In Fig. 5.9 (right), we show at the bottom the expected relative yield of the $\Xi^{--}(1862)[ssdd\bar{u}]$ relative to $\Xi^-[ssd]$. The $\Xi^*(1862)$ adds at the percentile level to the yield of observed Ξ and thus it is less influential in the statistical hadronization approach. The absence of variation of the relative yield with collision energy is due to cancellation of chemical factors. This relatively small relative yield at all collision energies here considered shows that indeed the pp environment, where it has been identified by the NA49 collaboration, is most suitable. The dotted lines, in Fig. 5.9 (right), are visibly breaking the trend in some of the results, indicating that the large χ^2 chemical equilibrium fit generates unreliable statistical model parameters.

We also show, in Fig. 5.9 (right) on the top, the yield of the pentaquark state $\Sigma(1776)[sddu\bar{u}]$ which for purpose of this study is assumed at the mass indicated. Again due to cancellation of key chemical factors in ratios shown in Fig. 5.9 (right), both being proportional to $\gamma_q^2 \lambda_d / \lambda_u$, the ratio is flat (except for the failed fit chemical equilibrium results). Considering that $\lambda_d \simeq \lambda_u$ and $\gamma_q \simeq 1.6$, the magnitude of relative yields seen in Fig. 5.9 (right) is primarily due to the hadron mass, and

degeneracy.

We have shown that inclusion of the pentaquark states in the study of particle production in heavy ion collisions improves the quality of our fits to experimental data. We find that $\Theta^+(1540)$ state influences the low energy SPS particle yield fit results. It can be expected that it will be detectable, in particular at low heavy ion collision energies, and thus should become a new probe of hadronization dynamics. The other pentaquark states will be hard to observe in heavy ion collisions.

5.5 Momentum dependence of the resonance-particle ratios as a freeze-out probe

In section 5.4, we have shown that the measurement of resonances can probe both the hadronization temperature, and the lifetime of the interacting hadron gas phase (Torrieri and Rafelski 2002; Rafelski et al. 2001). Ratios of a generic resonance (henceforward called N^*) to the light particle (which we will refer to as N) with an identical number of valence quarks are particularly sensitive probes of freezeout temperature because chemical dependence cancels out within the ratio. If we examine this ratio within a given $m_T > m_{N^*}$ range, we expect to disentangle flow and freeze-out conditions, since the ratio N^*/N should not depend on m_T for a purely static and thermal source (if there is no flow, $N^* \propto e^{m_T \cosh(y)}$ so $(N^*/N)_{m_T > m^*}$ is constant).

We therefore take the most general Boost-invariant freeze-out hypersurface in the Boltzmann limit (see Table 4.1, Eq. (4.11))

$$\frac{dN}{dm_T^2} \propto S(m_T, p_T) = \int_{\Sigma} r dr S(m_T, p_T, r), \quad (5.11)$$

where

$$S(m_T, p_T, r) = m_T K_1(\beta m_T) I_0(\alpha p_T) - \frac{\partial t_f}{\partial r} p_T K_0(\beta m_T) I_1(\alpha p_T), \quad (5.12)$$

with

$$\beta = \frac{\cosh[y_T(r)]}{T}, \quad \alpha = \frac{\sinh[y_T(r)]}{T} \quad (5.13)$$

and use it to calculate the ratio between two particles with the same chemical composition. The chemical factors cancel out, and we are left with

$$\frac{N^*}{N} = \left(\frac{g^*}{g} \right) \frac{S(m_T, p_T^*)}{S(m_T, p_T)}, \quad (5.14)$$

where g^* and g refer to each particle's degeneracy and the function $S(m_T, p_T)$ is given by Eq. (5.12). (Note that m_T is the same for N^* and N , but p_T varies).

Fig. 5.10 shows the application of this procedure to the cases $(K^* + \overline{K^*})/(K_S)$ (top), $\Sigma^*(1385)/\Lambda$ (middle), and η'/η (bottom) at two freeze-out temperatures and flows: $T = 140\text{MeV}$, $v_{max}/c = 0.55$ on left and $T = 170\text{MeV}$, $v_{max}/c = 0.3$ on the right. Significant deviations from simple constant values are observed, showing the sensitivity of the ratio to freeze-out geometry and dynamics. The analytically simple result in Eq. (5.14) is valid only if the light particle Y has been corrected for feed down from resonances, including N^* . In other words, Eq. (5.14) as well as Fig. 5.10 require that decay products from reconstructed N^* do not appear on the bottom of the ratio. Experiments usually do not do such feed down corrections (Fachini 2002; Markert et al. 2002a; Friese 2002), since this would increase both statistical and systematic error on the ratio, and it is not always possible to do such corrections at all (undetected decays) or in the full range of experimental sensitivity.

Introducing the feed down corrections into Eq. (5.14), we obtain

$$\frac{N_{\text{observed}}^*}{N_{\text{observed}}} = \frac{g^* S(m_T, p_T^*)}{g S(m_T, p_T) + \sum_i g_i^* b_{N_i^* \rightarrow N} R(m_T, p_{Ti})}. \quad (5.15)$$

Here, $S(m_T, p_T)$ describes the directly produced particles and has the form given by Eq. (5.11) and each term $R(m_T, p_{Ti}^*)$ describes a feed down contribution, in the form given in section 2.3.1 (In particular Eq. (2.34) and following)

Fig. 5.11 shows the ratios, including feed down of resonances, for the same particles and statistical hadronization conditions as were studied in Fig. 5.10. In the $\Sigma^*/(\text{all } \Lambda)$ case we omitted the feed down from Ξ to Λ which is usually corrected for (if this is not done the ratio $\Sigma^*/(\text{all } \Lambda)$ would depend strongly on the chemical potentials). We did allow for the $\phi \rightarrow K_S K_L$ feed down, since it is a strong decay that cannot so easily be corrected for³. We note that the feed down from particles with a different chemical composition cannot always be corrected for, and thus some resonances ratios will also acquire a (mild) dependence on the chemical potentials. This is even true for ratios such as $\eta'/(\text{all } \eta)$, given different $s\bar{s}$ content. In this chapter, these type chemical corrections were set equal to unity.

To further study the sensitivity of resonance-particle m_T -ratio to freeze-out dynamics, we also present the (feed down corrected) case as a function of p_T rather than m_T in Fig. 5.12. Unsurprisingly, we see grossly different behaviors, with many of the results coalescing. This of course is an expression of the fact that N^* and N have dramatically different p_T at the same m_T and vice versa. We believe that the m_T ratio will in general be more sensitive to freeze-out dynamics, since its dependence on m_T is dominantly due to freeze-out geometry and dynamics. However, the p_T dependence seen in Fig. 5.12 provides an important self-consistency

³See footnote in subsection 5.2.1

check for our previous results. We have found that the m_T ratios are often greater than unity even though there must be more ground state particles than resonances. Now it can be seen in the p_T ratio, that this requirement is satisfied.

5.6 Discussion

In general the the m_T and p_T dependence of the ratios in Fig 3 and, respectively, Fig 4 depends on freeze-out geometry, temperature and flow velocity. The introduction of a steeper flow profile will further raise all of the considered ratios, since a considerable fraction of particles will be produced in regions that do not flow as much. The influence of freeze-out dynamics will generally go in the same direction as freeze-out approaches the explosive limit ($dt_f/dr \rightarrow 1$). However, both the magnitude and the qualitative features of the two effects (flow and freeze-out velocity) will be considerably different. Especially, when more than one ratio is measured, it would appear that we will be able to determine the freeze-out condition. This is in contrast to the m_T distributions in Fig. 4.2, where the effects discussed in this paper result in linear corrections, which tend to compete, making the task of extracting the freeze-out dynamics much more ambiguous. Thus, there is considerable potential of resonance-particle m_T -ratios as a freeze-out probe.

The presence of a long living hadronic gas rescattering phase can distort our freeze-out probe. In particular, the apparent N^*/N ratio will be altered due to the depletion of the detectable resonances through the rescattering of their decay products. Its dependence on m_T will be affected in a non-trivial way, since faster (higher p_T) resonances will have a greater chance to escape the fireball without decaying, thus avoiding the rescattering phase altogether. Regeneration of resonances

in hadron scattering may add another m_T dependence which is different for the Σ^*/Λ and the K^*/K ratios (Bleicher and Stocker 2004). While, as discussed in the last section, evidence that a rescattering phase plays a great role in particle distributions is lacking, it would seem that the “safest” probes for freeze-out are the particles and resonances most unlikely to rescatter.

For this reason we have included the η'/η ratio in our considerations. $\eta \rightarrow \gamma\gamma$ and $\eta' \rightarrow \gamma\gamma$ have very different branching ratios, but have the same degeneracies and similar but rather small partial widths. The electromagnetic decay mode is practically insensitive to posthadronization dynamics. Regeneration effects are suppressed since the hadronic two body decay channel is suppressed. All these features make these particles interesting probes, allowing for the analysis considered here. η, η' mesons have been measured at SPS energies in the $\gamma\gamma$ decay channel (Albrecht et al. 1995; Lebedev et al. 1994), and detectors such as PHENIX are capable of reconstructing the same decays at RHIC.

In summary, we have presented an overview of the different statistical freeze-out models used to fit heavy ion data. We have shown how the freeze-out geometry and freeze-out dynamics influences the hadron spectra. Our primary result is the finding that the m_T dependence of the resonance-particle ratios is a probe of freeze-out. We have presented these ratios for three particle species and two freeze-out conditions and have considered how our results could be altered by posthadronization phenomena.

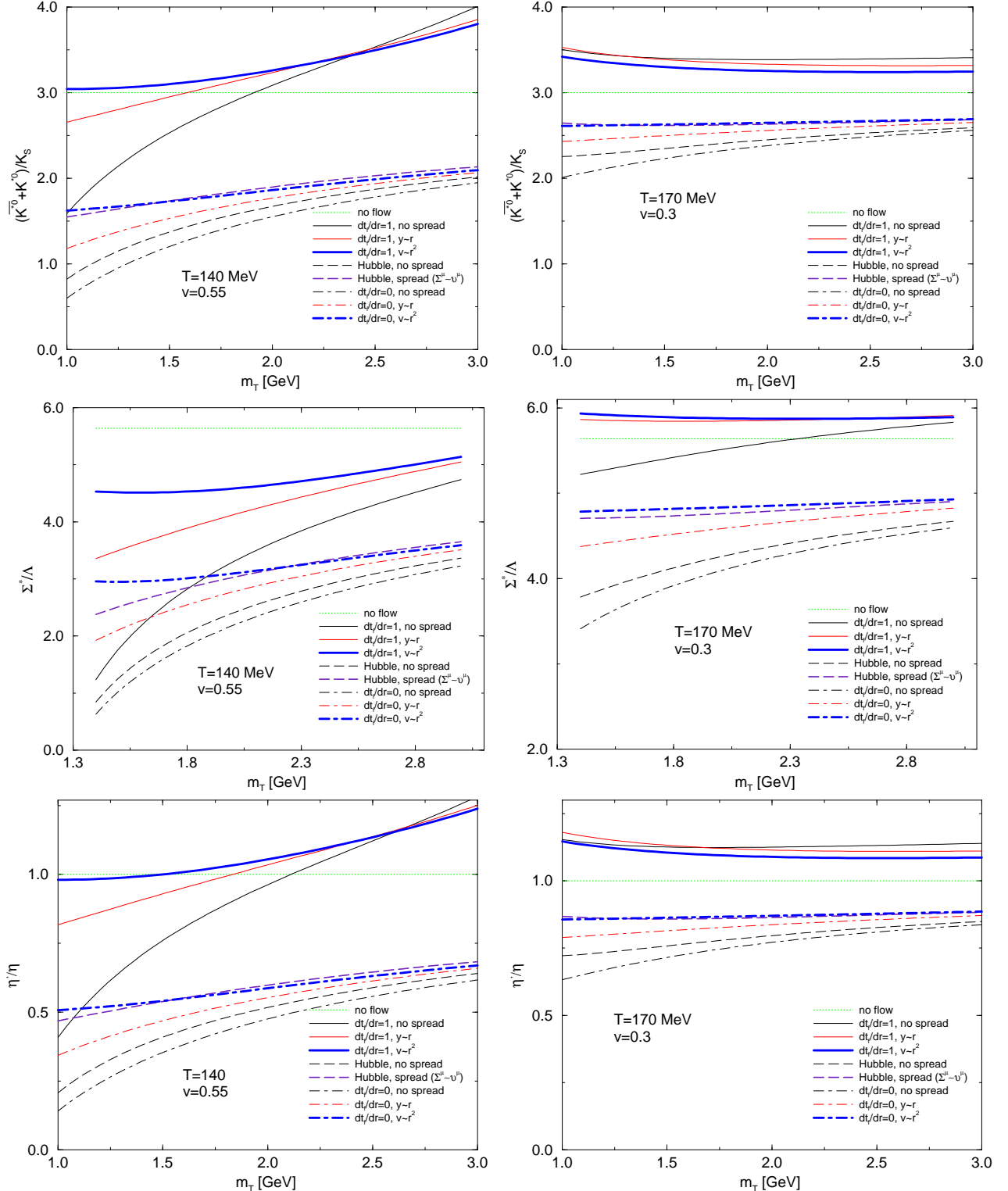


Figure 5.10: (Color online) Dependence of the K^*/K , Σ^*/Λ and η'/η on the Freeze-out model .

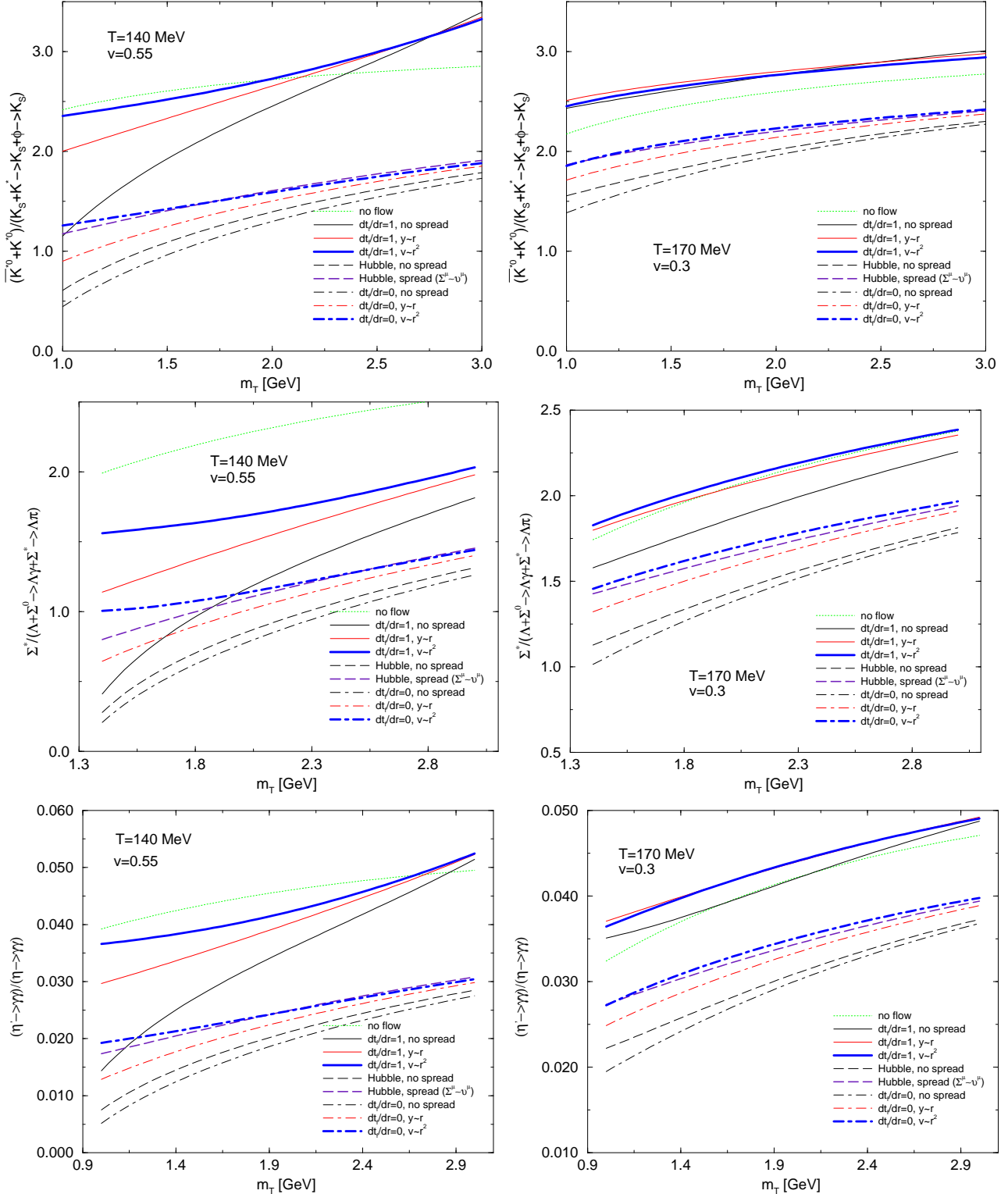


Figure 5.11: (Color online) $(K^* + \bar{K}^*)/(\text{all } K_S)$, $\Sigma^*(1385)/(\text{all } \Lambda)$ and $\eta'/(\text{all } \eta)$ ratios, including feed down from resonances.

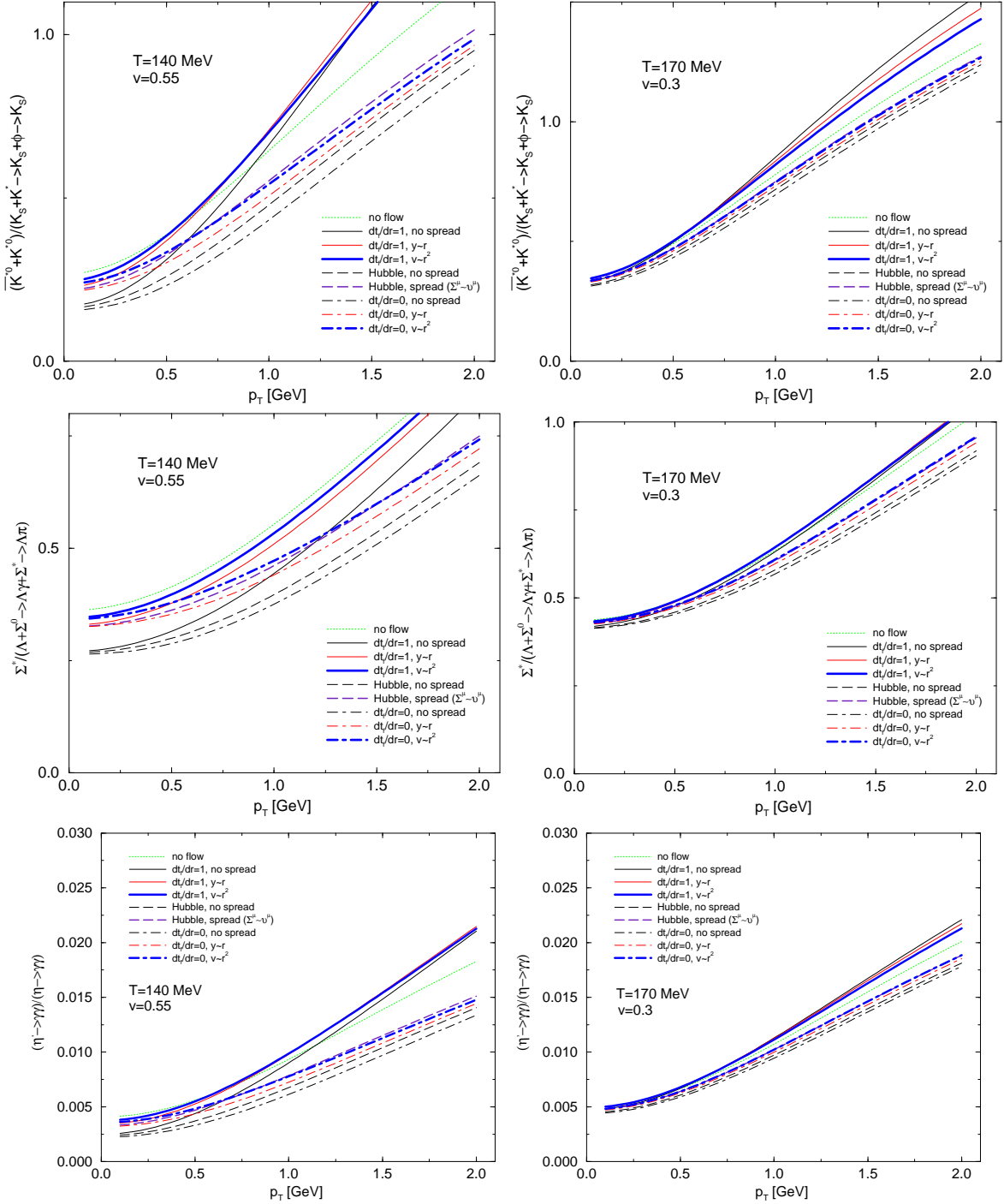


Figure 5.12: (Color online) p_T dependence of $(K^* + \bar{K}^*)/\text{(all } K_S)$, $\Sigma^*(1385)/\text{(all } \Lambda)$ and $\eta'/\text{(all } \eta)$ ratios, including feed down from resonances.

CHAPTER 6

Azimuthal anisotropy

6.1 Introduction

Matter flow azimuthal anisotropy has long been considered a promising soft hadron observable in the study of heavy ion collisions. This anisotropy is considered an important evidence for collective matter flow (Ollitrault 1992; Voloshin and Zhang 1996), as it indicates thermalization early in the system's evolution (Sorge 1997).

Generally one simplifies the complex transport problem and considers hydrodynamic model, i.e. dynamics of first moment of the momentum distribution of particles. Assuming in the local reference frame an asymmetric thermal momentum distribution we evaluate below the actual final state particle distributions. Azimuthal anisotropy in hydrodynamics arises from anisotropic gradient of pressure (force field) when the collision between nuclei is not exactly head-on central. In this way hydrodynamic model leads to the azimuthal momentum dependent asymmetry of final state particle distributions.

Anisotropy in the final state can be quantified in terms of a Fourier decomposition of the momentum distribution (Poskanzer and Voloshin 1998),

$$E \frac{dN}{d^3p} = \frac{1}{2\pi} \frac{dN}{p_T dp_T dy} \left[1 + \sum 2v_n \cos(n\phi) \right], \quad (6.1)$$

where the angle ϕ is defined with respect to the reaction plane (Ollitrault 1993) in

an event-by-event analysis (Fig. 6.1).

The second coefficient v_2 , usually called elliptic flow, has been subject to a considerable amount of experimental investigation at AGS, SPS and RHIC energies (Pinsky et al. 1999; Appelshauser et al. 1998; Adler et al. 2002a; Adler et al. 2003). The fourth coefficient v_4 has recently been measured at RHIC (Adams et al. 2004). (odd components, such as the directed flow v_1 , disappear in the Boost-Invariant limit)

Generally, v_n is a function of momentum. It has been found that $v_2(p_T)$ at low p_T and central rapidity agrees with hydrodynamical predictions (Kolb and Heinz 2003; Hirano and Tsuda 2003). However, RHIC experiments have shown that at $p_T \sim 1.5$ GeV v_2 rise saturates to a particle-dependent limit (Adler et al. 2002a; Adler et al. 2003), something so far hydrodynamic approach could not explain. Since this p_T value is also seen as being too soft for $v_2(p_T)$ to be determined by “hard” perturbative processes, this behavior has not been fully understood.

However, coalescence of partons obeying perturbative dynamics has been shown to lead to saturation of $v_2(p_T)$ (Molnar and Voloshin 2003). While this approach does not as yet cover consistently the low p_T range (Fries et al. 2003) and hence is yet to undergo detailed quantitative testing, its success suggests that, more generally, the process of quark-gluon hadronization can influence significantly the resulting $v_2(p_T)$. Here we address this possibility systematically, but qualitatively in that we do not introduce resonance decays and flow profile of matter. Our objective is to identify physical mechanisms rather than to explain the experimental data.

Our study will show that there are $v_2(p_T)$ saturation mechanisms based solely on rapid hadronization of a hydro-dynamically evolving opaque system, such

as quark-gluon plasma. We shall use the Cooper-Frye approach of Eq. (2.17) (Cooper and Frye 1974).

$$E \frac{dN}{d^3p} = \int d^3\Sigma^\mu p_\mu f(u^\mu p_\mu, T, \mu). \quad (6.2)$$

As we have argued in the previous chapters, this formula is particularly relevant if most observed particles are emitted when the system undergoes a phase transition to a gas of particles having a much larger mean free path (QGP \rightarrow expanding Hadron Gas). In this case, the Cooper-Frye formula, in particular the hadronization hypersurface $d^3\Sigma_\mu$, ceases to be just a computational prescription to generate particles from a continuum, but acquires physical significance as the representation of the hadronizing QGP in position space. Thus a more thorough exploration of how it can modulate the shape of $v_2(p_T)$ is required. The form of $d^3\Sigma_\mu$ is determined by the dynamics of the QGP \rightarrow HG phase transition.

Several theoretical studies and also general behavior of experimental results suggest that hadronization happens rapidly, perhaps through viscous fingering of the vacuum (Csorgo and Csernai 1994), driven by a mechanical instability at the point when the pressures (including that of flow) of the two vacua balance, but the velocity still point outwards (Rafelski and Letessier 2000). In this situation it is natural to expect a “burning log” type emission (Torrieri and Rafelski 2003b), with a fast ($\sim c$) moving emission surface rapidly consuming the fireball from outside in. In contrast to this dynamical hadronization picture, a “blast-wave” freeze-out model in which the freeze-out time does not depend on the transverse freeze-out radius is presently popular among experimentalists, perhaps due to the simplicity of its use in a fitting procedure (Burward-Hoy 2003; Adams et al. 2003b; Afanasiev et al. 2003; Sandor et al. 2004).

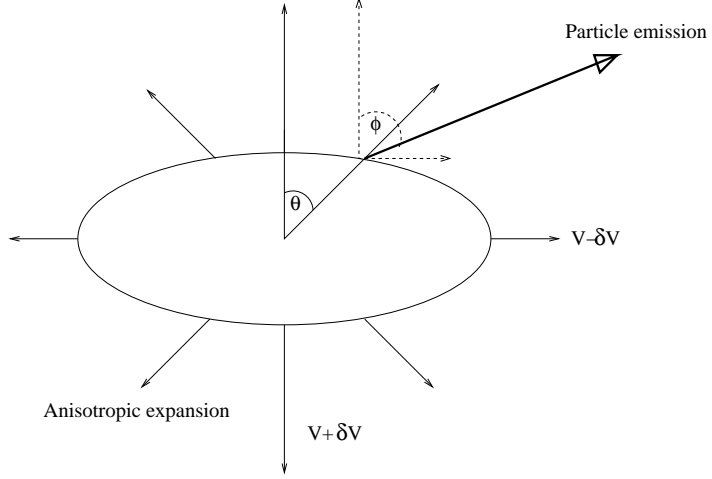


Figure 6.1: A general freeze-out surface in configuration space .

As we will show these two scenarios (burning log and non-dynamic blast wave) give considerably different $v_2(p_T)$ for the same initial matter flow anisotropy. In particular, we find that a burning-log type freeze-out dynamics leads in qualitative terms to the observed v_2 saturation.

6.2 v_n in the Cooper-Frye approach

We shall use the approach taken in chapter 4, using boost-invariance to construct our flow and Σ_μ . Hence, in the most general boost-invariant case

$$\Sigma^\mu = \begin{pmatrix} t_f \cosh(y_L) \\ r_f \cos(\theta) \\ r_f \sin(\theta) \\ t_f \sinh(y_L) \end{pmatrix}, \quad u^\mu = \gamma_T \begin{pmatrix} \cosh(y_L) \\ v_T \cos(\theta) \\ v_T \sin(\theta) \\ \sinh(y_L) \end{pmatrix}. \quad (6.3)$$

Where θ is the angle of the emission point in configuration space (Fig. 6.1, not to be confused with the emission angle ϕ). However, we forgo cylindrical symmetry, and Fourier expand both the flow and hadronization hypersurface, keeping only even

terms given the symmetry,

$$t_f(r, \theta) = \sum_{n=0}^{\infty} \Delta_{2n} t_f(r) \cos(2n\theta), \quad (6.4)$$

$$r_f(r, \theta) = \sum_{n=0}^{\infty} \Delta_{2n} r_f(r) \cos(2n\theta), \quad (6.5)$$

$$v_T(r, \theta) = \sum_{n=0}^{\infty} \Delta_{2n} v(r) \cos(2n\theta). \quad (6.6)$$

We assume a purely elliptic fireball ($n = 0, 1$ only), and moreover a “fast” freeze-out so as to neglect t_f θ -dependence. If the fireball is approximately circular in transverse space, the elliptical freeze-out hypersurface becomes an ellipse (with a correction of $O(\delta r^2)$),

$$\Sigma^\mu = \begin{pmatrix} t_f(r) \cosh(y_L) \\ (r + \delta r) \cos(\theta) \\ r \sin(\theta) \\ t_f(r) \sinh(y_L) \end{pmatrix}, \quad (6.7)$$

$$u^\mu = \gamma_T(r, \theta) \begin{pmatrix} \cosh(y_L) \\ (v + \delta v \cos(\theta)) \cos(\theta) \\ (v + \delta v \cos(\theta)) \sin(\theta) \\ \sinh(y_L) \end{pmatrix}, \quad (6.8)$$

$$\gamma_T = \frac{1}{\sqrt{1 - (v + \delta v \cos(\theta))^2}}. \quad (6.9)$$

We can now parametrize the freeze-out hypersurface element in terms of r, θ, y_L = (radius, angle and longitudinal rapidity y_L)

$$\begin{aligned} d^3\Sigma^\mu &= \epsilon^{\mu\nu\alpha\beta} \frac{\partial\Sigma_\nu}{\partial r} \frac{\partial\Sigma_\alpha}{\partial\theta} \frac{\partial\Sigma_\beta}{\partial y_L} \\ &= \begin{pmatrix} \cosh(y_L)(r + \delta r \sin^2(\theta)) \\ \frac{\partial t_f}{\partial r} r \cos(\theta) \\ \frac{\partial t_f}{\partial r} (r + \delta r) \sin(\theta) \\ \sinh(y_L)(r + \delta r \sin^2(\theta)) \end{pmatrix} dy_L dr d\theta. \end{aligned} \quad (6.10)$$

If we combine the obtained u^μ and $d^3\Sigma_\mu$ with the usual parametrization for the emitted particle's 4-momentum

$$p^\mu = \begin{pmatrix} m_T \cosh(y) \\ p_T \sin(\phi) \\ p_T \cos(\phi) \\ m_T \sinh(y) \end{pmatrix} \quad (6.11)$$

we obtain an expression of the boost-invariant momentum distribution in terms of ϕ, p_T, m_T and y :

$$\begin{aligned} E \frac{dN}{d^3p} &= \int_0^{R_{max}} r dr \int_{-\infty}^{\infty} dy_L \int_0^{2\pi} d\theta [m_T \cosh(y - y_L) \times \\ &\quad \times (1 + \frac{\delta r}{r} \sin^2(\theta)) - p_T \frac{\partial t_f}{\partial r} (\cos(\theta - \phi) + \frac{\delta r}{r} \sin(\theta))] \\ &\quad f(\frac{\gamma_T}{T} [m_T \cosh(y - y_L) - p_T (v + \delta v \cos(2\theta)) \cos(\theta - \phi)]) \end{aligned} \quad (6.12)$$

Where $f(x) = e^{-x}$ in the Boltzmann approximation (good for all particles except pions) and for pions:

$$f(x) = \sum_{n=0}^{\infty} (-1)^n \lambda_\pi^{n+1} e^{-nx}.$$

Each v_n can now be calculated using

$$v_n = \frac{\int_0^{2\pi} \cos(n\phi) E \frac{dN}{d^3p}}{2 \int_0^{2\pi} E \frac{dN}{d^3p}} \quad (6.13)$$

the integrals over ϕ and y_L can be done analytically in the boost-invariant limit, using the modified Bessel Functions

$$I_n(x) = \int_0^{2\pi} \frac{d\phi}{2\pi} \cos(n\phi) e^{x \cos(\phi)} \quad (6.14)$$

$$K_n(x) = \int_{-\infty}^{\infty} dy_L \cosh(ny_L) e^{-x \cosh(y_L)} \quad (6.15)$$

and the following result

$$\int_0^{2\pi} \frac{d\phi}{2\pi} \cos(n\phi) e^{a \cos(\phi) + b \sin(\phi)} = T_n \left(\frac{a}{\sqrt{a^2 + b^2}} \right) I_n \left(\sqrt{a^2 + b^2} \right) \quad (6.16)$$

$$\int_0^{2\pi} \frac{d\phi}{2\pi} \sin(n\phi) e^{a \cos(\phi) + b \sin(\phi)} = S_n \left(\frac{a}{\sqrt{a^2 + b^2}} \right) I_n \left(\sqrt{a^2 + b^2} \right) \quad (6.17)$$

where $T_n(x)$ and $S_n(x)$ are defined in terms of Chebyshev polynomials

$$T_n(x) = \cos(n \cos^{-1}(x))$$

$$S_n(x) = \sin(n \cos^{-1}(x)) = \sqrt{1 - T_n^2(x)}$$

Putting everything together, we get

$$v_n(p_T) = \frac{\int r dr \int d\theta J_n}{2 \int r dr \int d\theta J_0}, \quad (6.18)$$

where ($\alpha = p_T(v + \delta v \cos(\theta))$)

$$\begin{aligned} J_{n>0} = & \left[K_1 \left(\frac{\gamma_T m_T}{T} \right) \left(1 + \frac{\delta r}{r} \sin(\theta)^2 \right) - p_T \frac{\partial t_f}{\partial r} K_0 \left(\frac{\gamma_T m_T}{T} \right) \right] T_n(\cos[\theta]) I_n(\alpha) - p_T \frac{\partial t_f}{\partial r} K_0 \left(\frac{\gamma_T m_T}{T} \right) \\ & \left[\frac{1}{2} \cos[\theta] (T_{n+1}(\cos[\theta]) I_{n+1}(\alpha) + T_{n-1}(\cos[\theta]) I_{n-1}(\alpha)) + \right. \\ & \left. \frac{1}{2} \sin(\theta) (S_{n+1}(\cos[\theta]) I_{n+1}(\alpha) - S_{n-1}(\cos[\theta]) I_{n-1}(\alpha)) \right] \end{aligned} \quad (6.19)$$

and

$$J_0 = \left[K_1 \left(\frac{\gamma_T m_T}{T} \right) \left(1 + \frac{\delta r}{r} \sin(\theta)^2 \right) - p_T \frac{\partial t_f}{\partial r} K_0 \left(\frac{\gamma_T m_T}{T} \right) \right] I_0(\alpha) - p_T \frac{\partial t_f}{\partial r} K_0 \left(\frac{\gamma_T m_T}{T} \right) I_0(\alpha) \quad (6.20)$$

For a quantitative fit to be physically meaningful, resonance contributions ($\sim 50\%$ of the total K_S, Λ , more for π (Torrieri and Rafelski 2003a)) need to be taken into account. As we have seen in the previous chapters, calculating these contributions is numerically intensive (Baran et al. 2004), and work to perform such a quantitative fit, together with analysis of particle spectra (Torrieri et al. 2004), is currently in progress.

6.3 Results and discussion

We have used Eq. (6.18) to qualitatively explore the dependence of $v_2(p_T)$ for K_S, Λ and π on the parameters of statistical freeze-out. It is apparent that the freeze-out dynamics parameter $\partial t_f / \partial r$ has a non-negligible effect on $v_2(p_T)$ (Fig. 6.2 right). In particular, by changing the freeze-out hypersurface towards the “burning log” ($\partial t_f / \partial r = -1$) limit, it is possible to raise and lower the saturation scale and p_T at which the saturation occurs. Varying $\partial t_f / \partial r$ also controls the mass dependence of the observed $v_2(p_T)$, with an increased $\partial t_f / \partial r$ leading to a different saturation scale for the K^0 and Λ , as observed by experiment. Comparing the right panels of Fig. 6.2 left and right, it becomes clear that a simultaneous fit for the $v_2(p_T)$ of several different particles would constrain both the flow anisotropy and the freeze-out dynamics.

Of course, a physical fireball is not characterized by a single flow, but by a spatially varying flow profile. Fig. 6.3 (right) explores the effect of a range of physically reasonable profiles on the observed v_2 . Unsurprisingly, adding a flow profile diminishes the observed v_2 , while maintaining the saturation scale determined by dv/v and $\partial t_f / \partial r$.

Finally, we note that corrections due to azimuthal anisotropy of the freeze-out hypersurface and chemical non-equilibrium are also very small, even as the chemical potential approaches the Bose-Einstein condensation limit.(Fig. 6.3 left, Fig. 6.4 left). Temperature corrections are more noticeable (Fig. 6.3 left).

Eq. (6.19) makes it apparent that the interference between space and flow anisotropy means that even a purely elliptic fireball will acquire $v_{n>2} \neq 0$ for all even numbers Fig. 6.4 (right) shows the contributions of v_n arising from the freeze-out of a purely elliptical fireball. It can be seen that, for $n = 4$, this contribution is not negligible, and is in fact comparable to that arising from Hydro (Kolb 2003).

This result, together with the recent experimental observation of directed flow (Adams et al. 2004), suggests that v_3 and v_5 away from central rapidity could also be promising observables: Our model finds $v_{3,5} = 0$ since we assume boost-invariance. However, a full 3-fluid calculation, together with Eq. (6.19), would yield these quantities easily. Given the significant observed directed flow (Adams et al. 2004), as well as the v_4 calculated in Fig. 6.4, odd $v_{n>1}$ s could be within experimental observation. These coefficients make for particularly interesting probes, since they arise solely from freeze-out effects and deviations from boost-invariance.

In conclusion, we have shown that observed $v_2(p_T)$ depends strongly on the freeze-out hypersurface, and that a burning-log type freeze-out can explain the observed $v_2(p_T)$ saturation. We have further shown that $v_n(p_T)$ is an extremely sensitive freeze-out probe, capable of constraining statistical freeze-out models very tightly. As experimental data in this area becomes richer and more precise, more realistic numerical studies of both spectra and $v_n(p_T)$ might establish themselves as crucial analysis tools.

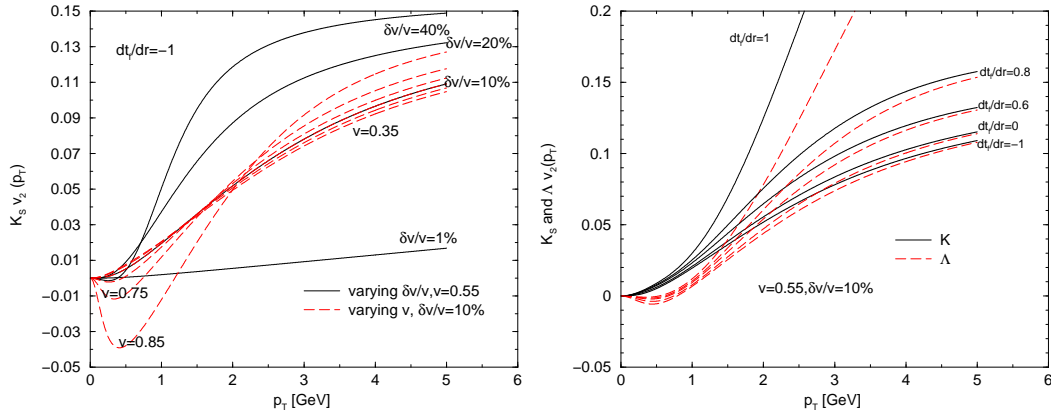


Figure 6.2: Left: Varying flow anisotropy. Right: Varying freeze-out dynamics .

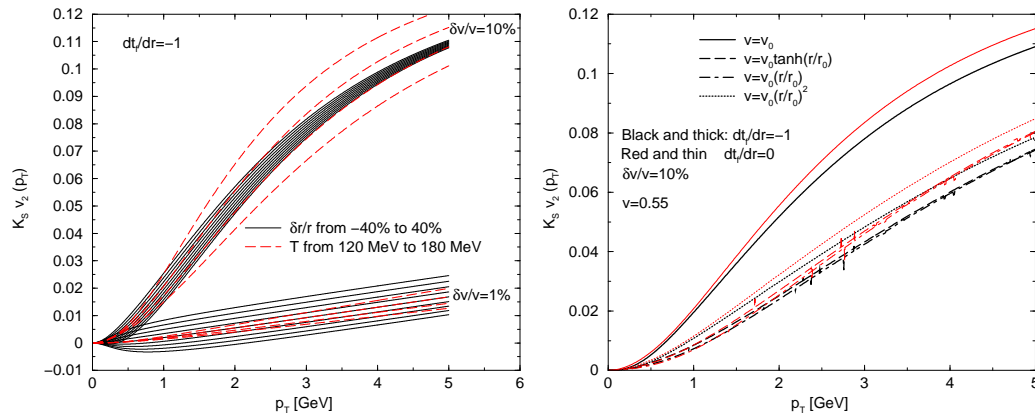


Figure 6.3: Left: Varying geometrical anisotropy. Right: Varying flow spread .

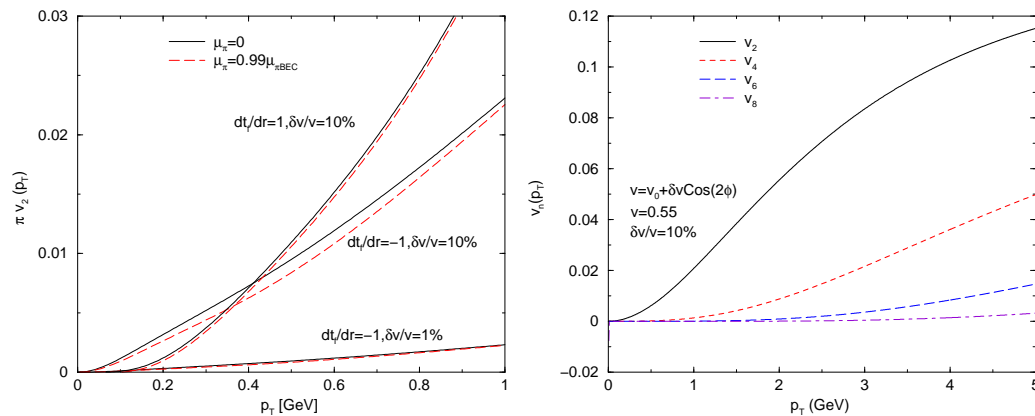


Figure 6.4: Left: Varying flow profile. Right: Higher v_n s from an elliptic fireball .

CHAPTER 7

Summary and outlook

7.1 What chapters 3-6 have shown

The statistical hadronization model, together with hydrodynamic flow, are capable of describing a large amount and variety of experimental data with comparatively few fit parameters. However, the variety of statistical models on “the market”, which manage to describe the data acceptably (to at least part of the heavy ion community) somewhat invalidates statistical hadronization as a physical picture.

A “slow” staged equilibrium freeze-out starting at $T=170$ MeV (Heinz and Jacob 2000), A sudden equilibrium freeze-out at $T=165$ MeV (Baran et al. 2004), and a fast explosive freeze-out starting at $T=140$ MeV (Rafelski and Letessier 2003b) are not “the same model”. They are profoundly different physical pictures, which lead to different conclusions about what the QGP-HG phase transition should look like.

That all three have been successfully employed to describe experimental data simply means that two (or possibly all three!) of these pictures are the heavy ion equivalent of epicycles: Models with no connection with reality, which are lucky enough to fit some of the experimental data.

In chapter 2, we have presented several candidates for a probe capable of

distinguishing the epicycles from the real physics Chapters 3-6 examined each of the candidates in detail, in light of the experimental evidence. To what extent have we succeeded at isolating the true physical picture?

7.1.1 Does non-equilibrium sudden hadronization work?

Sudden hadronization scenarios are considerably easier to falsify than a complicated staged freeze-out phase. In both the equilibrium and non-equilibrium scenarios, particle yields place strong constraints on temperature and chemical potential. Particle spectra place equally strong constraints on temperature and flow. If the temperature which fixes the yields (“chemical freeze-out”) differs from the temperature which fixes the spectra (“thermal freeze-out”), a fit to normalized yields should conclusively fail.

That such a fit does not fail is, perhaps, the most firm conclusion to be drawn from this thesis. In chapters 3 and 4, we have shown that fits based on the same temperature for yields and spectra succeed, or at least are acceptable, both at SPS and RHIC energies, if the non-equilibrium sudden hadronization ansatz is used.

If, however, hadronization happens in equilibrium, we find that the χ^2/DoF increases beyond meaningfulness, a conclusion enforced by the lack of definite minima in equilibrium χ^2 profiles. Fig. 5.3 shows that the equilibrium scenario fails to describe short-lived resonance yields (which it does not aim to describe anyways): The scarcity of these resonances drives the fit to a temperature at which its impossible to describe ratios such as Λ/Ξ without introducing γ_q and γ_s .

The checks performed in this thesis are not, however, the only ones possible. In particular, in the following two years experiments should publish normalized spectra of unstable resonances. These spectra pose much tighter constraints because such resonances have the same quark composition as light particles. Hence, their normalization, with respect to these light particles, is controlled by temperature alone.

Resonances and absolute normalization remove the correlation between temperature and flow: It is not possible to adjust the slopes by shifting the temperature and transverse flow along the same contour, since in this case normalization suffers. However, temperature is still strongly correlated with chemical potentials (especially γ_s and γ_q). Using spectra of short-lived resonances will remove this correlation, and show once and for all if there is a meaningful temperature minimum.

It should be noted that spectra of ϕ and K^* were already modeled at RHIC, and are well described by the single freeze-out ansatz. Much more, however, is yet to come.

7.1.2 Have we ruled out staged hadronization?

Ruling out Staged hadronization is considerably more difficult, since this model is not very quantitative beyond the “Two temperatures, one for chemical and one for thermal freeze-out” requirement.

One can argue that a good description of both abundancies and spectra of particles with very different interaction channels within the same temperature and flow is, by itself, a piece of evidence against staged hadronization. If staged

hadronization occurs, why should the Ω , with no s-channel interaction with the π , have the same freeze-out temperature and flow as the π , which interacts via the s-channel with pretty much every other particle in the hadron gas.

Why should the Λ and $\bar{\Lambda}$, or Ξ and $\bar{\Xi}$ be described by the same temperature and flow at the SPS, given that in a baryon-rich medium particles and antiparticles have very different reaction channels ($\Lambda p \rightarrow \Lambda p$. $\bar{\Lambda} p \rightarrow \pi K, \dots$). This is even more true in the case of spectra of short lived resonances: As shown in Fig. 4.8, microscopic models predict a very p_T dependent re-scattering of decay products, which should bring the spectra of short-lived resonances away from hydro-dynamically predicted values.

However, this evidence is not really enough to rule out the model, considering that, as proven in chapter 4, a fit for quite a large range of particles can be made with either a “sudden freeze-out+resonances” ansatz, or a “no resonances and arbitrary normalization” description. The χ^2 and the fitted temperature comes out remarkably similar in these two approaches.

Direct detection has made clear that the presence of resonances in spectra is an experimental fact rather than a model assumption. The analysis of resonance yields performed in chapter 5 points to a short interacting hadron gas phase, as well as a low chemical freeze-out temperature. Of course, proponents of staged hadronization would argue that the effect of out-of-equilibrium regeneration would invalidate this conclusion (Bleicher and Stocker 2004).

7.1.3 Have we constrained freeze-out dynamics?

Here, the answer must be “not yet”: Our fits to spectra have shown that freeze-out dynamics, parametrized for central and near-central collisions by $\frac{\partial t_f}{\partial r}$, is an important factor in determining inverse slopes, and can be extracted if enough particles are fitted. We have presented attempts at such extraction at both SPS and RHIC energies. A minimum in the χ^2 profile was found, but it is not fully convincing. One way of constraining this minimum further is through fitting more low p_T particles, since including the low p_T region makes the fit considerably more sensitive to the variation of $\frac{\partial t_f}{\partial r}$ (The phase space volume of the emitted hadron $\sim E - p_T \frac{\partial t_f}{\partial r}$). PHOBOS recently lowered the observed p_T range by two orders of magnitude (Back et al. 2004), and more particles (certainly K , hopefully protons) will be coming.

However, a deeper problem remains: As we have shown, the choice of flow profile correlates with the choice of freeze-out dynamics. This is not surprising, since both quantities are determined by the condition chosen for freeze-out, as can be seen by comparing different hydrodynamic models (Teaney et al. 2001; Schnedermann and Heinz 1993). However, it means that extracting conclusively Σ^μ from fits becomes considerably more computationally intensive, which makes exploring other probes, more capable of extricating freeze-out dynamics separately from flow profile, necessary.

Some probes were proposed in chapters 5 and 6. Resonances ratios as a function of m_T are a promising analysis tool, but experimental results have yet to be presented. v_2 , described in chapter 7, is also a promising probe, but once again resonance contributions are needed to describe existing experimental data (Dong

et al. 2004).

Finally, there is the traditional probe for exploring freeze-out in configuration space: Hanbury-Brown-Twiss interferometry (HBT) (Wiedemann and Heinz 1999). Since this thesis did not include HBT calculations, we have not discussed the current state of affairs in any detail beyond the problems faced by statistical models in fitting HBT (Heinz and Kolb 2002). The solution to these problems might be tied to sudden freeze-out (Csernai et al. 2003), or to the fact that assumptions going into HBT models might be, for many reasons, overly simplistic (Gastineau and Aichelin 2000; Bolz et al. 1993; Wong 2004).

7.2 Outlook on the heavy ion experimental program

This thesis was written well before all of the RHIC data has been analyzed. Indeed, the most interesting and surprising experimental results might well still be in the future. As noted elsewhere, while the resonance program has collected a convincing signal for a huge array of particles (with more to come), detailed quantitative observations, such as yields, ratios and spectra for all detected resonances and exotica, are yet to be published.

Charm and bottom production is another topic which awaits most of its experimental data. Heavy quarks will probably never be chemically equilibrated at any energy, and the great majority of their yields will always be produced during the initial high Q^2 collisions (Thews et al. 2001; Schroedter et al. 2000). However, a quark gluon plasma will equilibrate them thermally, and hadronization will distribute them in a radically different way than microscopic hadronic processes. For sudden freeze-out to be consistent, it should describe quarks independently of

their mass. This means that charmed particles (ψ, ψ', D etc), beauty states and mixtures (B_c) should be produced according to their statistical weights, and their momentum distribution should be modeled by the same flow as that of light quarks. We shall see if this is really the case, as the predictions of statistical models can differ drastically (\sim order of magnitude) from the purely hadronic ones (Schroedter et al. 2000).

Beyond the current RHIC program, we can look forward to the TeV energy range accessible to the LHC. While hadronization conditions will probably not be that different from RHIC (the chemical potentials at mid-rapidity should both be close to zero), the initial conditions and equilibrated evolution are likely to be markedly different. In particular, initial collisions are likely to generate a number of heavy quarks comparable to the strange quarks created at SPS and RHIC. If the system thermalizes as rapidly as the RHIC system seems to be, its temperature during the initial stage of the hydrodynamic evolution is likely to be well in the perturbative QGP range. Perhaps, if this phase lasts a long time, we will also see interesting electroweak effects (another phase transition accessible to experimental study?). At present it is not clear what the effect of this initial evolution will be, and whether any hadronic signals will survive subsequent cooling.

The most interesting physics, however, might not come so much from pushing the energy boundary higher and higher, as from comparing as many different collision energies, system sizes and chemical conditions as possible. The SIS, AGS and SPS have explored conditions in a wide range of nuclei at energies ranging from 1 to 20 GeV. RHIC has pushed this boundary to the hundreds of GeV, the LHC will push it into the TeV range, and the future SIS facility will look for low energy

but high-density systems. Taking all these experiments together results in a large region in temperature, chemical potential and system size which needs to be systematically analyzed. At what point do qualitatively new features (eg equilibration, or $\gamma_{q,s} \neq 1$) come in? What is the critical system size or collision energy needed for “most of the system” to become thermalized? Where exactly is the phase transition boundary, and are there any critical points?

We do not yet know the answer, but can say convincingly that soft physics will play an important role in obtaining it. As remarked in chapter 1, hard probes (such as jet quenching) are useful to tell us some bulk properties of the matter produced in highly energetic heavy ion collisions. If, however, one wants to explore how these bulk properties change with energy, or even relate the measured values to thermodynamics, hard processes, on their own become much less useful. It is only soft physics which will be able to determine at what point a qualitative change in microscopic degrees of freedom has occurred. To accomplish this, however, requires more than the new experimental data. Statistical hadronization itself needs to be understood better, both at the phenomenological and fundamental level.

7.3 Outlook on statistical hadronization

As the previous sections have shown, there is a lot more data which need to be analyzed in the statistical model framework to be able to tell convincingly which statistical model reflects physics. Fortunately, as the previous chapters have mentioned, the soft physics data taking at both SPS and RHIC is far from over. The range of particles analyzed in this theses, and many more, need to be systematically examined at the large range of collision energies and system size accessible to

modern day and future experiments.

For this reason, the immediate next step as far as the work described in this thesis is concerned is the development of a statistical hadronization code to be made available open-source to experimental collaborations. This will provide experimentalists with an open and universal “standard statistical model” to which to compare all their data, as well as a guarantee against errors (which, as we found, are very easy to make, given the thousands of particles and decay modes which need to be calculated). We have been developing such a code (named SHARE) together with the Krakow group (Baran et al. 2004). The first part of SHARE, which calculates 4π yields, has recently been released (Torrieri et al. 2004). Further modules (covering spectra, v_2 and HBT) are currently in development.

Another possible direction for statistical hadronization research is investigating its mathematical consistency, and improving its formalism. At present, there is no indication that either sudden freeze-out or staged freeze-out are self-consistent. Would inelastic interactions of a hadron gas really freeze-out at $T=170$ MeV, as staged freeze-out assumes? Would elastic interactions of an explosively hadronizing plasma at $T=140$ MeV really be negligible? If the answer to both these questions is no, to what extent does departure from equilibration impact observables? What is the quantitative systematic error such effects give to fitted thermal and flow parameters?

One way to answer these questions is to feed statistical model output into microscopic models, such as uRQMD. At present, uRQMD is incapable of fully describing any of the RHIC observables (strange particle yields, collective flow, and resonance production). However, this does not preclude statistical production

followed by hydrodynamic evolution. The Monte-Carlo module described in chapter 3 is being developed and incorporated into SHARE, as a “plug” for uRQMD. Hopefully, this will lead to some of the above questions being answered.

On a more fundamental level, it is clear that the statistical hadronization formalism needs developing. Reducing all particles to Lorentz-scalar objects emitted from a 3D locus in space, as the Cooper-Frye formula does, is a rough approximation which might miss important physical features of the hadronizing system. In particular, interaction of the two phases of matter at hadronization might have non-negligible consequences (Bugaev 2004). Enforcing conservation laws and entropy non-decrease locally on each hadronizing volume element might lead to non-trivial changes of the statistical parameters across the phase transition. $\gamma_q > 1$, discussed extensively in this dissertation, is a simple example. It might not be the only parameter which changes significantly as the system undergoes a rapid phase transition. (other workers have proposed a change in T (Keranen et al. 2003)).

More ambitiously, the above questions might be answered by tying the statistical model to a more fundamental picture of hadronization, possibly involving a microscopic effective theory. Perhaps insights in this direction might be obtained by examining at what energy range (p_T and rapidity) the statistical model ceases to provide a good physical description of the data, and what takes its place. Recently, a lot of interest has been aroused by the fact that several intermediate energy observables ($p_T \sim 1\text{GeV}$, below the scale described by pQCD) can be described in terms of parton coalescence (Fries et al. 2003; Molnar and Voloshin 2003). While this model’s ability to describe the data is compelling, its failings on a fundamental level (energy-momentum conservation and entropy non-decrease) mean that is a

limiting case of a larger process. In particular, it should be possible to combine coalescence and statistical hadronization as two limits of a single framework (this is especially true for non-equilibrium statistical hadronization: After all, it can be argued that statistical hadronization with $\gamma_{q,s} \neq 1$ is another way of viewing parton coalescence into massive states, with probabilities given by thermal weights).

It should be reiterated, however, that these advances in theoretical understanding are very unlikely unless the right statistical hadronization model is experimentally selected. Max Planck found that black body radiation fits a $\frac{1}{e^{\frac{\omega}{kT}} + 1}$ distribution years before he found a fundamental description of this phenomenon. Similarly, one hopes our rough phenomenological fits will help elucidate one of the greatest unsolved mysteries in modern physics: The structure of that strange, complex and unpredictable medium which we have naively been calling empty space.

APPENDIX A

Coordinates and units

Throughout this dissertation we use the so called “natural” system of units, in which

$$\hbar = c = k_B = 1 \quad (\text{A.1})$$

Given a unit of energy, the conversion ($\hbar c$) will make it an inverse of the distance. Thus,

$$\hbar c = 197 \text{MeVfm}, \quad 1 \text{GeV} = 5.4 \text{fm}^{-1} \quad (\text{A.2})$$

When dealing with a collision at ultra-relativistic energies, it is convenient to split the momentum into components parallel and perpendicular to the collision and express the parallel part as an energy-momentum rapidity

$$y = \frac{1}{2} \ln \left(\frac{E + p_L}{E - p_L} \right) \quad (\text{A.3})$$

it is easy to show that y transforms linearly under a Lorentz boost

$$y \rightarrow y + y_0 \quad (\text{A.4})$$

it is also easy to show that

$$E = m_T \cosh(y) \quad p_L = m_T \sinh(y) \quad (\text{A.5})$$

where we defined the “transverse mass” $m_T = \sqrt{p_T^2 + m^2}$. Hence, a particle’s 4-momentum can be parametrized as

$$p^\mu = \begin{pmatrix} m_T \cosh(y) \\ p_T \cos(\phi) \\ p_T \sin(\phi) \\ m_T \sinh(y) \end{pmatrix} \quad (\text{A.6})$$

Experimentally measuring rapidity can be problematic, as it requires particle identification. Hence, many experiments measure pseudo-rapidity

$$\eta = \frac{1}{2} \ln \left(\frac{p + p_L}{p - p_L} \right) = -\ln \left[\tan \left(\frac{\theta}{2} \right) \right] \quad (\text{A.7})$$

where $\theta = \tan(p_T/p_L)$. in the ultra-relativistic limit $m \ll p \rightarrow E$

$$y \approx \eta - \frac{m^2}{2p} \frac{2p_L}{p^2 - p_L^2} + \dots \quad (\text{A.8})$$

so the approximation works much better in the central rapidity ($p_L \ll p$) region.

APPENDIX B

Fitting

Suppose we have a theory which relates variables y and x through a parameter α

$$y = f(x, \alpha) \quad (\text{B.1})$$

and a set of uncorrelated experimental data points (y_i, x_i) with an experimental error σ_i . The probability that the “true” value y gives the experimental result y_i is given by some probability density function $P(y, y_i, \sigma_i)$. Hence, the probability that N data points y were measured as y_i is given by the likelihood function

$$P_{tot} = \prod_{i=1}^N P(f(x_i, \alpha), y_i, \sigma_i) \quad (\text{B.2})$$

by maximizing P_{tot} , or (for mathematical simplicity)

$$\log(P_{tot}) = \sum_{i=1}^N \log(P(f(x_i, \alpha), y_i, \sigma_i)) \quad (\text{B.3})$$

we can find an estimate of the parameter α .

In particular, if the error function is a Gaussian

$$P(x, x_i, \sigma_i) = \frac{1}{\sqrt{2\pi\sigma_i^2}} e^{-\frac{(x-x_i)^2}{2\sigma_i^2}} \quad (\text{B.4})$$

the Maximum likelihood corresponds to the minimum χ^2 where

$$\chi^2 = \sum_{i=1}^N \left(\frac{f(x_i, \alpha) - y_i}{\sigma_i} \right)^2 \quad (\text{B.5})$$

By Taylor-expanding χ^2 in the region of the minimum

$$\chi^2 \approx \chi_{min}^2 + \frac{d^2\chi^2}{d^2\alpha}(\alpha - \alpha_{min})^2 = \quad (B.6)$$

and remembering that $P_{tot} \sim e^{\chi^2}$ the error on the parameter α can be found by

$$\Delta\alpha = \frac{2}{\sqrt{\frac{d^2\chi^2}{d^2\alpha}}} \quad (B.7)$$

This procedure can be generalized from one parameter α to a set of parameters α_i (In this thesis, minimizations with 13 parameters are performed). The error then becomes the determinant of a matrix of correlation coefficients

$$\sigma_{\alpha_{i,j}} = \frac{2}{\sqrt{\left[\frac{\partial^2\chi^2}{\partial\alpha_i\partial\alpha_j}\right]^{-1}}} \quad (B.8)$$

However, in this case the structure of the minimum in parameter space becomes non-trivial, with contours, plateaus, saddle points etc. making finding of the “true minimum” potentially very hard. In this thesis, we rely on the MINUIT numerical minimization package (James and Roos 1975) to minimize χ^2 , but we test the dependence on the parameters by explicitly calculating χ^2 profiles (χ^2 as a function of one parameter) and contours (χ^2 as a function of two parameters).

The χ^2 fit is also a test of how well does the theory $y = f(x, \alpha)$ describe the experimental data. After α is found, the minimized χ^2 can be used to obtain the “confidence level” of the fit, ie the probability, given $f(x, y, \alpha_{min})$, that the total χ^2 obtained in an experiment is of that value or higher.

$$CL(\chi^2) = \int_{\chi^2}^{\infty} \prod_i^n P(x, x_i, \sigma_i) \approx \int_{\chi^2}^{\infty} e^{-z^2/2} dz \quad (B.9)$$

the quantitative dependence of $CL(\chi^2)$ as a function of χ^2 and the degrees of freedom is shown in Fig. B (Hagiwara et al. 2002). As can be seen, the confidence

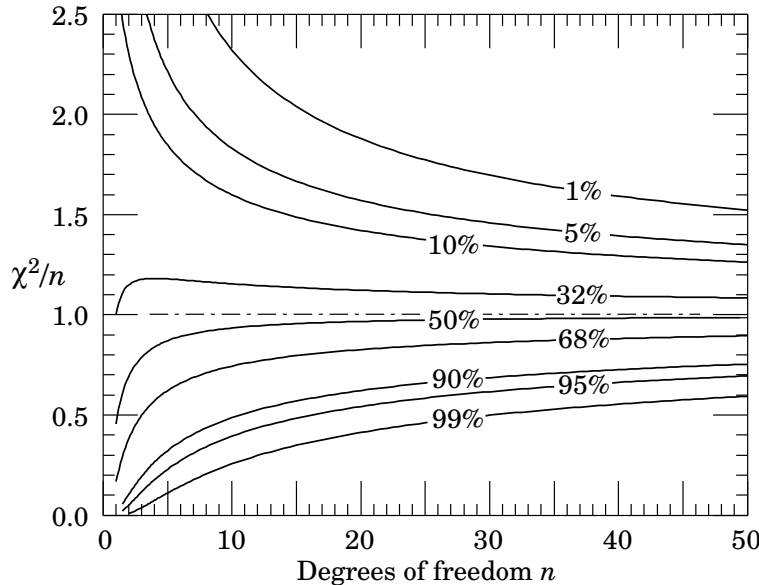


Figure B.1: Confidence levels as a function of degrees of freedom.

levels tend to an asymptotic limit as the degrees of freedom increase, corresponding to an expectation of $\chi^2 \simeq \text{DoF}$. This limit is valid in the fits to particle spectra performed in chapters 3 and 4. However, if the degrees of freedom in the fit are limited (as in the fits to particle yields discussed in chapter 2), the confidence level depends strongly on the number of degrees of freedom, and a χ^2/DoF considerably less than 1 is required for the fit to be statistically significant.

It should be remembered that the confidence level plot is only significant when all errors are Gaussian. This is generally not true if large systematic errors are present. In this case, when these errors can be estimated precisely they should be taken into account by summing systematic and statistical errors

$$\chi^2 = \sum_{i=1}^N \left(\frac{f(x_i, \alpha) - y_i}{\sigma_i^{statistical} + \sigma_i^{systematic}} \right)^2. \quad (\text{B.10})$$

If, however, this can not be done statistical stops being a quantitative measure of the fit's validity. In chapter 3 we encounter precisely this problem with K_s .

APPENDIX C

Relativistic phase space

The relativistic phase space for a physical system is the volume in 4-momentum space corresponding to the system's invariant mass (which we call m . For many-particle systems, it corresponds to \sqrt{s})

$$\Omega = \int d^4p \delta(p_\mu p^\mu - m^2) = \int d^3p \int_0^\infty dE \delta\left(\sqrt{E^2 - p^2 - m^2}\right) \quad (\text{C.1})$$

This integral can be simplified keeping in mind that

$$\delta(f(x)) = \frac{1}{\left[\frac{df}{dx}\right]_{x=x_0}} \delta(x - x_0)$$

differentiating the delta-function in Eq.(C.2) by E it can be seen, immediately, that

$$\Omega = \int d^3p \int_0^\infty \frac{dE}{2E} \delta\left(E - \sqrt{p^2 - m^2}\right) = \int \frac{d^3p}{2E} \delta\left(E - \sqrt{p^2 - m^2}\right) \quad (\text{C.2})$$

It can be seen that this expression is relativistically invariant by Lorentz-transforming a volume of phase space explicitly (without loss of generality, in the z direction)

$$dp'_x dp'_y dp'_z = dp_x dp_y \gamma(dp_z - vdE) = dp_x dp_y dp_z \gamma \left(1 - v \frac{dE}{dp_z}\right)$$

Since

$$\frac{dE}{dp_z} = \frac{d}{dp_z} \sqrt{m^2 + p_z^2} = \frac{p_z}{E}$$

we get

$$dp_x dp_y dp_z \left(1 - v \frac{dE}{dp_z}\right) = dp_x dp_y dp_z \gamma \left(1 - v \frac{p_z}{E}\right) = dp_x dp_y dp_z \frac{E'}{E}$$

Hence, we have proven that

$$\frac{dp'_x dp'_y dp'_z}{E'} = \frac{dp_x dp_y dp_z}{E}$$

as required.

We have therefore derived the relativistic phase space for a particle of momentum p , energy E and mass m . For a system of N particles with momentum p and energy E , such as those discussed in Chapter 2, it is easy to generalize our result to

$$\frac{d^3 p}{E} \rightarrow \int \prod_{i=1}^N \frac{d^3 p_i}{E_i} \delta \left(\sum_{i=1}^N p_i - p \right) \delta \left(\sum_{i=1}^N E_i - E \right)$$

APPENDIX D

Publications

Several parts of this thesis have been published in peer-Reviewed Journals. We shall give a listing of publications contained in this thesis, together with the chapter which follows the publication most closely.

- (Torrieri and Rafelski 2003a; Torrieri and Rafelski 2001a; Letessier et al. 2001)

Chapter 3

Paper (Torrieri and Rafelski 2001a) was chosen for the IoP select article collection. See <http://www.iop.org>Select/>

- (Torrieri and Rafelski 2002; Rafelski et al. 2001; Torrieri and Rafelski 2001b;

Letessier et al. 2003) Chapter 4

- (Torrieri and Rafelski 2004) **Chapter 5**

- Part of chapter 2 (the inclusion of width in particle yields) (Torrieri et al. 2004) has recently been submitted to Communications in Physical Computing.

- Chapter 6 (Torrieri and Rafelski 2004) is part of a continued research effort which will eventually be published.

APPENDIX E

Further acknowledgments

This section can only start with Dr Johann Rafelski, my advisor. Through four hard years, he did his best to make me into a research scientist. I am humbly grateful to him, and sincerely hope to make the best of his teachings.

This thesis, in it's current form, would also have been impossible without the generous help and support given by my committee. Therefore, I would like to thank Drs Keith Dienes, Mike Shupe, Robert Thews and Ubirajara van Kolck for the time taken to read the thesis, as well as their assistance and advice.

Part of the research summarized in this thesis has been performed during my stay in Krakow in the summer of 2003. I therefore thank Dr Wojciech Broniowski and Wojciech Florkowski of the Niewodniczanski Nuclear Physics Institute for their hospitality and collaboration.

The interaction with experimentalists throughout my work is also greatly appreciated. In particular, I thank Sevil Salur for taking an interest in my work, keeping me continuously on my toes with her questions, and, in general, for her friendship. I also greatly benefited by the interaction I had with Christina Markert and Patricia Fachini.

This department has been the most socially cohesive and friendly physics

department I have ever come across. I would like to thank everyone who contributes in maintaining this, and urge future students to keep it up. Of course, the physicists and honorary physicists of the LSS crowd deserve a mention here. Mike, Mikey, Anne, Tommy, Gabe, Torsten, James, Jessica, Hermann, David, Delphi, John and many others have made the ride here infinitely more bearable.

Despite what many physicists tell you, life does not end at the exit of the physics department. I wish to credit the wonderful people who assisted me in life outside of physics for the last four and a half years. I sincerely hope I learned something from them. Thank you Celeste, Carrie, Sarmad, Baha, Nesreen, Paul, Rachel, Hanna, Will, Czarina, Jessica, Allen, Pietro, Susan and many many others.

I should also acknowledge that I am lucky enough to be able to devote 28 years of my life to full-time education, and make a living by satisfying my intellectual curiosity in subjects unrelated to everyday survival. This is a privilege which only a small subset of humanity, in space and time, can enjoy. I hope some of my activities, at the University of Arizona and elsewhere, have contributed to increase that subset.

Finally, the most important acknowledgment of all: This dissertation brought me to the other side of the world from my wonderful parents, who raised me, taught me curiosity and determination, and had to endure the painful separation so I could achieve my dreams.

Thank you all.

I could not have done it without you.

REFERENCES

Abreu, M. C. et al. (2000). Evidence for deconfinement of quarks and gluons from the j/ψ suppression pattern measured in pb-pb collisions at the cern-sps. *Phys. Lett.* **B477**, 28–36.

Adams, J. et al. (2003a). Evidence from $d + au$ measurements for final-state suppression of high $p(t)$ hadrons in $au + au$ collisions at rhic. *Phys. Rev. Lett.* **91**, 072304.

Adams, J. et al. (2003b). Multi-strange baryon production in au au collisions at $s(nn)^{**}(1/2) = 130$ -gev.

Adams, J. et al. (2004). Azimuthal anisotropy at rhic: The first and fourth harmonics. *Phys. Rev. Lett.* **92**, 062301.

Adler, C. et al. (2002a). Elliptic flow from two- and four-particle correlations in $au + au$ collisions at $s(nn)^{**}(1/2) = 130$ -gev. *Phys. Rev.* **C66**, 034904.

Adler, C. et al. (2002b). $K^*(892)0$ production in relativistic heavy ion collisions at $s(nn)^{**}(1/2) = 130$ -gev. *Phys. Rev.* **C66**, 061901.

Adler, S. S. et al. (2003). Elliptic flow of identified hadrons in $au + au$ collisions at $s(nn)^{**}(1/2) = 200$ -gev. *Phys. Rev. Lett.* **91**, 182301.

Afanasev, S. V. et al. (2002). New results from na49. *Nucl. Phys.* **A698**, 104–111.

Afanasiev, S. V. et al. (2003). Recent results on spectra and yields from na49. *Nucl. Phys.* **A715**, 161–170.

Aggarwal, M. M. et al. (1999). Freeze-out parameters in central 158gev pb-208 + pb-208 collisions. *Phys. Rev. Lett.* **83**, 926–930.

Akkelin, S. V., P. Braun-Munzinger, and Y. M. Sinyukov (2002). Reconstruction of hadronization stage in pb + pb collisions at 158gev/c. *Nucl. Phys.* **A710**, 439–465.

Albrecht, R. et al. (1995). Production of eta mesons in 200-a/gev $s + s$ and $s + au$ reactions. *Phys. Lett.* **B361**, 14–20.

Alt, C. et al. (2004). Observation of an exotic $s = -2$, $q = -2$ baryon resonance in proton proton collisions at the cern sps. *Phys. Rev. Lett.* **92**, 042003.

Ambrosini, G. et al. (1999). Impact parameter dependence of π^+ , κ^+ , p , anti- p , d and anti- d production in pb + pb collisions at 158gev. *Nucl. Phys.* **A661**, 370–373.

Anderlik, C. et al. (1999). Freeze out in hydrodynamical models. *Phys. Rev. C* **59**, 3309–3316.

Andersen, E. et al. (1999). Strangeness enhancement at mid-rapidity in pb-pb collisions at 158 gev/c. *Phys. Lett. B* **449**, 401–406.

Antinori, F. et al. (1999). Strangeness enhancement at midrapidity in pb-pb collisions at 158 gev/c: A comparison with venus and rqmd models. *Eur. Phys. J. C* **11**, 79–88.

Appelshauser, H. et al. (1998). Directed and elliptic flow in 158-gev/nucleon pb + pb collisions. *Phys. Rev. Lett.* **80**, 4136–4140.

Appelshauser, H. et al. (1999). Baryon stopping and charged particle distributions in central pb + pb collisions at 158-gev per nucleon. *Phys. Rev. Lett.* **82**, 2471–2475.

Arbex, N., F. Grassi, Y. Hama, and O. Socolowski (2002). Do we need to incorporate separate chemical and thermal freeze-outs in hydrodynamics? *J. Phys. G* **28**, 2029–2033.

Back, B. B. et al. (2004). Particle production at very low transverse momenta in au + au collisions at $s(nn)^{**}(1/2) = 200$ -gev.

Bali, G. S. (2001). Qcd forces and heavy quark bound states. *Phys. Rept.* **343**, 1–136.

Baran, A., W. Broniowski, and W. Florkowski (2003). Private communication. *Private communication*.

Baran, A., W. Broniowski, and W. Florkowski (2004). Description of the particle ratios and transverse-momentum spectra for various centralities at rhic in a single- freeze-out model. *Acta Phys. Polon. B* **35**, 779–798.

Barmin, V. V. et al. (2003). Observation of a baryon resonance with positive strangeness in k+ collisions with xe nuclei. *Phys. Atom. Nucl.* **66**, 1715–1718.

Bass, S. A. et al. (1998). Microscopic models for ultrarelativistic heavy ion collisions. *Prog. Part. Nucl. Phys.* **41**, 225–370.

Bearden, I. G. (2004). Charged meson rapidity distributions in central au + au collisions at $s(nn)^{**}(1/2) = 200$ -gev.

Becattini, F., M. Gazdzicki, A. Keranen, J. Manninen, and R. Stock (2003). Study of chemical equilibrium in nucleus nucleus collisions at ags and sps energies.

Bernard, C. W. et al. (2000). The static quark potential in three flavor qcd. *Phys. Rev. D* **62**, 034503.

Biro, T. S. and B. Muller (2004). Almost exponential transverse spectra from power law spectra. *Phys. Lett. B* **578**, 78–84.

Bjorken, J. D. (1983). Highly relativistic nucleus-nucleus collisions: The central rapidity region. *Phys. Rev.* **D27**, 140–151.

Bleicher, M. and H. Stocker (2004). Dynamics and freeze-out of hadron resonances at rhic. *J. Phys.* **G30**, S111–S118.

Bolz, J., U. Ornik, M. Plumer, B. R. Schlei, and R. M. Weiner (1993). Resonance decays and partial coherence in bose-einstein correlations. *Phys. Rev.* **D47**, 3860–3870.

Brambilla, N., A. Pineda, J. Soto, and A. Vairo (2000). Potential nrqcd: An effective theory for heavy quarkonium. *Nucl. Phys.* **B566**, 275.

Bratkovskaya, E. L., S. Soff, H. Stocker, M. van Leeuwen, and W. Cassing (2004). Evidence for nonhadronic degrees of freedom in the transverse mass spectra of kaons from relativistic nucleus nucleus collisions. *Phys. Rev. Lett.* **92**, 032302.

Braun-Munzinger, P., I. Heppe, and J. Stachel (1999). Chemical equilibration in pb + pb collisions at the sps. *Phys. Lett.* **B465**, 15–20.

Braun-Munzinger, P., D. Magestro, K. Redlich, and J. Stachel (2001). Hadron production in au au collisions at rhic. *Phys. Lett.* **B518**, 41–46.

Bruno, G. E. et al. (2003). Transverse mass distributions of strange particles produced in pb-pb collisions at 158gev/c.

Bugaev, K. A. (1996). Shock-like freeze-out in relativistic hydrodynamics. *Nucl. Phys.* **A606**, 559–567.

Bugaev, K. A. (2004). Boundary conditions of the hydro-cascade model and relativistic kinetic equations for finite domains.

Burward-Hoy, J. M. (2003). Source parameters from identified hadron spectra and hbt radii for au au collisions at $s(nn)^{**}(1/2) = 200$ -gev in phenix. *Nucl. Phys.* **A715**, 498–501.

Byckling, E. and K. Kajantie (1969). Reductions of the phase-space integral in terms of simpler processes. *Phys. Rev.* **187**, 2008–2016.

Capella, A., E. G. Ferreiro, A. B. Kaidalov, and D. Sousa (2004). Anomalous suppression of pi0 production at large transverse momentum in au + au and d + au collisions at $s(nn)^{**}(1/2) = 200$ -gev.

Chaudhuri, A. K. (2002). Nuclear absorption and j/psi suppression in pb + pb collisions. *Phys. Rev.* **C66**, 021902.

Chodos, A., R. L. Jaffe, K. Johnson, and C. B. Thorn (1974). Baryon structure in the bag theory. *Phys. Rev.* **D10**, 2599.

Cooper, F. and G. Frye (1974). Comment on the single particle distribution in the hydrodynamic and statistical thermodynamic models of multiparticle production. *Phys. Rev.* **D10**, 186.

Creutz, M. (1978). Feynman rules for lattice gauge theory. *Rev. Mod. Phys.* **50**, 561.

Csernai, L. P., M. I. Gorenstein, L. L. Jenkovszky, I. Lovas, and V. K. Magas (2003). Can supercooling explain the hbt puzzle? *Phys. Lett.* **B551**, 121–126.

Csorgo, T. and L. P. Csernai (1994). Quark - gluon plasma freezeout from a supercooled state? *Phys. Lett.* **B333**, 494–499.

Dashen, R. F. and R. Rajaraman (1974). Narrow resonances in statistical mechanics. *Phys. Rev.* **D10**, 694.

Diakonov, D., V. Petrov, and M. V. Polyakov (1997). Exotic anti-decuplet of baryons: Prediction from chiral solitons. *Z. Phys.* **A359**, 305–314.

Dong, X., S. Esumi, P. Sorensen, N. Xu, and Z. Xu (2004). Resonance decay effects on anisotropy parameters.

Ehehalt, W. and W. Cassing (1996). Relativistic transport approach for nucleus nucleus collisions from sis to sps energies. *Nucl. Phys.* **A602**, 449–486.

Ejiri, S. et al. (2003). Study of qcd thermodynamics at finite density by taylor expansion.

Fachini, P. (2002). Resonance studies at star. *Heavy Ion Phys.* **15**, 195–204.

Fachini, P. (2004). Resonance production in au + au and p + p collisions at $s(nn)^{**}(1/2) = 200$ -gev. *Acta Phys. Polon.* **B35**, 183–186.

Fermi, E. (1950). High-energy nuclear events. *Prog. Theor. Phys.* **5**, 570–583.

Fries, R. J., B. Muller, C. Nonaka, and S. A. Bass (2003). Hadron production in heavy ion collisions: Fragmentation and recombination from a dense parton phase. *Phys. Rev.* **C68**, 044902.

Friese, V. (2002). Production of strange resonances in c + c and pb + pb collisions at 158gev. *Nucl. Phys.* **A698**, 487–490.

Ftačník, J., K. Kajantie, N. Pisutova, and J. Pisut (1987). On the transverse energy distributions in the central rapidity region of o-16 pb collisions at 200-gev per nucleon. *Phys. Lett.* **B188**, 279.

Gale, C., T. C. Awes, R. J. Fries, and D. K. Srivastava (2004). The electromagnetic signature of jets.

Gastineau, F. and J. Aichelin (2000). The emitting source: Can it be determined by the hbt correlation function in ultrarelativistic heavy ion collisions?

Gazdzicki, M. (2004). Energy scan program at the cern sps and an observation of the deconfinement phase transition in nucleus nucleus collisions. *J. Phys.* **G30**, S161–S168.

Geiger, K. (1993). Particle production in high-energy nuclear collisions: A parton

cascade cluster hadronization model. *Phys. Rev.* **D47**, 133–159.

Gounaris, G. J. and J. J. Sakurai (1968). Finite width corrections to the vector meson dominance prediction for $\rho \rightarrow e^+ e^-$. *Phys. Rev. Lett.* **21**, 244.

Gradshteyn, I. and I. Ryzhik (1989). Tables of integrals, series and products. Academic press.

Gribov, V. N. (1999). The theory of quark confinement. *Eur. Phys. J.* **C10**, 91–105.

Gyulassy, M. (2004). The qgp discovered at rhic. *NATO Advanced Study Institute: Structure and Dynamics of Elementary Matter, Kemer, Turkey, 22 Sep - 2 Oct 2003..*

Gyulassy, M., I. Vitev, and X. N. Wang (2001). High $p(t)$ azimuthal asymmetry in noncentral $a + a$ at rhic. *Phys. Rev. Lett.* **86**, 2537–2540.

Gyulassy, M., I. Vitev, X.-N. Wang, and B.-W. Zhang (2003). Jet quenching and radiative energy loss in dense nuclear matter. *Published in Quark Gluon Plasma 3, editors: R.C. Hwa and X.N. Wang, World Scientific, Singapore..*

Hagedorn, R. (1965). Statistical thermodynamics of strong interactions at high-energies. *Nuovo Cim. Suppl.* **3**, 147–186.

Hagedorn, R. (1984). Multiplicities, $p(t)$ distributions and the expected hadron \rightarrow quark - gluon phase transition. *Riv. Nuovo Cim.* **6N10**, 1–50.

Hagedorn, R., I. Montvay, and J. Rafelski. Thermodynamics of nuclear matter from the statistical bootstrap model. Presented at Workshop on Theoretical Physics: Hadronic Matter at Extreme Energy Density, Erice, Italy, Oct 13-21, 1978.

Hagiwara, K., K. Hikasa, K. Nakamura, M. Tanabashi, M. Aguilar-Benitez, C. Amsler, R. Barnett, P. Burchat, C. Carone, C. Caso, G. Conforto, O. Dahl, M. Doser, S. Eidelman, J. Feng, L. Gibbons, M. Goodman, C. Grab, D. Groom, A. Gurtu, K. Hayes, J. Hernández-Rey, K. Honscheid, C. Kolda, M. Mangano, D. Manley, A. Manohar, J. March-Russell, A. Massoni, R. Miquel, K. Mönig, H. Murayama, S. Navas, K. Olive, L. Pape, C. Patrignani, A. Piepke, M. Roos, J. Terning, N. Törnqvist, T. Trippe, P. Vogel, C. Wohl, R. Workman, W.-M. Yao, B. Armstrong, P. Gee, K. Lugovsky, S. Lugovsky, V. Lugovsky, M. Artuso, D. Asner, K. Babu, E. Barberio, M. Battaglia, H. Bichsel, O. Biebel, P. Bloch, R. Cahn, A. Cattai, R. Chivukula, R. Cousins, G. Cowan, T. Damour, K. Desler, R. Donahue, D. Edwards, V. Elvira, J. Erler, V. Ezhela, A. Fassò, W. Fettscher, B. Fields, B. Foster, D. Froidevaux, M. Fukugita, T. Gaisser, L. Garren, H.-J. Gerber, F. Gilman, H. Haber, C. Hagmann, J. Hewett, I. Hinchliffe, C. Hogan, G. Höhler, P. Igo-Kemenes, J. Jackson, K. Johnson, D. Karlen, B. Kayser, S. Klein, K. Kleinknecht, I. Knowles, P. Kreitz, Y. Kuyanov, R. Landua, P. Langacker, L. Littenberg, A. Martin, T. Nakada, M. Narain, P. Nason, J. Peacock, H. Quinn, S. Raby, G. Raffelt, E. Razuvaev, B. Renk, G. Rolandi, M. Ronan, L. Rosenberg, C. Sachrajda, A. Sanda, S. Sarkar, M. Schmitt, O. Schneider, D. Scott, W. Seligman, M. Shaevitz, T. Sjöstrand, G. Smoot,

S. Spanier, H. Spieler, N. Spooner, M. Srednicki, A. Stahl, T. Staney, M. Suzuki, N. Tkachenko, G. Valencia, K. van Bibber, M. Vincter, D. Ward, B. Webber, M. Whalley, L. Wolfenstein, J. Womersley, C. Woody, and O. Zenin (2002). Review of Particle Physics. *Physical Review D* **66**, 010001+.

Heinz, U. W. and M. Jacob (2000). Evidence for a new state of matter: An assessment of the results from the cern lead beam programme, and <http://cern.web.cern.ch/cern/announcements/2000/newstatematter/>.

Heinz, U. W. and P. F. Kolb (2002). Two rhic puzzles: Early thermalization and the hbt problem.

Hirano, T. and K. Tsuda (2003). Collective flow and hbt radii from a full 3d hydrodynamic model with early chemical freeze out. *Nucl. Phys.* **A715**, 821–824.

Hohne, C. et al. (2003). System size dependence of strangeness production at 158-a- gev. *Nucl. Phys.* **A715**, 474–477.

Iancu, E., A. Leonidov, and L. McLerran (2002). The colour glass condensate: An introduction. *Cargese 2001, QCD perspectives on hot and dense matter*, 73–145.

James, F. and M. Roos (1975). 'minuit' a system for function minimization and analysis of the parameter errors and correlations. *Comput. Phys. Commun.* **10**, 343–367.

Johnson, K. (1975). The m.i.t. bag model. *Acta Phys. Polon.* **B6**, 865.

Kajantie, K., J. Kapusta, L. D. McLerran, and A. Mekjian (1986). Dilepton emission and the qcd phase transition in ultrarelativistic nuclear collisions. *Phys. Rev.* **D34**, 2746.

Kapusta, J., P. Lichard, and D. Seibert (1991). High-energy photons from quark - gluon plasma versus hot hadronic gas. *Phys. Rev.* **D44**, 2774–2788.

Kapusta, J. I. (1979). Quantum chromodynamics at high temperature. *Nucl. Phys.* **B148**, 461–498.

Karsch, F. (1998). Deconfinement and chiral symmetry restoration.

Karsch, F. and E. Laermann (2003). Thermodynamics and in-medium hadron properties from lattice qcd.

Karsch, F., K. Redlich, and A. Tawfik (2003). Hadron resonance mass spectrum and lattice qcd thermodynamics. *Eur. Phys. J.* **C29**, 549–556.

Keranen, A., J. Manninen, L. P. Csernai, and V. Magas (2003). Statistical hadronization of supercooled quark-gluon plasma. *Phys. Rev.* **C67**, 034905.

Kleiss, R. and W. J. Stirling (1992). Massive multiplicities and monte carlo. *Nucl. Phys.* **B385**, 413–432.

Koch, P., B. Muller, and J. Rafelski (1986). Strangeness in relativistic heavy ion collisions. *Phys. Rept.* **142**, 167–262.

Kolb, P. F. (2003). v4 - a small, but sensitive observable for heavy ion collisions. *Phys. Rev.* **C68**, 031902.

Kolb, P. F. and U. Heinz (2003). Hydrodynamic description of ultrarelativistic heavy-ion collisions.

Landau, L. (1953). A hydrodynamic theory of multiple formation of particles. *Izv. Akad. Nauk SSSR (Ser. Fiz.)* **17**, 51.

Lebedev, A. et al. (1994). Comparison of pi0 and eta spectrum from s + au collisions at 200-gev/c. *Nucl. Phys.* **A566**, 355c–358c.

Lenkeit, B. et al. (1999). Recent results from pb au collisions at 158-gev/c per nucleon obtained with the ceres spectrometer. *Nucl. Phys.* **A661**, 23–32.

Letessier, J. and J. Rafelski (2000). Observing quark-gluon plasma with strange hadrons. *Int. J. Mod. Phys.* **E9**, 107–147.

Letessier, J. and J. Rafelski (2002). Hadrons and quark - gluon plasma. *Cambridge Monogr. Part. Phys. Nucl. Phys. Cosmol.* **18**, 1–397.

Letessier, J. and J. Rafelski (2003). Qcd equations of state and the qgp liquid model. *Phys. Rev.* **C67**, 031902.

Letessier, J., G. Torrieri, S. Hamieh, and J. Rafelski (2001). Qgp fireball explosion. *J. Phys.* **G27**, 427–438.

Letessier, J., G. Torrieri, S. Steinke, and J. Rafelski (2003). Strange pentaquark hadrons in statistical hadronization. *Phys. Rev.* **C68**, 061901.

Letessier, J., A. Tounsi, and J. Rafelski (1992). Hot hadronic matter and strange anti-baryons. *Phys. Lett.* **B292**, 417–423.

Letessier, J., A. Tounsi, and J. Rafelski (2000). Low-m(t) pi+ pi- asymmetry and pion enhancement from hadronization of qgp. *Phys. Lett.* **B475**, 213–219.

Lifshitz, E. and L. Pitaevskii (1981). Physical kinetics. Pergamon Press.

Markert, C., G. Torrieri, and J. Rafelski (2002a). Strange hadron resonances: Freeze-out probes in heavy-ion collisions.

Markert, C., G. Torrieri, and J. Rafelski (2002b). Strange hadron resonances: Freeze-out probes in heavy-ion collisions.

Matsubara, T. (1955). A new approach to quantum statistical mechanics. *Prog. Theor. Phys.* **14**, 351–378.

Matsui, T. and H. Satz (1986). J / psi suppression by quark - gluon plasma formation. *Phys. Lett.* **B178**, 416.

McLerran, L. D. and B. Svetitsky (1981). Quark liberation at high temperature: A monte carlo study of su(2) gauge theory. *Phys. Rev.* **D24**, 450.

Molnar, D. and S. A. Voloshin (2003). Elliptic flow at large transverse momenta from quark coalescence. *Phys. Rev. Lett.* **91**, 092301.

Nakano, T. et al. (2003). Observation of $s = +1$ baryon resonance in photo-production from neutron. *Phys. Rev. Lett.* **91**, 012002.

Nambu, Y. and G. Jona-Lasinio (1961). Dynamical model of elementary particles based on an analogy with superconductivity. i. *Phys. Rev.* **122**, 345–358.

Nebauer, R. and J. Aichelin (2002). Thermodynamics of the three-flavor nambu-jona-lasinio model: Chiral symmetry breaking and color superconductivity. *Phys. Rev.* **C65**, 045204.

Ollitrault, J.-Y. (1992). Anisotropy as a signature of transverse collective flow. *Phys. Rev.* **D46**, 229–245.

Ollitrault, J.-Y. (1993). Determination of the reaction plane in ultrarelativistic nuclear collisions. *Phys. Rev.* **D48**, 1132–1139.

Olszewski, A. et al. (2002). Overview of results from phobos experiment at rhic. *J. Phys.* **G28**, 1801–1807.

Peitzmann, T. (2003). Influence of hydrodynamics on the interpretation of the high $p(t)$ hadron suppression at rhic. *Nucl. Phys.* **A727**, 179–192.

Peskin, M. E. and D. V. Schroeder (1995). An introduction to quantum field theory. Reading, USA: Addison-Wesley (1995) 842 p.

Pinkenburg, C. et al. (1999). Elliptic flow: Transition from out-of-plane to in-plane emission in au + au collisions. *Phys. Rev. Lett.* **83**, 1295–1298.

Polyakov, A. M. (1978). Thermal properties of gauge fields and quark liberation. *Phys. Lett.* **B72**, 477–480.

Pomeranchuk, I. (1951). On multiparticle production in single interaction process. *Proc. USSR Academy of Sciences* **43**, 889.

Poskanzer, A. M. and S. A. Voloshin (1998). Methods for analyzing anisotropic flow in relativistic nuclear collisions. *Phys. Rev.* **C58**, 1671–1678.

Pratt, S. and W. Bauer (2003). Thermal production of the rho meson in the $\pi^+ \pi^-$ channel. *Phys. Rev.* **C68**, 064905.

Rafelski, J., L. P. Fulcher, and A. Klein (1978). Fermions and bosons interacting with arbitrarily strong external fields. *Phys. Rept.* **38**, 227–361.

Rafelski, J. and J. Letessier (2000). Sudden hadronization in relativistic nuclear collisions. *Phys. Rev. Lett.* **85**, 4695–4698.

Rafelski, J. and J. Letessier (2002). Importance of reaction volume in hadronic

collisions: Canonical enhancement. *J. Phys.* **G28**, 1819–1832.

Rafelski, J. and J. Letessier (2003a). Strangeness and statistical hadronization: How to study quark-gluon plasma. *Acta Phys. Polon.* **B34**, 5791–5824.

Rafelski, J. and J. Letessier (2003b). Strangeness and statistical hadronization: How to study quark-gluon plasma. *Acta Phys. Polon.* **B34**, 5791–5824.

Rafelski, J. and J. Letessier (2003c). Strangeness excitation function in heavy ion collisions.

Rafelski, J. and J. Letessier (2003d). Testing limits of statistical hadronization. *Nucl. Phys.* **A715**, 98–107.

Rafelski, J., J. Letessier, and G. Torrieri (2001). Strange hadrons and their resonances: A diagnostic tool of qgp freeze-out dynamics. *Phys. Rev.* **C64**, 054907.

Rafelski, J., J. Letessier, and A. Tounsi (1996). Strange particles from dense hadronic matter. *Acta Phys. Polon.* **B27**, 1037–1140.

Rafelski, J. and B. Muller (1982). Strangeness production in the quark - gluon plasma. *Phys. Rev. Lett.* **48**, 1066.

Randrup, J. (2003). Production of the exotic theta baryon in relativistic nuclear collisions. *Phys. Rev.* **C68**, 031903.

Richardson, J. L. (1979). The heavy quark potential and the upsilon, j / ψ systems. *Phys. Lett.* **B82**, 272.

Rischke, D. H. (2002). Remarks on the extraction of freeze-out parameters. *Nucl. Phys.* **A698**, 153–163.

Salur, S. (2004). Sigma(1385) resonance studies with star at $\sqrt{s_{NN}}=200$ gev.

Sandor, L. et al. (2004). Hyperon production at the cern sps: Results from the na57 experiment. *J. Phys.* **G30**, S129–S138.

Schnedermann, E. and U. W. Heinz (1993). Relativistic hydrodynamics in a global fashion. *Phys. Rev.* **C47**, 1738–1750.

Schroedter, M., R. L. Thews, and J. Rafelski (2000). B/c meson production in nuclear collisions at rhic. *Phys. Rev.* **C62**, 024905.

Sollfrank, J., P. Koch, and U. W. Heinz (1990). The influence of resonance decays on the $p(t)$ spectra from heavy ion collisions. *Phys. Lett.* **B252**, 256–264.

Sonin, A. (1991). Viscous fingers: from simple amorphous forms to anisotropic fractals. *La Rivista Del Nuovo Cimento* **14**, 10–1.

Sorge, H. (1997). Elliptical flow: A signature for early pressure in ultrarelativistic nucleus nucleus collisions. *Phys. Rev. Lett.* **78**, 2309–2312.

Staszek, P. et al. (2002). Results from brahms experiment at rhic. *Acta Phys.*

Polon. **B33**, 1387–1403.

Stepanyan, S. et al. (2003). Observation of an exotic $s = +1$ baryon in exclusive photoproduction from the deuteron. *Phys. Rev. Lett.* **91**, 252001.

't Hooft, G. (1976). Symmetry breaking through bell-jackiw anomalies. *Phys. Rev. Lett.* **37**, 8–11.

Teaney, D., J. Lauret, and E. V. Shuryak (2001). A hydrodynamic description of heavy ion collisions at the sps and rhic.

Terazawa, H. (1995). Pion pair production by two photons. *Phys. Rev.* **D51**, 954–957.

Thews, R. L., M. Schroedter, and J. Rafelski (2001). Formation of quarkonium states at rhic. *J. Phys.* **G27**, 715.

Tomasik, B., U. A. Wiedemann, and U. W. Heinz (2003). Reconstructing the freeze-out state in pb + pb collisions at 158gev/c. *Heavy Ion Phys.* **17**, 105–143.

Torrieri, G., W. Broniowski, W. Florkowski, J. Letessier, and J. Rafelski (2004). Share: Statistical hadronization with resonances. *Communications in Physics Computing To be published.*

Torrieri, G. and J. Rafelski (2001a). Search for qgp and thermal freeze-out of strange hadrons. *New J. Phys.* **3**, 12.

Torrieri, G. and J. Rafelski (2001b). Strange hadron resonances as a signature of freeze-out dynamics. *Phys. Lett.* **B509**, 239–245.

Torrieri, G. and J. Rafelski (2002). Strange hadron resonances and qgp freeze-out. *J. Phys.* **G28**, 1911–1920.

Torrieri, G. and J. Rafelski (2003a). A comparison of statistical hadronization models.

Torrieri, G. and J. Rafelski (2003b). Statistical hadronization probed by resonances. *Phys. Rev.* **C68**, 034912.

Torrieri, G. and J. Rafelski (2004). Azimuthal anisotropy of transverse momentum distribution: A probe of freeze-out dynamics. *To be published.*

Tounsi, A., A. Mischke, and K. Redlich (2003). Canonical aspects of strangeness enhancement. *Nucl. Phys.* **A715**, 565–568.

Touschek, B. (1968). Thermodynamics of nuclear matter from the statistical bootstrap model. *Nuovo Cimento* **B 58**, 295.

Various (1999). Cern program library. <http://wwwasd.web.cern.ch/wwwasd/cernlib.html>.

Voloshin, S. and Y. Zhang (1996). Flow study in relativistic nuclear collisions by

fourier expansion of azimuthal particle distributions. *Z. Phys.* **C70**, 665–672.

Wang, X.-N., M. Gyulassy, and M. Plumer (1995). The lpm effect in qcd and radiative energy loss in a quark gluon plasma. *Phys. Rev.* **D51**, 3436–3446.

Watson, M., M. Ferro-Luzzi, and R. Tripp (1963). Analysis of $y_0^*(1520)$ and determination of \sum parity. *Phys. Rev.* **131**, 2248–2280.

Wiedemann, U. A. and U. W. Heinz (1999). Particle interferometry for relativistic heavy-ion collisions. *Phys. Rept.* **319**, 145–230.

Wilson, K. G. (1974). Confinement of quarks. *Phys. Rev.* **D10**, 2445–2459.

Wong, C.-Y. (2004). Does hbt measure the freeze-out source distribution?

Zhang, H. (2004). δ , k^* and ρ resonance production and their probing of freeze-out dynamics at rhic.

Zimanyi, J. and P. Levai (2004). Quark coalescence into opposite parity baryon states.